



Sigillum Universitatis Ludovici Maximiliani

The Role of Galaxy Mergers in the Evolution of Supermassive Black Holes

**Dissertation der Fakultät für Physik
der Ludwig-Maximilians-Universität München
für den Grad des
Doctor rerum naturalium**

**vorgelegt von Silvia Bonoli
aus Bologna**

München, den 30.03.2010



Sigillum Universitatis Ludovici Maximiliani

1. Gutachter: Prof. Dr. Simon D. M. White

2. Gutachter: Prof. Dr. Hans Böhringer

Tag der mündlichen Prüfung: 28.05.2010

I AM SMART ENOUGH TO UNDERSTAND THAT I AM NOT SMART ENOUGH

personally adapted from
Richard Feynman

Contents

Contents	1
Zusammenfassung	9
Abstract	11
1 Introduction	13
1.1 The Evidence for Supermassive Black Holes	13
1.1.1 Active Galactic Nuclei	13
1.1.2 Supermassive black holes and their gravitational influence	14
1.1.3 Hypervelocity Stars	15
1.2 Properties of the black hole population	15
1.2.1 Techniques to estimate black hole masses	16
1.2.2 Black hole demographics	17
1.3 AGN and Quasars	18
1.3.1 Brief overview of AGN types	18
1.3.2 The Luminosity Function	19
1.3.3 Quasar clustering	20
1.4 The interaction between black holes and their host galaxies	24
1.4.1 Scaling relations	24
1.4.2 AGN feedback	26
1.5 The cosmological evolution of supermassive black holes	27
1.5.1 Seed Black Holes	27
1.5.2 Triggering black hole accretion	27
1.5.3 Black hole mergers	28

1.6	Outline of the thesis	29
2	Modeling the cosmological evolution of black holes and quasars	31
2.1	Introduction	31
2.2	The model	32
2.2.1	Numerical simulation	33
2.2.2	Galaxy evolution	33
2.2.3	BH mass accretion and AGN	35
2.3	Models vs. Observations	41
2.3.1	The BH scaling relations	41
2.3.2	The BH mass function	47
2.3.3	The AGN bolometric luminosity function	47
2.4	Summary of the chapter	50
3	The large-scale clustering of simulated quasars	53
3.1	Introduction	53
3.2	Models for Black Hole accretion and emission	55
3.2.1	BH seeding	55
3.2.2	Radio mode	55
3.2.3	Quasar mode	56
3.3	Clustering properties	61
3.3.1	Brief description of the correlation parameters used	61
3.3.2	AGN and dark matter clustering	63
3.3.3	AGN and halo clustering	64
3.3.4	Luminosity dependence of AGN clustering and comparison with data	67
3.4	BHs, Quasars and their dark environment	72
3.4.1	Duty cycle	77
3.5	Summary of the chapter	78
4	The <i>merger bias</i>	81
4.1	Introduction	81
4.2	Identifying merging haloes and galaxies in the Millennium Simulation	83

4.2.1	The Millennium Simulation and its galaxy population	83
4.2.2	Halo mergers	83
4.2.3	Galaxy mergers	84
4.3	Results	85
4.3.1	Clustering analysis and the excess bias F	85
4.3.2	The merger bias for DM haloes	87
4.3.3	The merger bias for galaxies	89
4.4	Implications for the clustering of quasars	92
4.5	Summary of the chapter	97
5	Semi-analytic vs. hydrodynamical simulations	99
5.1	Introduction	99
5.2	The simulations	100
5.2.1	The initial conditions	100
5.2.2	The baryonic physics in GADGET	101
5.2.3	The baryonic physics in the semi-analytic model	103
5.3	Results for the black hole population	105
5.3.1	The most massive haloes	105
5.3.2	The black hole mass function and mass density	105
5.3.3	The quasar luminosity function	110
5.3.4	The $M_{\text{BH}} - \sigma_*$ relation	111
5.4	Summary of the chapter	112
6	Summary and outlook	115
A	Black hole accretion	119
A.1	Eddington Luminosity	119
A.1.1	The radiative efficiency	120
A.1.2	The <i>e-folding</i> time	120
A.2	Black Hole accretion models	121
A.2.1	Thin disk	121
A.2.2	Thick disk	121

A.2.3 Bondi accretion	121
B Clustering statistics	123
B.1 Introduction to clustering statistics	123
B.2 Galaxy and halo clustering	124
Acknowledgements	127
Curriculum vitae	129
Publication list	131

List of Figures

List of Figures	5
1.1 Stellar orbits around Sgr A*	15
1.2 Local black hole mass function	17
1.3 AGN unification scheme	18
1.4 Logarithmic view of an AGN and its galaxy	20
1.5 AGN Luminosity Function	21
1.6 Evolution of the AGN Luminosity Density	22
1.7 AGN Correlation Length	23
1.8 Scaling relations	25
1.9 $M_{\text{BH}} - \sigma_*$ from hydrodynamical simulations	29
2.1 Time evolution of f_{Edd} , M_{BH} and L_{bol}	38
2.2 Scaling relations at $z = 0$	39
2.3 Scaling relations with three-parameters fit	44
2.4 The predicted BH fundamental plane	45
2.5 $M_{\text{BH}} - M_{\text{bulge}}$ scaling relation for different prescriptions for the BH mass accretion	46
2.6 BH mass function	47
2.7 Bolometric luminosity function for different light curve models	48
3.1 Black hole median accreted mass as a function of redshift	57
3.2 Differential black hole mass density at $z = 0$	58
3.3 Bolometric luminosity function	58
3.4 Eddington fraction distribution	59
3.5 Shape of the AGN two-point correlation function	62

3.6	The correlation function of AGN and haloes	64
3.7	Redshift and luminosity dependence of the AGN correlation function	65
3.8	The correlation function of the faintest AGN	67
3.9	Space density of simulated quasars	68
3.10	Quasar clustering: comparison with optical data	69
3.11	The clustering of L_* quasars	70
3.12	Distribution of dark matter halo masses hosting AGN	73
3.13	Redshift evolution of the AGN typical host halo mass	74
3.14	$L_{\text{Bol}} - M_{\text{Halo}}$ relation	75
3.15	$M_{\text{BH}} - M_{\text{Halo}}$ relation	76
3.16	AGN duty cycle	78
4.1	Cross-correlation function of recently-merged haloes	86
4.2	Bias and excess bias from Figure 4.1	87
4.3	Excess bias for DM haloes in separate mass bins	88
4.4	Cross-correlation function of recently-merged galaxies	90
4.5	Excess bias for galaxies in different mass bins	91
4.6	Median host DM subhalo mass for galaxies with different stellar masses	93
4.7	Bias of FOF halo merger remnants as a function of redshift	94
4.8	number of major mergers in the Millennium Simulation	95
4.9	Bias of simulated bright quasars (B-band magnitude < -24 mag)	96
5.1	Maps of the most massive haloes and their BHs from the hydro simulation	106
5.2	Maps of the most massive haloes and their BHs from the semi-analytic model	107
5.3	simulation-predicted $z = 0$ BH mass function	108
5.4	predicted evolution of the BH mass density	109
5.5	Predicted evolution of the black hole mass function	110
5.6	Predicted quasar luminosity function at various z	111
5.7	Simulated $M_{\text{BH}} - \sigma_*$ relation	112
B.1	Millennium two-point correlation function	124
B.2	Analytic halo bias	125

List of Tables

List of Tables	7
2.1 Parameters of the linear fits to the scaling relations shown in Figure 2.2	40
2.2 Parameters of the fits to the scaling relations shown in Figure 2.3	40
3.1 Values of the AGN correlation length as a function of redshift and luminosity . .	66
5.1 Simulations parameters	101

Zusammenfassung

Es ist heute weithin akzeptiert, dass supermassive schwarze Löcher bei der Entstehung und Entwicklung von Galaxien eine wichtige Rolle spielen. Supermassive schwarze Löcher haben Massen zwischen 10^6 und 10^9 Sonnenmassen, und Beobachtungen in den letzten Jahrzehnten haben Hinweise darauf geliefert, dass jede Galaxie in ihrem Zentrum ein solches Objekt beherbergt. Der gravitative Einfluss supermassiver schwarzer Löcher ist eng auf das galaktische Zentrum beschränkt. Dennoch kann es die dynamische Struktur des ganzen Sternensystems stark beeinflussen. Schwarze Löcher akkretieren Gas und Sterne, die in das galaktische Zentrum fallen. Während dieses Prozesses wird ein Teil der Gravitationsenergie des einfallenden Materials effizient in Strahlung umgewandelt, und es treten hochenergetische Phänomene wie Jets und Winde auf. Diese Strahlung kann die äussersten Randgebiete der Galaxie erreichen, und dadurch deren physikalische Eigenschaften über einen weiten Bereich von Längenskalen stark verändern. Zwischen der Masse der zentralen schwarzen Löcher und den Eigenschaften des Bulges der Galaxien wurden in den letzten Jahren starke Korrelationen entdeckt. Für eine vollständige Beschreibung der Galaxienentwicklung ist es daher essentiell zu verstehen, wie sich Galaxien und die von ihnen beherbergten schwarzen Löcher gegenseitig in ihrer Entwicklung beeinflussen.

Quasare sind mit einer Leuchtkraft von maximal den 10^{14} -fachen der Leuchtkraft der Sonne die hellsten Objekte am Himmel. Solche Helligkeiten entstehen, wenn schwarze Löcher pro Jahr bis zu 100 Sonnenmassen akkretieren. Um auf die Akkretionsscheibe des schwarzen Lochs zu fallen, muss das Gas der Galaxie in die Nähe des Schwarzschildradius gelangen und daher Drehimpuls verlieren, da der Schwarzschildradius um viele Größenordnungen kleiner ist als die typischen galaktischen Längenskalen. Welche physikalischen Prozesse solch einen hohen Verlust an Drehimpuls herbeiführen, und daher die Akkretion auf das schwarze Loch auslösen können, ist zur Zeit noch unklar. Verschmelzungen zweier Galaxien können sehr heftige Ereignisse sein: Die gesamte Struktur der Galaxie kann zerstört werden, und numerische Simulationen haben gezeigt, dass diese Prozesse Phasen intensiver Sternentstehung auslösen und große Mengen an Gas ins Zentrum der Galaxie treiben können. Zudem haben Galaxien, die aus solch einer Verschmelzung hervorgehen, typischerweise eine elliptische Morphologie. Verschmelzungen von Galaxien sind daher die wichtigsten Kandidaten für das effiziente Aktivieren von Quasaren und für die gleichzeitige Entstehung von Bulges.

Ziel dieser Arbeit ist, mit verschiedenen numerischen und statistischen Methoden die kosmologische Entwicklung supermassiver schwarzer Löcher und die Rolle von Galaxienverschmelzungen für das Auslösen effizienter Akkretion auf das schwarze Loch zu erforschen.

Im ersten Teil der Arbeit beschreiben wir das Modell für Galaxienentstehung, welches wir in einem Großteil der vorliegenden Arbeit dazu verwenden, die Entstehung und Entwicklung schwarzer Löcher und ihrer Galaxien in Halos aus dunkler Materie zu verfolgen. Dieses Modell besteht aus so genannten „merger trees“ dunkler Materie aus einer großen Simulation, welche mit

Hilfe von analytischen Vorschriften mit Galaxien bevölkert werden. Dieser Ansatz erlaubt es, die Entwicklung der Materiestrukturen im Universum in einem großen, kosmologischen Volumen und über lange Zeiträume hinweg zu simulieren, angefangen mit einem sehr jungen Universum bis hin zur heutigen Zeit. Das große Volumen ist notwendig, um eine statistische Analyse unserer Zielobjekte durchführen zu können. Wir modellieren das Wachstum der schwarzen Löcher, indem wir annehmen, dass während der Verschmelzung zweier Galaxien effiziente Akkretion auf das schwarze Loch stattfindet, welches dann als Quasar beobachtet werden kann. In Kombination mit Modellen für die Lichtkurven einzelner Akkretionsereignisse reproduzieren unsere Simulationen die wichtigsten Eigenschaften, die für die Populationen der schwarzen Löcher und Quasare beobachtet werden, als Funktion der Rotverschiebung. Mit Hilfe von Korrelationsfunktionen untersuchen wir zudem die räumliche Verteilung unserer simulierten Quasare und vergleichen diese mit den neuesten Beobachtungsdaten. In Übereinstimmung mit den Beobachtungen stellen wir fest, dass sich die räumliche Korrelationsfunktion von Quasaren mit der Rotverschiebung in der gleichen Weise entwickelt wie die der Halos. Dies deutet darauf hin, dass sich helle Quasare immer in Halos mit Massen von $10^{12} - 10^{13} h^{-1} M_{\odot}$ befinden. Die gute Übereinstimmung zwischen unseren Vorhersagen für die Korrelationsfunktion von Quasaren und den Beobachtungsergebnissen sind ein weiterer Hinweis darauf, dass die Verschmelzung von Galaxien effiziente Akkretion auf das schwarze Loch auslöst.

Dann untersuchen wir die statistische Relevanz des so genannten „merger bias“, eines Effektes, der zu einer Fehlinterpretation der beobachteten Korrelationsfunktion der Quasare führen kann. Wenn Quasare durch die Verschmelzung von Galaxien aktiviert werden und wenn kürzlich verschmolzene Objekte sich auf eine andere Weise verteilen als andere Objekte von gleicher Masse, dann eignet sich die Korrelationsfunktion nicht dazu, die Lebenszeit der Quasare oder die Eigenschaften ihrer Halos, abzuleiten. Anhand der Millenium Simulation haben wir die Signifikanz dieses Effekts in kürzlich verschmolzenen Halos untersucht, und herausgefunden, dass er vernachlässigt werden kann.

Im letzten Teil der Arbeit vergleichen wir die Entwicklung schwarzer Löcher und Quasare, wie sie durch das oben eingeführte Modell beschrieben wird, mit der in unseren kosmologischen hydrodynamischen Simulationen. Bei der Beschreibung der globalen Eigenschaften der massereichsten schwarzen Löcher und Quasare im lokalen Universum stimmen beide Modelle gut überein und reproduzieren die Beobachtungen. Ihre Vorhersagen zur Entwicklung der schwarzen Löcher und Quasare mit der Rotverschiebung sind jedoch recht unterschiedlich. Daher könnte ein Vergleich der Entwicklung individueller Objekte in beiden Modellen Hinweise auf die Prozesse liefern, die zur Akkretion auf das schwarze Loch und damit zum Aufleuchten eines Quasars führen.

Summary

In the astrophysical community, it is now widely recognized that supermassive black holes have a primary role in the formation and evolution of galaxies. Supermassive black holes have a mass between 10^6 and 10^9 times the mass of our Sun, and observations in the last couple of decades have suggested that every galaxy hosts such an object in its center. The gravitational influence of supermassive black holes is limited to the very nuclear region of the galaxy, but it can still strongly affect the dynamical structure of the whole stellar system. Like hungry monsters, black holes accrete gas and stars that fall onto the galactic center. In this process, a fraction of the gravitational potential energy of the infalling material is efficiently converted into radiation, and very powerful phenomena, like jets and winds, take place. This radiation can reach the very outer regions of the host galaxy, whose physical properties across a large range of scales can then get strongly modified. Tight relations between the mass of the central black holes and properties of the spheroidal component of the host galaxies have been discovered in the last years, and an understanding of how black holes and their hosts influence each other in their evolution has now become essential to obtain a clear picture of galaxy formation.

Quasars are the brightest objects in the sky, with luminosities that can reach 10^{14} solar luminosities. Such luminosities are explained by black holes accreting tens of solar masses per year. To fall onto the black hole accretion disk, any gas present in the galaxy has to lose enough angular momentum to get close to the Schwarzschild radius, which is many orders of magnitude smaller than typical galactic scales. Which physical processes are able to cause the loss of so much angular momentum and therefore trigger black hole accretion, is still not clear. Galaxy mergers can be very violent events: the entire galaxy structure can be disrupted, and numerical simulations have shown that these processes can trigger intense bursts of star formation and channel a lot of gas towards the nuclear regions. Moreover, merger remnants have typically spheroidal morphology. Mergers are therefore the primary candidates both for efficient quasar triggering and the simultaneous formation of spheroids.

The aim of this thesis is to use different numerical methods and statistical tools to explore the cosmological evolution of supermassive black holes and the role of mergers in triggering efficient black hole accretion.

The first part of the thesis is devoted to the description of the model for galaxy formation that we exploit in most of the presented work to follow the formation and evolution of black holes and their host galaxies within dark matter haloes: this model consists of dark matter merger trees from a large cosmological simulation populated with galaxies through analytical prescriptions. This approach allows us to simulate the life of structures from a time when the Universe was very young to the present epoch in large cosmological volumes, necessary for a statistical analysis of our target classes of objects. We modeled the growth of black holes by assuming that efficient black hole accretion and quasar events take place during galaxy mergers. Coupled with models for the light

curves associated with individual accretion events, our simulations are able to reproduce the most important observed properties of the black hole and quasar populations, as a function of redshift. We also exploit clustering statistics to study the spatial distribution of our simulated quasars and compare it with the most recent observational data. In agreement with observations, we find that quasar clustering evolves with redshift in the same way as the clustering of dark matter haloes, suggesting that bright quasars are always hosted by haloes with mass of $10^{12} - 10^{13} h^{-1} M_{\odot}$. The good agreement between our predictions for quasar clustering and the observational results gives further support to the assumption of merger-driven efficient black hole accretion.

We then explore the statistical importance of *merger bias*, an effect that could lead to a misinterpretation of the observed quasar clustering. If quasars are indeed triggered by merger events, and if recently-merged objects cluster in a different way than other objects of the same mass, then clustering cannot be used to infer either the properties of the haloes hosting quasars or the quasar lifetime. Using the Millennium Simulation, we analyzed the significance of this effect in recently merged dark matter haloes, and found that it is negligible.

In the last part of the thesis, we compare the evolution of black holes and quasars as described with the model used in the first part of the thesis, and as simulated with cosmological hydrodynamical simulations. Looking at the global properties of the black holes and quasars, we find that the two modeling procedures agree well with each other and with observations in the description of the most massive objects in the local Universe. However, the redshift evolution of the black hole and quasar populations predicted by the two models is quite different, and an analysis of the evolution of individual objects as simulated with the two numerical methods may reveal differences in the processes that lead to black hole accretion and quasar triggering.

Chapter 1

Introduction

In this chapter we introduce the most important facts related to supermassive black holes¹ and Active Galactic Nuclei. We start by discussing the observational evidences for the existence of supermassive black holes in §1.1. We then summarize the main properties of the black hole population in §1.2 and of the Active Galactic Nuclei population in §1.3. In §1.4 the link between black holes and galaxies is described, and in §1.5 the evolution of black holes is put inside a cosmological framework. Finally, the outline of the thesis is presented in §1.6.

1.1 The Evidence for Supermassive Black Holes

In this section, we give a brief overview of the observations that, in the last few decades, indicated that nearly all nearby galaxies host at their center a supermassive black hole.

1.1.1 Active Galactic Nuclei

At the beginning of the last century very bright objects with stellar-like spectral features started to be observed. Around the middle of the century, Carl Seyfert, in his work *Nuclear emission from Spiral Nebulae* reported the results of the analysis of about ten spiral galaxies with a very strong stellar-like nuclear emission (Seyfert 1943). The peculiarity of these nuclei was the presence of emission lines strongly broadened “presumably by Doppler motion, by amounts varying up to 8500 km s^{-1} ”. Seyfert also observed that “the maximum width of the Balmer emission lines seems to increase with the absolute magnitude of the nucleus and with the ratio of the light in the nucleus to the total light of the nebula” and such broad lines were observed to be typical only of spiral galaxies with a strong nuclear emission. Galaxies with such features are now called *Seyfert galaxies*, and, since Seyfert’s observations, many other different properties have been observed in galaxies with strong nuclear emission (luminosities of active galaxies can reach 10^{48} erg/s). The classification of Active Galactic Nuclei (AGN) is now very complex and more details on the peculiarities of different classes of AGN are presented in §1.3. The point that we want to stress here is that the only possible explanation for the powerful emission coming from the nuclei of active galaxies is the presence of an accreting massive black hole. The idea of black holes being the engines of AGN was for the first time suggested by Salpeter (1964), Zel’Dovich (1964) and then by Lynden-Bell (1969), who ruled

¹Supermassive black holes are black holes with mass in the range of $10^6 - 10^9 M_{\odot}$. From now on, unless otherwise stated, when referring to “black holes” (BHs), we will always refer to supermassive black holes.

out the hypothesis that powerful nuclear emission is due to a very dense star cluster, and suggested a model in which a massive black hole is the central engine.

AGN have thus been the first indirect evidence for black holes of $10^6 - 10^9 M_{\odot}$ residing in galactic nuclei.

1.1.2 Supermassive black holes and their gravitational influence

The mass of supermassive black holes is a very small fraction of the total mass of the galaxy they reside in. Also, in terms of physical size, black holes are many orders of magnitudes smaller than their host galaxy. The Schwarzschild radius of a black hole of $10^8 M_{\odot}$, for example, is $\sim 3 \times 10^8$ km, which is approximately 10^{-5} pc. As we have mentioned above and as further discussed in the next sections, despite its small dimensions with respect to the host galaxy, the luminosity emitted by an accreting black hole can be higher than that of the galaxy itself, and this energetic output can strongly influence its surroundings up to cluster scales (hundreds of kpc). The gravitational influence of a black hole is, instead, very important in the central region of a galaxy, and its effects provide some of the best evidence for the existence of supermassive black holes. The region around a black hole that experiences the BH gravitational potential is defined by the “radius of influence”, given by $r_i = GM_{\text{BH}}/\sigma_*^2$, where σ_* is the stellar velocity dispersion. For a black hole of $10^8 M_{\odot}$ sitting in a galaxy with $\sigma_* \sim 200 \text{ km s}^{-1}$, the radius of influence r_i is ~ 10 pc. Trajectories of stars and gas clouds in the central region of a galaxy, if Keplerian, indicate the presence of a central potential generated by a “point-mass”. Searches of stars with such dynamical behaviour have been successful starting from the early '80s, with the observations of the kinematics of stars, gas clouds and masers² around the center of nearby galaxies, such as M31 and M32 (see the review of Kormendy 2004). The “massive-dark-object” around which stars and gas orbit, has to be so compact and massive, that black holes are the most plausible explanation. Such black holes could be the “quiet” or “dead” counterparts of the active black holes that power AGN.

The beautiful case of Sagittarius A*

The best up-to-date proof of the existence of supermassive black holes at the center of galaxies comes from the observations of the nucleus of our own Galaxy. In the last two decades, thanks to infrared observations using interferometry and adaptive optics, two independent groups led respectively by Reinhard Genzel and Andrea Ghez, have followed the proper motion of a small cluster of stars around Sgr A*, a compact radio source at the center of the Galaxy. The stars lie very close to the center, at distances of few hundred astronomical units, and their velocities are so high that full orbits can be followed in a few years (see Figure 1.1). The source of the strong gravitational force that influences the motion of the surrounding stars resides in such a small region that any explanation other than a massive black hole can be safely excluded. The most recent estimates of the black hole mass point to $\sim 4 \times 10^6 M_{\odot}$ (Gillessen et al. 2010), and the radio emission from Sgr A* would come from the gas falling into the event horizon (e.g., Genzel & Karas 2007).

²A *maser* (microwave amplification by stimulated emission of radiation) is the light emission from clouds rich in molecules around young stars. The emission is coming from electrons that undergo a downward transition to a lower energy state when stimulated by photons with energy equal to the energy difference between the states.

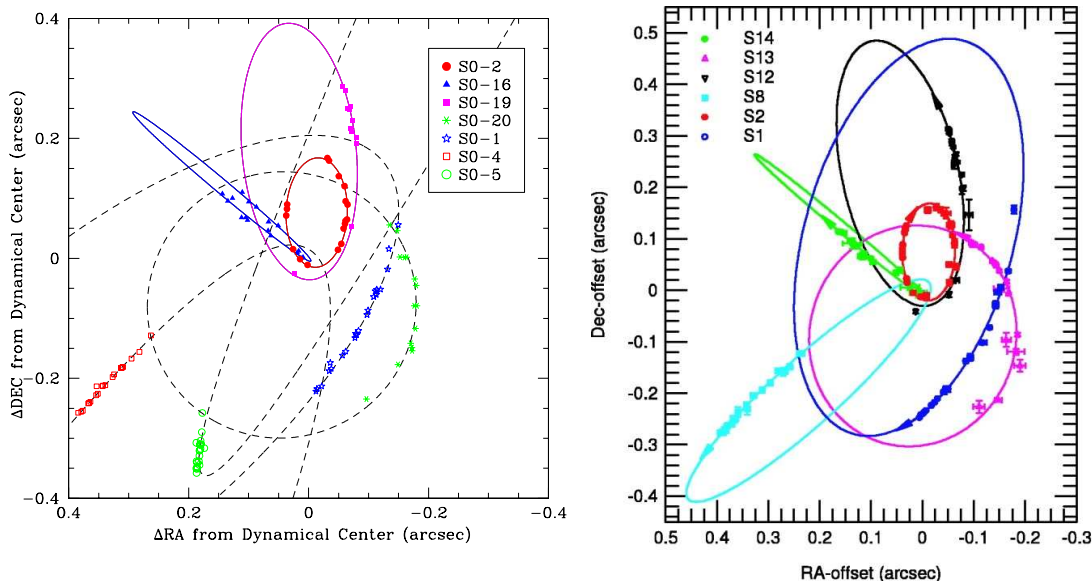


Figure 1.1: *Orbits of stars observed around Sgr A* with the Keck telescope from the UCLA group (left panel, Ghez et al. 2005) and with the ESO Very Large Telescope from the MPE collaboration (right panel, Eisenhauer et al. 2005).*

1.1.3 Hypervelocity Stars

In his seminal paper from 1988, Hills writes “a close but Newtonian encounter between a tightly bound binary and a $10^6 M_{\odot}$ black hole causes one binary component to become bound to the black hole and the other to be ejected at up to $4,000 \text{ km s}^{-1}$. The discovery of even one such hypervelocity star coming from the Galactic center would be nearly definitive evidence for a massive black hole” (Hills 1988). Hills, for the first time, calculated which would be the ejection speed of one of the components of a stellar binary system that interacts with a massive black hole in the Galactic center. Depending on the mass of the stars, on the mass of the black hole and on the eccentricity of the binary, stars could reach up to few thousands km s^{-1} , which is much higher than the escape velocity of the Galaxy. Hills pointed out that observations of such stars could be a definite proof of the existence of a supermassive black hole in the Galaxy. Yu & Tremaine (2003) analyzed also the possibility of hypervelocity stars from the encounter between an individual star and a black hole binary. The two processes would lead to similar event rates, which are expected to be observable. Hypervelocity stars have been detected in recent years, with velocities of several hundreds of km s^{-1} , larger than the escape velocity of the Galaxy, but not reaching the high values predicted theoretically (see e.g., Brown et al. 2009, for a review of the current observational results). It is now expected that the upcoming *GAIA* satellite (Perryman et al. 2001) will be able to detect more hypervelocity stars and provide further information about the Galactic center.

1.2 Properties of the black hole population

In this section we review the observed global properties of the population of massive black holes in the local Universe and as a function of redshift.

1.2.1 Techniques to estimate black hole masses

Before entering into the details of the properties of massive black holes, it is useful to review the techniques in use to estimate black hole masses:

- **Dynamical methods:** As described in §1.1.2, massive black holes have a gravitational sphere of influence that can extend to few pc. Within this region, the motion of stars and gas clouds is dictated by the potential of the central massive object. Observations of the dynamics of objects close to the nucleus, associated with theoretical models for the kinematics of stars around a central potential, give estimates of the mass associated to the nuclear black hole. While in our Galaxy stars can be individually resolved and followed over time (see §1.1.2), in other galaxies the nuclear stellar kinematics is measured using high-resolution spectroscopy. Stellar-dynamical estimates of black hole masses are the most precise and direct, despite the errors associated with the theoretical modeling of the stellar kinematics (for a review of this method and its successes, see Kormendy 2004). The drawback of this method is that it is very time-consuming, and can only be applied to nearby galaxies. For a broader census of black hole masses, less direct methods, as described below, are required.
- **Reverberation mapping and virial techniques:** It was first pointed out by Blandford & McKee (1982) that any variation in the ionizing emission of the central engine of Seyfert I galaxies and quasars would cause a variation both in the continuum and in the emission lines produced in Broad Line Regions (see the next section for a description of broad line regions, or BLR). The variations of the continuum and the emission lines would not be synchronous, but would happen with a time difference due to the travel time of the ionizing photons between the central source and the BLR. Therefore, a careful monitoring of the time delay between the variability in the continuum and the variability in the broad emission lines, can provide an estimate of the distance r_{BLR} between the source and the BLR. With simple virial arguments, the mass of the black hole is then given by:

$$M_{\text{BH}} \sim \frac{v^2 r_{\text{BLR}}}{G}, \quad (1.1)$$

where v is the characteristic velocity of the BLR clouds, estimated from the FWHM of the spectral emission lines. Throughout the years, many black hole masses have been estimated using this method (see, for example Peterson et al. 2004). Interestingly, when measuring time delays, Kaspi and collaborators (Kaspi et al. 2000), found that the radius of the BLR scales with the continuum luminosity at 5100 \AA : $r_{\text{BLR}} \propto L_{5100}^{0.7}$. This relation provides a quick way to estimate BLR sizes, since the luminosity can be obtained in a single observation (“single-epoch” detection). Similar relations have been found at other wavelengths, and can be used to estimate BH masses up to intermediate-high redshifts (Vestergaard 2002).

- **Scaling relations:** This is probably the most indirect method to estimate black hole masses, but it is important for statistical analysis of the global population. It relies on scaling relations between black hole masses and properties of the host galaxies, that are described in details in §1.4.1. These relations are first calibrated using direct measurements of black hole masses, and then the more easily accessible information of galaxy properties (such as luminosity and stellar velocity dispersion), are used to estimate the mass of the central objects.

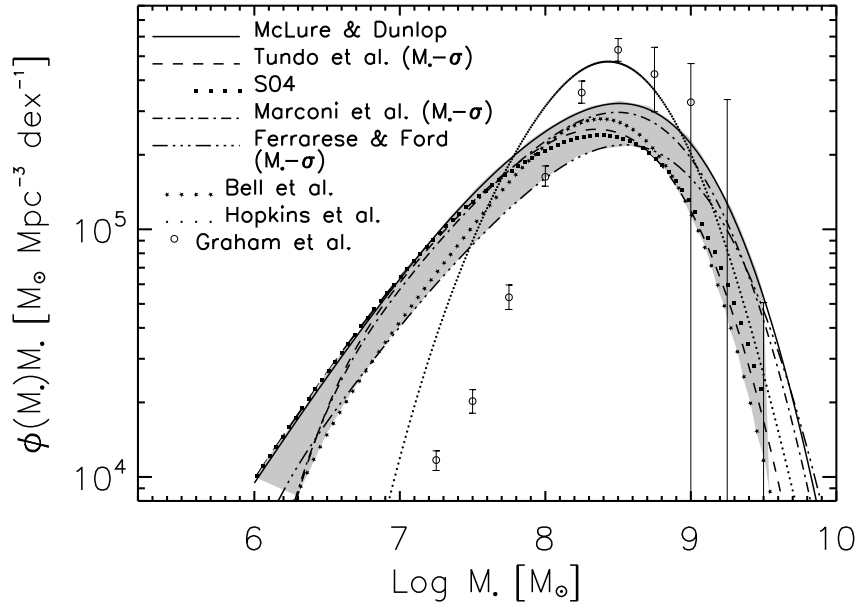


Figure 1.2: Various estimates of the black hole mass function in a compilation of Shankar et al. (2009b).

1.2.2 Black hole demographics

Thanks to constantly-improving observations and numerous available techniques to measure black hole masses, we now have a very good census of the black hole population in the local Universe.

Figure 1.2 shows various estimates of the black hole mass function in the most recent compilation of Shankar et al. (2009b). Masses in this broad range are typically derived from indirect measurements based on scaling relations between the black hole mass and properties of the host galaxy: from a wide census of bulge masses, luminosities or velocity dispersion it is, in fact, possible to derive the corresponding black hole masses, taking properly into account the errors in the used relations.

The black hole mass function is the most fundamental information we have on the black hole population in the local Universe and any model that tries to explain the origin and evolution of supermassive black holes has, as basic checkpoint, to match the local observed mass function.

How the mass function evolves with cosmic time is still not precisely known. Estimates of the black hole mass function at high redshift can be obtained using a continuity equation to combine the local black hole mass function and the AGN luminosity function as a function of redshift (e.g., Small & Blandford 1992; Merloni 2004; Shankar et al. 2009b). Alternatively, the black hole mass function can be derived from the luminosity function of early-type galaxies, assuming a relation between the luminosity of the spheroid and the black hole mass (e.g., Tamura et al. 2006, and §1.4.1 for a description of scaling relations between black hole mass and galaxy properties). Despite the uncertainties due to the strong assumptions behind each approach, those studies seem to converge on the result that the population of most massive black holes was already formed by $z \sim 1$ (see also the discussion in §1.3.2).

The integral of the mass function over all masses gives the black hole mass-density, which is now estimated to be around $\rho_{\text{BH}} \sim 4 \times 10^5 M_{\odot}/\text{Mpc}^3$ (see Graham & Driver 2007, for a recent discussion on different black hole mass-density estimates). In 1982, Soltan combined the local black hole mass

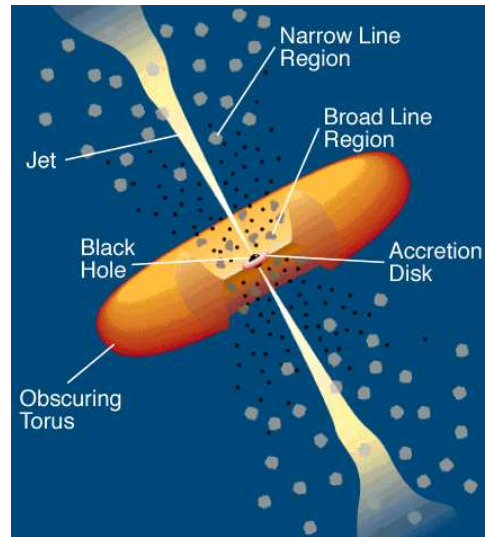


Figure 1.3: In this famous sketch from Urry & Padovani (1995), are shown the different components that constitute the basic structure of active nuclei. According to this unification scheme, different AGN properties depend primarily on the orientation of the galaxy with respect to the observer.

density with the quasar luminosity function and estimated that most of the mass in present-day black holes must have been accreted in phases of bright activity (Soltan 1982). Following this approach, many groups have analyzed the evolution of the AGN luminosity function to also impose limits on the *radiative efficiency* ϵ (see A.1.1 in Appendix A), finding that, across cosmic time, $\epsilon \sim 0.1$ (e.g., Yu & Tremaine 2002; Merloni et al. 2004; Shankar et al. 2004).

1.3 AGN and Quasars

In this section we summarize the most important properties of active black holes. After a brief overview of the *unification model* and of AGN classification, we describe recent observational results on the quasar luminosity function and clustering, which are important descriptors of the AGN population and that will be used throughout the next chapters to test theoretical models of black hole accretion.

1.3.1 Brief overview of AGN types

Active nuclei are commonly divided into different classes, depending on their spectral features, luminosity and variability. AGN show, in fact, many different properties and, according to the AGN *unification schemes*, these observed properties depend on the mass of the central engine, its life-stage, but primarily on the angle at which the accreting supermassive central hole is observed.

Figure 1.3 shows the famous sketch of the main components of an active nuclei from Urry & Padovani (1995). The central black hole is surrounded by an **accretion disk** which is, in turn, surrounded by high-velocity gas clouds, usually referred to as the **broad line region** (BLR), since it is from this gas that the very broad lines observed in a large fraction of AGN are thought to originate. This component of the nuclei is very important, especially for estimates of black hole

masses, as already mentioned in §1.2.1. The so-called **narrow line region** (NLR) is also composed of gas clouds, but they lie further away from the nucleus and are characterized by lower velocity and hence the narrow observed emission lines. Many AGN are also optically-obscured, and the gas and dust that hide the nuclear region are thought to be distributed in a **torus**-like axisymmetric structure. Typical of AGN are also jets of material accelerated from the very central region up to relativistic speeds, and these jets can extend up to a few hundreds of kpc.

A first simple AGN classification is based on the type of lines present in the spectra. **Type 1 AGN** are characterized both by narrow and broad lines in their spectra, suggesting that the observer is able to look directly into the region of the accretion disk. Type 1 AGN are, in fact, also characterized by a very bright continuum, which is the light emitted by the very central region. **Type 2 AGN**, instead, have spectra featuring only narrow lines and a much weaker continuum. The torus is probably obscuring the central region, and only the emission lines from the slower clouds of gas far from the center are visible. Type 1 AGN also emit a large fraction of their light ($\sim 10\%$) in the optical, whereas this fraction is much lower for type 2 AGN.

Seyfert galaxies, observed by Carl Seyfert as mentioned in §1.1.1, are divided in Seyfert 1 and Seyfert 2, based on the above classification. In the present-day nomenclature, **quasars**³ differ from Seyfert I galaxies mainly in the luminosity, with quasars being much brighter and able to outshine the host galaxy completely. The observational cut-off between the two populations is usually $M_V = -23$ mag.

Another perspective on an AGN and its host galaxy is shown in Figure 1.4. In this sketch, the basic components of an AGN and its host galaxy are shown in logarithmic scale. This schematic picture wants to emphasize the many order of magnitudes in scales covered by the AGN and the galaxy.

1.3.2 The Luminosity Function

Whereas the mass function is the basic descriptor of black hole demographics, the luminosity function of active nuclei is essential to understand the properties of the AGN population, and how this population evolves with redshift. Also, because the masses of “dormant” black holes can not be estimated at high redshift, the AGN luminosity function gives a first order indication of the evolution of the mass function (see the discussion in §1.2.2) and it provides essential constraints for theoretical models that try to explain the cosmological evolution of massive black holes.

It is important to determine the luminosity function in different bands, since different bands capture the emission from different types of AGN. In addition, the bolometric luminosity function gives information on the total mass that is being accreted onto black holes at any given time.

In Figure 1.5, a compilation of luminosity functions in different bands, combined to estimate the bolometric luminosity function as function of redshift, from Hopkins et al. (2007b) is shown. Throughout the next chapters, this estimate of the luminosity function will be used to test our theoretical models for black hole accretion across cosmic time.

The anti-hierarchical growth of massive black holes

For a long time now it has been known that the number density of quasars is higher at higher redshifts than today, with a peak at $z \sim 2$. In more recent years, X-ray observations have also shown that AGN with high X-ray luminosities are more common at higher redshift with respect

³From now on, with the term *quasar* we will usually refer generally to the brightest AGN population.

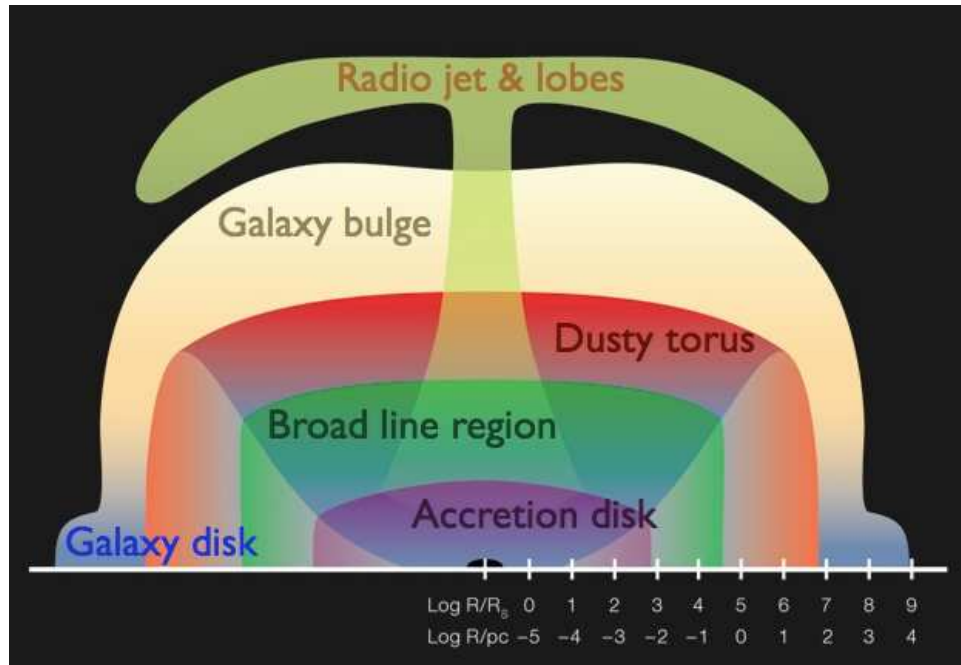


Figure 1.4: Schematic view of the basic components of an AGN embedded in the host galaxy in logarithmic scales. (courtesy of A. Merloni, S. Bonoli and the ESO graphics department).

to their low-luminosity counterparts (Steffen et al. 2003; Cowie et al. 2003; Cattaneo & Bernardi 2003; Ueda et al. 2003; Hasinger et al. 2005), as illustrated in the left panel of Figure 1.6. Recently, the same conclusions have been obtained also with optical data (Croom et al. 2009), as shown in the right panel of the same figure. Heckman et al. (2004), using optical data from SDSS, found that at low redshift only BHs with a mass $\lesssim 10^7 M_{\odot}$ are actively growing. Combined, these observations suggest that supermassive black holes grow “anti-hierarchically”: the more massive BHs were already in place at high redshift, and since then the accretion activity has shifted to smaller objects.

1.3.3 Quasar clustering

While the luminosity function indicates how the total energy budget is distributed across sources of different luminosities, clustering analysis provides information on how the sources are distributed on the sky and which is their environment. In fact, the clustering power of observed AGN can be compared with galaxy clustering or the clustering of simulated dark matter haloes to infer in which type of environment AGN reside. We refer to Appendix B for a description of clustering statistics.

A matching between quasar clustering and halo clustering can also be used to estimate quasar lifetime, as first suggested by Cole & Kaiser (1989) and later discussed in details by Haiman & Hui (2001) and Martini & Weinberg (2001a). The principle on which this conjecture is based is very simple: if quasars are strongly clustered, their hosts must be rare objects, and therefore they must also be long events in order to account for the total quasar luminosity density observed. If, on the other hand, their clustering is comparable to the clustering of small dark matter haloes, their hosts must be much more common, and their luminous phases must therefore have short duration.

A detailed investigation of the clustering properties of AGN have become possible with the

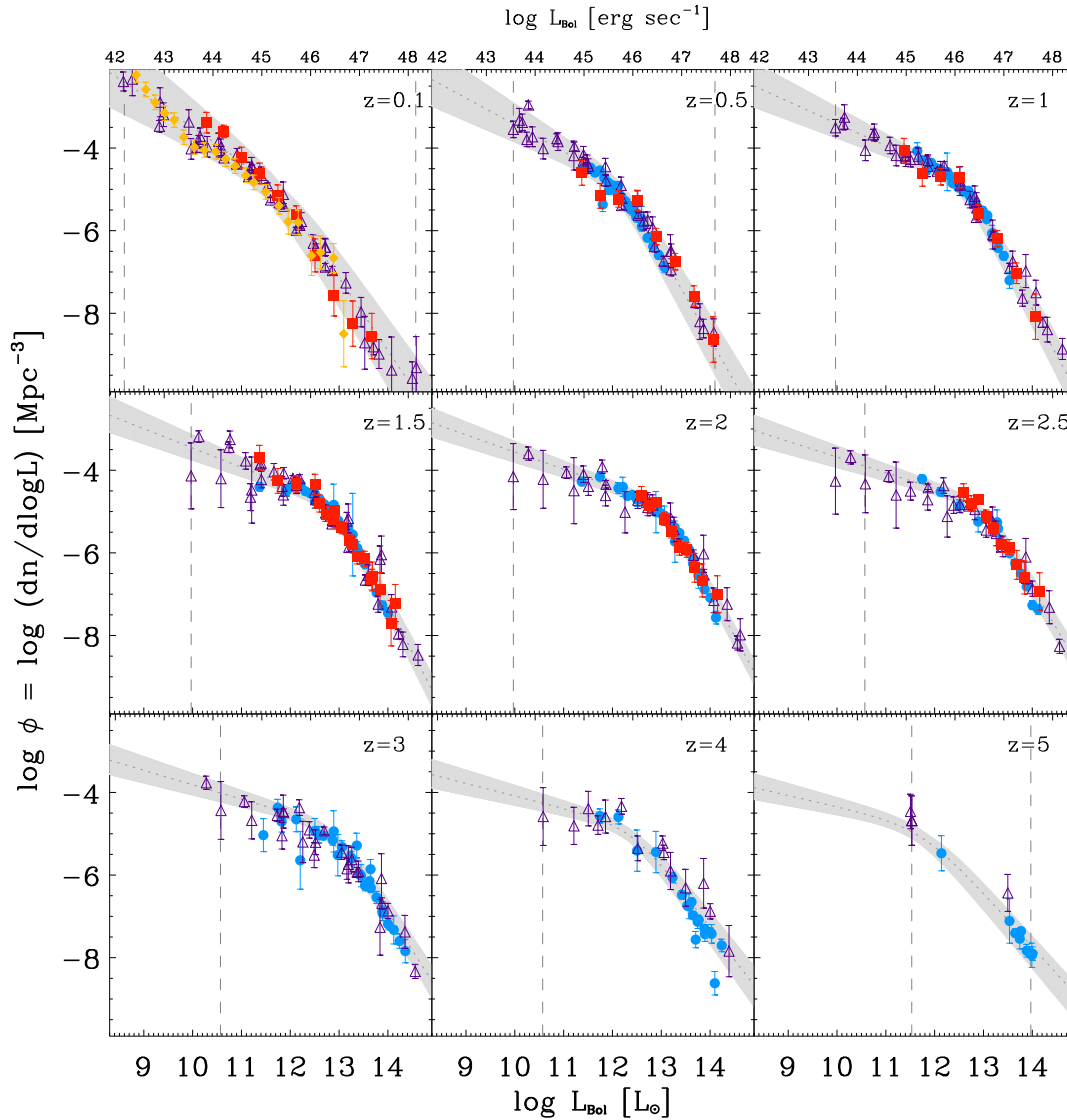


Figure 1.5: Bolometric AGN luminosity function (gray band) as a function of redshift, as calculated by Hopkins et al. (2007b). The different symbols and colors refer to different bands from which data have been extracted: solid blue circles are optical data, filled red squares infrared, purple triangle are soft and hard X-ray data and the filled orange diamonds are luminosities from emission lines. The vertical dashed lines bracket the observational limits. We refer the reader to Hopkins et al. (2007b) for a more detailed description of the data and methodology used to extract the bolometric best-fit luminosity function.

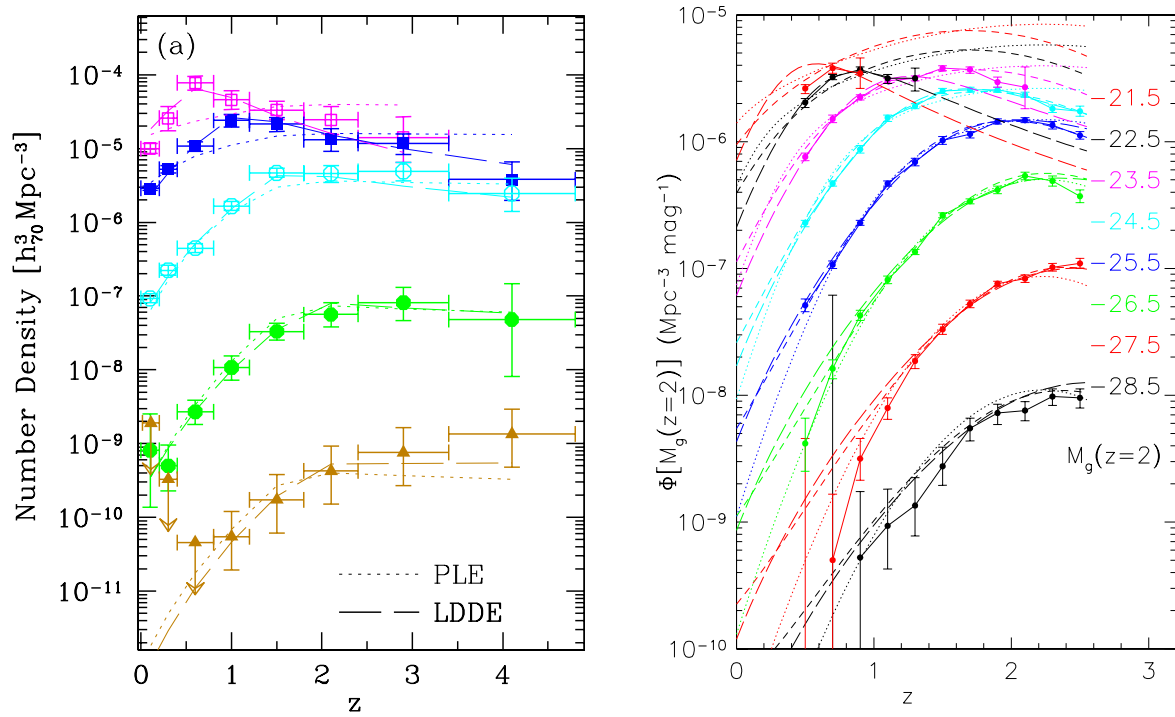


Figure 1.6: Redshift evolution of the AGN luminosity density. The left panel is from the X-ray luminosity function (Hasinger et al. 2005) and the right figure is from the optical one (Croom et al. 2009). In both bands low-luminosity objects have their peak in number density at lower redshifts with respect to the most luminous ones.

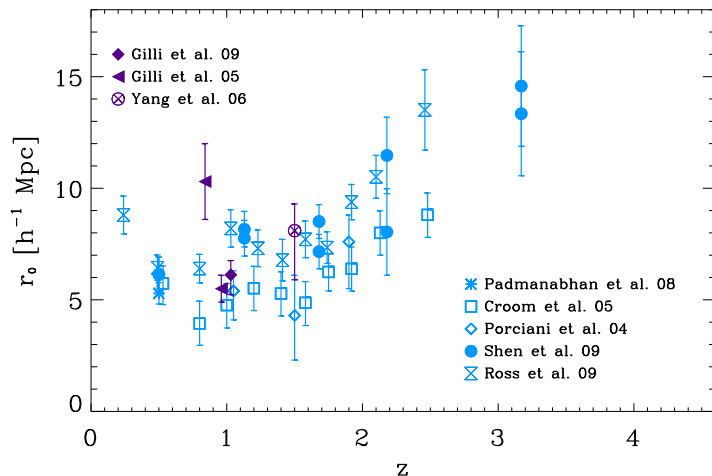


Figure 1.7: *Correlation length as a function of redshift as observed by different groups. The purple points are for X-ray data, while the blue ones are for optical quasars. This figure wants to show the general trend of r_0 with redshift, and the general agreement between different observations, but the comparison has not to be taken quantitatively, since the surveys luminosity cuts and the fitting procedure to calculate r_0 vary from group to group. Also, note that the high point from Gilli et al. (2005) is from the CDFS, while the lower point from the CDFS. Also, at each redshift Shen et al. (2009b) quote two values for the bias, which come from including or excluding negative points on the correlation function in the fitting procedure.*

observation of thousands of quasars by the wide-field surveys like SDSS and 2dFQSO (York et al. 2000; Croom et al. 2004). Croom et al. (2005) and Porciani et al. (2004) calculated the correlation function of quasars observed in 2dF in the redshift range $0.5 \lesssim z \lesssim 2$. Both groups found that the clustering strength is an increasing function of redshift, but that it does not depend significantly on quasar luminosity. The inferred values of the bias⁴ suggest that quasars of the observed luminosities are hosted by haloes of a few $10^{12} h^{-1} M_{\odot}$, which remains approximately constant with redshift, since haloes of a fixed mass are progressively more clustered towards higher redshift. Following the approach of Haiman & Hui (2001) and Martini & Weinberg (2001a), the estimated quasar lifetime would be a few 10^7 yr, reaching $\sim 10^8$ yr at the highest observed redshifts. More recent studies on larger samples and at different redshifts have confirmed these results (Shen et al. 2007; Myers et al. 2007a; Coil et al. 2007; da Ângela et al. 2008; Padmanabhan et al. 2008; Ross et al. 2008). However, the magnitude range covered by these surveys is typically quite narrow, and this may explain the lack of evidence for a significant dependence of clustering on luminosity. When Shen et al. (2009b) analyze the clustering of the 10% brightest objects of their sample, they find that these quasars have a higher bias compared to the full sample.

On the X-ray side, only recently large enough samples have become available for a statistically reliable clustering analysis. Gilli et al. (2005) have used the Chandra Deep Fields North and South (CDFN & CDFS) to measure the correlation power of X-ray selected AGN, and found very different correlation lengths (defined in the two fields: while AGN in the CDFN have a correlation power similar to the one observed for optical quasars, the objects in the CDFS have a much higher

⁴The *bias* is usually defined as the square-root of the ratio between the clustering power of the objects under analysis and that of the dark matter, see the definition B.1 and the related discussion in Appendix B.

correlation length⁵. This discrepancy is probably due to cosmic variance⁶, but see Marulli et al. (2009) for a theoretical discussion on this. Similar results as for the CDFN have been found for the CLASXS survey (Yang et al. 2006) and the XMM-COSMOS field (Gilli et al. 2009).

In Figure 1.7 the correlation length of AGN observed with various surveys in different bands is shown as a function of redshift.

1.4 The interaction between black holes and their host galaxies

We review in this section the relations observed between the mass of the central black hole and the host galaxy, and the main properties of AGN feedback.

1.4.1 Scaling relations

At the end of the last century, when stellar-dynamical measurements of black hole masses became available, interesting correlations between M_{BH} and properties of the host galaxies were found. Kormendy & Richstone (1995) were the first to point out that “black hole masses are proportional to the mass of the bulge component”. Few years later, Magorrian and collaborators combined dynamical models with kinematics data of 36 nearby galaxies to estimate black hole masses and calculate that the mass of the central object is ~ 0.006 times the mass of the stellar component of the host galaxy (Magorrian et al. 1998). At the turn of the new century, a new important correlation was found: Ferrarese & Merritt and Gebhardt and collaborators, discovered that the black hole mass is related also to the stellar velocity dispersion σ_* of the host (Ferrarese & Merritt 2000; Gebhardt et al. 2000), approximately as $M_{\text{BH}} \propto \sigma_*^\alpha$, where $\alpha \sim 4$, and with a scatter smaller than the one observed for the $M_{\text{BH}} - M_{\text{Bulge}}$ relation. In the following years, a lot of effort has been invested in measuring the precise slope and scatter of these relations (e.g. Tremaine et al. 2002; Marconi et al. 2004), and more relations were suggested, such as the ones between the black hole mass and the Sérsic index⁷ of the galaxy density profile (Graham et al. 2001) and even between the black hole mass and the mass of the host dark matter halo (Ferrarese 2002; Baes et al. 2003). In Figure 1.8 the $M_{\text{BH}} - \sigma_*$ and $M_{\text{BH}} - M_{\text{Bulge}}$ relations are shown using data from different groups, as indicated in the caption.

More recently, Hopkins et al. (2007a) introduced a “fundamental plane” for black holes, derived using both observational data and the outputs of hydrodynamical simulations of galaxy mergers. This is a relation that connects the black hole mass with both the stellar mass and the velocity dispersion of the host galaxy, expressed as:

$$\log(M_{\text{BH}}/M_\odot) = 7.93 + 0.72 \log(M_{11}^*) + 1.4 \log(\sigma_{200}), \quad (1.2)$$

where M_{11}^* is the galaxy stellar mass in units of $10^{11} M_\odot$, and σ_{200} is the bulge velocity dispersion in units of 200 km s^{-1} .

⁵The *correlation length* is, by definition, the scale at which the two-point correlation function is equal to unity, see Equation (B.3) in Appendix B.

⁶*Cosmic variance* is an effect that could arise when the portion of the Universe under examination is too small to be a statistically representative region of the entire Universe. A sample which is too small might, in fact, contain information that is biased with respect to the global statistics of the Universe.

⁷The *Sérsic index* n indicates the steepness of the density profile of a galaxy, usually expressed as: $I(R) \propto e^{-R^{1/n}}$, where $I(R)$ is the surface brightness, or projected density profile, as a function of the radial distance R (de Vaucouleurs 1948; Sérsic 1968).

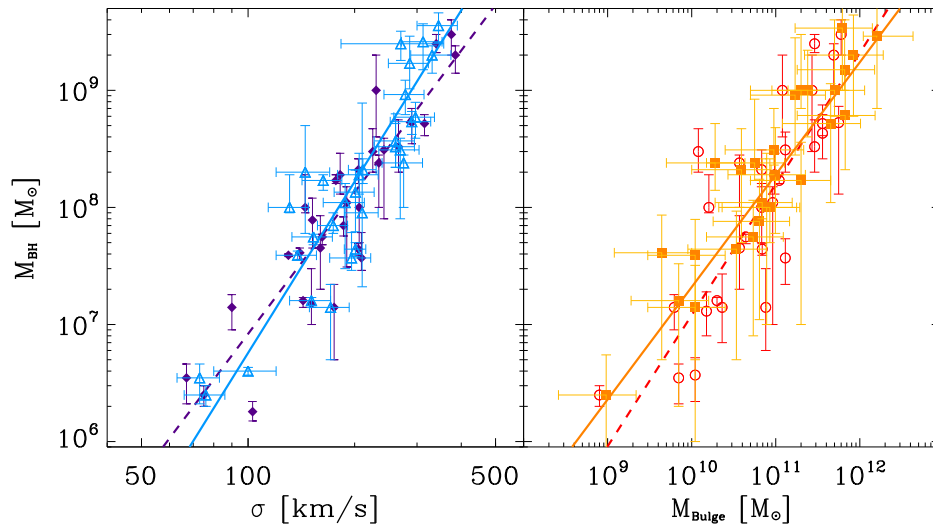


Figure 1.8: Example of scaling relations between the black hole mass and the stellar velocity dispersion (left panel) and bulge mass (right panel). In the left panel, the filled purple diamonds are from Tremaine et al. (2002), with the corresponding best-fit correlation represented by the dashed line. The blue open triangles are data from Ferrarese & Ford (2005), with best-fit given by the solid line. In the right panel, the filled orange squares are data of Marconi & Hunt (2003) (the solid line is their best fit derived from their best sample) and the open red circles are from Häring & Rix (2004), with dashed curve as best-fit.

Beyond the controversy of which relation is tighter, or which is the precise value of the slope, the important message coming from these observations is that there is a fundamental link between a galaxy and its central black hole, despite the large differences in mass and spatial scales of the two objects (a black hole, however massive, is a tiny fraction of the mass of the host, and occupies a region which is many orders of magnitudes smaller than typical galactic scales). Whether black holes are “passive” actors in shaping these relations, or actively regulate their own growth, is still a matter of debate. Towards the end of this section, a review of some physical processes that are probably important in establishing this relation is given.

Scaling relations at high redshift

For a full understanding of how black holes and galaxies evolved together, it is necessary to understand how and when the above relations originated and how they evolve with redshift. Observationally, this is still an open question. Many groups are working on this subject, but so far the results have not been conclusive, mainly due to the difficulty in measuring black hole masses and galaxy properties at the same time. In the very distant Universe, black hole masses can be estimated only for active galaxies, using virial techniques or similar methods based on the luminosity produced by the central black hole. But, because of observational limits, only the most luminous AGN are selected, with the consequence that the luminosity of the host galaxy is often outshone by the luminosity of the active nucleus. Treu and collaborators have used very high signal-to-noise spectra from the *Keck* telescope combined with high-resolution images from the *Hubble Space Telescope* to calculate both the black hole mass and galaxy properties in a sample of Seyfert I galaxies at $z \sim 0.4$,

and found that the ratio between black hole and bulge mass evolves as $\sim (1+z)^{1.5\pm 1.0}$ (Treu et al. 2004, 2007). The same authors detected evolution also in the $M_{\text{BH}} - \sigma_*$ relation, with smaller velocity dispersion, for a given black hole mass, when going back in time. Peng et al. (2006) have analyzed the redshift evolution of the $M_{\text{BH}} - M_{\text{Bulge}}$ ratio using data of gravitationally-lensed quasar hosts at $1 \lesssim z \lesssim 4.5$: thanks to the lens amplification, properties of the host become more accessible and these authors find that at $z > 1$ black holes are about twice as massive with respect to the host galaxy as predicted by the local relation, and, at $z \gtrsim 1.7$, the ratio $M_{\text{BH}}/M_{\text{Bulge}}$ is four times larger than today. Merloni et al. (2010) used instead the multi-wavelength data of the zCOSMOS survey to disentangle the stellar and the nuclear contribution in AGN at $1 \lesssim z \lesssim 2.2$, finding a milder evolution, with $M_{\text{BH}}/M_{\text{Bulge}} \sim (1+z)^{0.68\pm 0.12}$.

Other groups have analyzed the evolution of the $M_{\text{BH}}/M_{\text{Bulge}}$ ratio using a very different approach, based on global statistical properties of the black hole and stellar populations. Comparing the evolution of the black hole mass and accretion rate density on one side, and the stellar mass and star formation rate density on the other, Merloni et al. (2004) found a moderate redshift evolution in the black hole and stellar mass ratio, in favor of larger black hole masses per stellar mass with respect to local values (see also, Shankar et al. 2009a). With a similar approach, Hopkins et al. (2006b) exclude a strong evolution in the $M_{\text{BH}}/M_{\text{Bulge}}$ ratio.

Finally, using data of large-scale quasar clustering, Fine et al. (2006) estimated the evolution of the ratio between the black hole mass and host dark matter halo mass finding: $M_{\text{BH}}/M_{\text{Halo}} \sim (1+z)^{2.5\pm 1.8}$.

On the theoretical side, Robertson et al. (2006) examined the evolution of the $M_{\text{BH}} - \sigma_*$ relation using a large number of simulations of isolated galaxy mergers, with galaxy properties re-scaled to the redshifts of interests. These authors found that the slope of the relation, up to $z \sim 6$, is essentially insensitive to the redshift-dependent properties of the host galaxies. Using similar numerical models, Johansson et al. (2009) found that BHs do not evolve onto the $M_{\text{BH}} - M_{\text{Bulge}}$ relation at the end of a merger event, if they were sitting above the relation before the merger. This result would rule out scenarios in which black holes grow much before their host bulge.

As mentioned above, an observational determination of the evolution of the scaling relations is essential to understand how black holes and their host galaxies co-evolve. Most theoretical models for the joint evolution of black holes and galaxies use the local relations to constrain their free parameters, but the redshift evolution of these relations remains an uncertain prediction. Hopefully future generations of observational facilities will be able to unveil more details on the redshift-dependence of these scalings.

1.4.2 AGN feedback

The energy released by an accreting black hole can easily exceed the binding energy of the host galaxy. How the emitted energy couples with the surrounding, is, though, not a trivial problem.

In their 1998 paper, Silk & Rees introduce a simple model in which a wind from a black hole in a “quasar” phase mechanically couples with the surrounding gas, halting star formation, regulating the growth of the black hole itself and naturally explaining the scaling relation between the black hole and the host galaxy mass (Silk & Rees 1998).

Such “self-regulated” growth of massive black holes has also been included in hydrodynamical simulations of galaxy mergers, successfully reproducing the $M_{\text{BH}} - \sigma_*$ relation by assuming that a fraction of the radiative luminosity from the accreting central black hole is able to heat the surrounding gas (Di Matteo et al. 2005; Springel et al. 2005b, and see also the discussion in §1.5.2

and Figure 1.9).

Indeed, there are different forms in which the energy output of an accreting hole can couple and influence the surrounding medium: a *radiative* or wind output would couple thermally with the gas, while in a *kinetic* mode the jets generated close to the accretion disk are able to mechanically push the gas out. While the first is now assumed to work when black holes accrete cold gas at high rates, the second is often invoked to halt the cooling of hot gas at the center of galaxy clusters. The latter is connected to the so-called “cooling-flow” problem, which is the discrepancy between the expected high cooling at the center of galaxy clusters, and the lack of observational evidence for the expected high mass deposition rates from cooling (Cowie & Binney 1977; Fabian & Nulsen 1977). The lack of significant amounts of cold gas in galaxy clusters is often explained invoking the heating mechanism of central AGN (e.g., Binney & Tabor 1995; Churazov et al. 2002; Brüggén & Kaiser 2002; Omma et al. 2004; Sijacki & Springel 2006; McNamara & Nulsen 2007).

1.5 The cosmological evolution of supermassive black holes

In the previous section we have described the tight connection observed between black holes and their host galaxies. The discovery of scaling relations has stimulated substantial effort in trying to understand how black holes and galaxies co-evolve and mutually influence each other across cosmic time. In this section we review which could be the basic stages of the life of a supermassive black hole, from its birth to the phases of bright activity.

1.5.1 Seed Black Holes

A subject of intense theoretical investigation is the origin of supermassive black holes. Two main theories are currently being debated: seeds of massive black holes could have been the remnants of Pop III stars (e.g., Bond et al. 1984; Madau & Rees 2001; Heger & Woosley 2002) or they could have originated from the direct collapse of low-angular momentum clouds of pristine gas (Haehnelt & Rees 1993; Loeb & Rasio 1994; Koushiappas et al. 2004; Begelman et al. 2006; Begelman 2010). In the first case the mass of the seed is estimated to be of the order of $10^2 - 10^3 M_{\odot}$, much less than what could be the outcome of low-angular momentum gas collapse ($\sim 10^5 M_{\odot}$).

Unfortunately, due to exponential growth during accretion, it is very difficult to use the local population of massive holes to recover information about their original mass before the onset of accretion. On the theoretical side, simulations are being carried out to investigate which model for massive BH formation is most plausible (e.g., Bromm & Loeb 2003; Alvarez et al. 2008). Observationally, these models for primordial BHs will hopefully be tested in the near future either directly through gravitational wave detection (Sesana et al. 2005; Koushiappas & Zentner 2006), or indirectly by, for example, looking at the effect that primordial accreting BHs might have had on the reionization of the intergalactic medium (e.g., Ricotti et al. 2005; Ripamonti et al. 2008).

1.5.2 Triggering black hole accretion

To fall onto the accretion disk, the gas present in a galaxy has to efficiently lose angular momentum and travel several orders of magnitude in scales from thousands of parsecs down to a few astronomical units. Which physical mechanisms are able to channel gas to the very nuclear region of a galaxy is still not clear (see, for example, the review of Jogee 2006). From a theoretical point of view, the main problem is to simulate such a large dynamical range.

In the standard Λ CDM structure formation model, small objects form first from small overdensities of the density field, and then grow by accretion and mergers, in a “hierarchical” or “bottom-up” fashion (White & Rees 1978; White & Frenk 1991). In this context, galaxy mergers play a primary role in triggering star formation and modifying the morphological galaxy properties. Numerical simulations have, in fact, shown that elliptical galaxies can be the remnant of the merger of two disk galaxies (e.g., Barnes 1988; Hernquist 1992; Naab & Burkert 1999; Springel et al. 2005a). Simulations have also shown that in gas-rich mergers starbursts occur and gas is channeled toward the nuclei of the merging galaxies through gravitational torques (Negroponte & White 1983; Barnes & Hernquist 1991; Mihos & Hernquist 1994, 1996; Barnes & Hernquist 1996). The tight relations observed in the local Universe between black hole masses and the host bulge properties (described in §1.4.1) suggest that bulges and black holes might form during the same events, and gas-rich galaxy mergers have been considered as the physical processes that could simultaneously explain the formation of spheroids and the growth of the nuclear black hole. In a seminal work at the beginning of this century, Kauffmann & Haehnelt analyzed the evolution of the black hole population in a full cosmological context, assuming that galaxy mergers were the main mechanism responsible for efficient black hole growth (Kauffmann & Haehnelt 2000). These authors were able to reproduce some of the main properties of the black hole and quasar population, demonstrating the viability of their basic assumptions. In the following years, more work has been done in this direction, using analytical, semi-analytical and fully numerical models (e.g., Wyithe & Loeb 2002; Volonteri et al. 2003; Granato et al. 2004; Springel et al. 2005b; Croton et al. 2006; Malbon et al. 2007; Monaco et al. 2007; Escala 2007). Another breakthrough in the numerical modeling of black hole accretion in the context of galaxy formation has been achieved by di Matteo, Springel and collaborators, who were able to form spheroids and obtain the $M_{\text{BH}} - \sigma_*$ relation using hydro-simulations of isolated gas-rich mergers including feedback from the accreting black hole (see Figure 1.9 and Springel et al. (2005b); Di Matteo et al. (2005).

On the observational side, already in 1988 Sanders and collaborators suggested a connection between quasars and starburst galaxies with signatures of recent mergers (Sanders et al. 1988). Morphologically-disturbed galaxies with a young stellar population seem indeed to be the typical hosts of AGN with high mass accretion rates (e.g., Sánchez et al. 2004; Jahnke et al. 2004; Bennert et al. 2008; Hutchings et al. 2009), whereas it has been observed that low-luminosity AGN seem to be hosted by galaxies with an older population that do not necessarily show signs of recent merger activity (e.g., Kauffmann et al. 2003; Silverman et al. 2008).

While galaxy mergers seem then to be responsible for triggering the activity of very bright AGN and quasars, low-luminosity AGN are possibly being triggered by other mechanisms, such as stellar winds from supernovae explosions or bars produced in galactic disks by gravitational instabilities (e.g., Jogee 2006; Ciotti & Ostriker 2007), although this division between “external” and “internal” triggers might be not as simple (Strand et al. 2008; Li et al. 2008; Georgakakis et al. 2009).

1.5.3 Black hole mergers

During galaxy merger events, the two black holes sitting at the center of each host will be dragged towards the center of the merger remnant because of dynamical friction. Eventually, the two black holes form a binary system, which is defined “hard” if the binding energy per unit mass ($G\mu/2a$) is larger than σ^2 (where μ is the reduced mass of the binary and a the semi-major axis, see, e.g., Merritt 2004). For typical supermassive black holes, the value of a in this limit is a few parsecs. A binary system is able to “harden” when third objects interact with it: in the process called *gravitational*

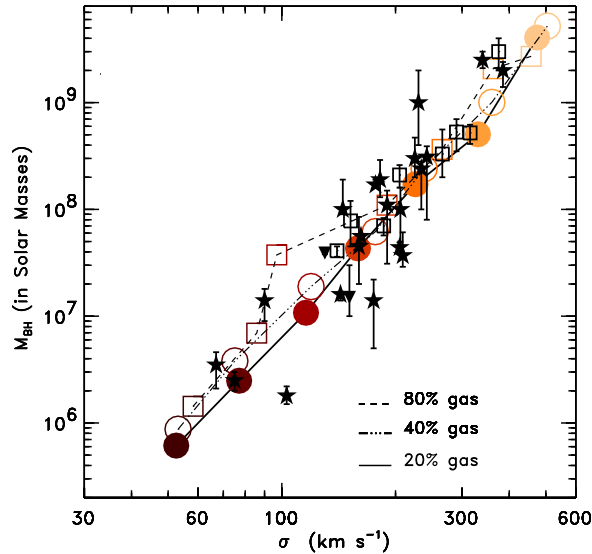


Figure 1.9: $M_{\text{BH}} - \sigma_*$ relation obtained from a series of isolated gas-rich galaxy mergers which include quasar feedback. The gas fractions included in the simulations vary from 20 to 80% (as indicated on the plot). The black points are from observational data (from stars, maser and gas kinematics). The red color shades indicate different initial total mass of the galaxy. From Di Matteo et al. (2005).

slingshot, the infalling objects get accelerated by the binary, which increases its binding energy. Two black holes can eventually coalesce when their separation is small enough for gravitational wave emission to become efficient. If the emission of gravitational waves is asymmetric, the binary experiences a recoil, with velocities that depend on the spin of the two black holes (e.g., Dotti et al. 2010). The separation at which gravitational wave emission becomes important is of the order of a few percent of a parsec, and it is still not clear whether enough material crosses the nuclear region of a galaxy for the binary to harden to such small scales. Numerical simulations have shown that encounters with stars alone might not be enough to harden the binary to very small scales (e.g., Milosavljević & Merritt 2003; Makino & Funato 2004). If, however, gas is present, the hardening process is facilitated and the final coalescence might take place on a short timescale (e.g., Escala et al. 2004; Mayer et al. 2008).

From an observational point of view, the lack of a statistically-large sample of binary black holes would suggest that the coalescence process is actually effective and black holes can merge in a relatively short time (see Komossa 2006, for a review on the observational evidences of binary black holes).

1.6 Outline of the thesis

The objective of this thesis is to test models in which bright AGN activity is triggered by galaxy mergers. As mentioned above, several observational results indicate that bright AGN reside in merger remnants.

To test the assumption that galaxy mergers are responsible for efficient black hole feeding, we

have used various numerical methods to model the AGN population across cosmic time, and we compared our model predictions with the most recent observational compilations of several global descriptors of the quasar population, such as luminosity functions and clustering statistics.

The thesis is divided as follows:

- **Chapter 2: Modeling the cosmological evolution of black holes and quasars**

In this chapter we describe our methodology to model the evolution of black holes in the context of galaxy formation. We also show tests for light curve models associated with single accretion events, and the general properties of the simulated black holes and quasars.

- **Chapter 3: The clustering of simulated quasars**

In this chapter we analyze the clustering properties of the quasars simulated with the procedure described in the previous chapter. We also analyze the properties of the dark environment and the duty cycle of our simulated quasar population.

- **Chapter 4: The *merger bias***

With the term “merger bias” we refer to any excess of large-scale clustering that recently-merged objects might have with respect to a population of objects with the same properties, but with no recent merger event. If such excess clustering exists, and if indeed quasars are triggered by galaxy mergers, the observed clustering could not be used to infer the environment quasars live in. In this chapter we analyze the significance of merger bias for simulated dark matter haloes, galaxies and quasars.

- **Chapter 5: The evolution of supermassive black holes in semi-analytical and hydrodynamic simulations**

This chapter is devoted to the description of first results of a study in which we compare directly the cosmological evolution of black holes and quasars as simulated with a semi-analytical model for galaxy formation and with hydrodynamical cosmological simulations.

- **Chapter 6: Summary and outlook**

In this final chapter we summarize the main findings of this thesis and present a brief outlook to future work.

Chapter 2

Modeling the cosmological evolution of black holes and quasars

In this chapter¹ we describe the procedure with which we model the evolution of black holes and quasars in a galaxy formation context. This modeling procedure will also be used in the next chapter to study the clustering properties of simulated quasars.

After a brief introduction (§2.1), in §2.2 we describe the most important physics of galaxy formation entering the semi-analytic model. In the same section we also describe the details of how we modeled the luminosity associated to each black hole accretion event using various light curve models. Then, in §2.3, the global properties of the black hole and quasar populations are presented. Specifically, we analyze the scaling relations, the fundamental plane and the mass function of BHs, and compare them with the most recent observational data. We also analyze the predicted evolution of the AGN luminosity function. While we find for the most part a very good agreement between predicted and observed BH properties, the semi-analytic model underestimates the number density of luminous AGN at high redshifts, independently of the adopted Eddington factor and accretion efficiency. However, an agreement with the observations is possible within the framework of our model, provided it is assumed that the cold gas fraction accreted by BHs at high redshifts is larger than at low redshifts.

Finally, in §2.4 we summarize the main findings of the work presented in this chapter.

2.1 Introduction

As discussed in §1.5, a co-evolution of BHs, AGN and galaxies is expected in the standard cosmological framework, where cosmic structures grow hierarchically via gravitational instability and merging events destabilize the gas at the galaxy centres, triggering star formation and BH mass accretion. In order to investigate this complex scenario, several models have been developed, based on either pure analytic approximations (see, e.g., Efstathiou & Rees 1988; Haehnelt & Rees 1993; Haiman & Loeb 1998; Percival & Miller 1999; Haiman & Menou 2000; Martini & Weinberg 2001b; Wyithe & Loeb 2003; Hatziminaoglou et al. 2003; Hopkins et al.

¹This chapter follows the paper *Modeling the cosmological co-evolution of supermassive black holes and galaxies I: BH scaling relations and the AGN luminosity function* by Federico Marulli, Silvia Bonoli, Enzo Branchini, Lauro Moscardini & Volker Springel (MNRAS, 385, 1846). Federico Marulli and Silvia Bonoli have been responsible for the bulk of the work, which Federico Marulli put together in its final form.

2007b), or semi-analytic ones (see, e.g., Kauffmann & Haehnelt 2000; Cavaliere & Vittorini 2002; Enoki et al. 2003; Volonteri et al. 2003; Granato et al. 2004; Springel et al. 2005c; Cattaneo et al. 2005; Croton et al. 2006; Malbon et al. 2007; Fontanot et al. 2006). Recently, thanks to the availability of unprecedented computational power, fully numerical models have also become available (see, e.g., Di Matteo et al. 2005; Springel et al. 2005b; Li et al. 2007; Sijacki et al. 2007; Di Matteo et al. 2008).

Simple analytic models in which AGN activity is only triggered by DM halo major mergers succeeded in quantitatively describing the observed evolution of the AGN number counts and luminosity at all but low redshifts, provided that some mechanism is advocated to inhibit accretion within massive haloes hosting bright AGN. However they fail in reproducing the observed AGN clustering at high redshifts (Marulli et al. 2006). Slightly more sophisticated semi-analytic models in which the halo merger history and associated BHs are followed by Monte Carlo realizations of the merger hierarchy, while the baryonic physics is neglected as well, can correctly reproduce both the AGN luminosity and clustering function at $z \gtrsim 1$ (Marulli et al. 2006), but the number density of faint AGN is significantly below observations, a clear indication that DM halo mergers cannot constitute the only trigger to accretion episodes in the local BH population (Marulli et al. 2007), and that in order to properly describe the cosmological evolution of BHs and AGN, the main baryonic phenomena involving the gas contents of DM halos cannot be neglected.

In this chapter we study the cosmological co-evolution of galaxies and their central BHs using a semi-analytical model developed on the outputs of the Millennium Simulation and described in detail in Croton et al. (2006) and De Lucia & Blaizot (2007). In this scenario, *radio mode* feedback from AGN at the centre of galaxy groups and clusters is invoked to prevent significant gas cooling in large halos, thus limiting the mass of the central galaxies and preventing them from forming stars at late times when their mass and morphology can still change through mergers. Thanks to this mechanism, Croton et al. (2006) demonstrated that such a model can simultaneously explain the low observed mass drop-out rate in cooling flows, the exponential cut-off in the bright-end of the galaxy luminosity function, and the bulge-dominated morphologies and stellar ages of the most massive galaxies in clusters.

Here we are interested in investigating how well this model can also reproduce the statistical properties of BHs and AGN. To do that, we extend the original model by adding new semi-analytical prescriptions to describe the BH mass accretion rate in the accretion episodes triggered by galaxy mergers, which fuel the *quasar mode*, and their conversion into radiation. We then analyze the scaling relations, the fundamental plane and the mass function of BHs, and compare them with the most recent observational data available. Finally, we compare the predicted AGN bolometric luminosity function with the observed one, and propose some modifications to the original semi-analytic assumptions to better fit the data.

2.2 The model

Our semi-analytic model for the co-evolution of DM haloes, galaxies and their central BHs consists of three ingredients, that we describe separately in this section: a numerical simulation to obtain the merger history of the DM haloes, a set of analytic prescriptions to trace the evolution of galaxies within their host haloes and a set of recipes to follow the BH accretion history and the AGN phenomenon.

2.2.1 Numerical simulation

In this work we use the outputs of the Millennium Simulation, which followed the dynamical evolution of $2160^3 \simeq 10^{10}$ DM particles with mass $8.6 \times 10^8 h^{-1} M_\odot$ in a periodic box of $500 h^{-1} \text{Mpc}$ on a side, in a ΛCDM “concordance” cosmological framework (Springel et al. 2005c). The computational box is large enough to include rare objects such as quasars or rich galaxy clusters, the largest of which contain about 3 million simulation particles at $z = 0$. At the same time, the mass resolution is high enough to resolve the DM halo of $0.1 L_\star$ galaxies with ~ 100 particles. The short-range gravitational force law is softened on the co-moving scale $5 h^{-1} \text{kpc}$ (Plummer-equivalent) which may be taken as the spatial resolution limit of the calculation. The cosmological parameters (the matter density parameter $\Omega_m = 0.25$, the baryon density parameter $\Omega_b = 0.045$, the Hubble parameter $h = H_0/100 \text{ km s}^{-1} \text{Mpc}^{-1} = 0.73$, the cosmological constant contribution to the density parameter $\Omega_\Lambda = 0.75$, the primordial spectral index $n = 1$, and the power spectrum normalization $\sigma_8 = 0.9$), are consistent with determinations from the combined analysis of the 2-degree Field Galaxy Redshift Survey (2dFGRS) (Colless et al. 2001) and first-year WMAP data (Spergel et al. 2003), as shown by Sánchez et al. (2006). We recall that the more recent analysis of the WMAP 3-year data (Spergel et al. 2007) suggests slightly different values (in particular smaller values for Ω_m , σ_8 and n). However, as demonstrated by Wang et al. (2007), due to the current modelling uncertainties, it is not possible to distinguish the two WMAP cosmologies on the basis of the observed galaxy properties, since the variations induced by acceptable modifications of the free parameters of the galaxy formation model are at least as large as those produced by the variation in the cosmological parameters.

The Millennium Simulation was carried out with a special version of the GADGET-2 code (Springel 2005), optimized for very low memory consumption, at the Computing Centre of the Max-Planck Society in Garching, Germany. We make use of hierarchical merging trees extracted from this simulation which encode the full formation history of DM haloes and subhalos, previously identified with, respectively, a friends-of-friends (FOF) group-finder and an extended version of the SUBFIND algorithm (Springel et al. 2001a). These trees constitute the backbone of our semi-analytic model, which is implemented during the post-processing phase: this allows us to simulate the wide range of baryonic processes occurring during the formation and evolution of galaxies and their central BHs.

2.2.2 Galaxy evolution

We use the galaxy formation model of Croton et al. (2006) as updated by De Lucia & Blaizot (2007). Although not in agreement with some properties of the red and blue galaxy populations (see, e.g., Weinmann et al. 2006; Kitzbichler & White 2007), this model is able to reproduce the overall observed properties of galaxies, i.e. the relations between stellar mass, gas mass and metallicity, the luminosity, colour and morphology distributions (Croton et al. 2006; De Lucia et al. 2006), the two-point galaxy correlation functions (Springel et al. 2005c), and the global galaxy luminosity and mass functions at high redshift (Kitzbichler & White 2007). We refer to the original papers for a full description of the numerical implementation of the model. In the following, we briefly recall the treatment of the physical processes involved in the galaxy evolution, and describe the prescriptions for the BH growth and the AGN evolution.

Following the standard paradigm set out by White & Frenk (1991) and adapted to high-resolution N-body simulations by Springel et al. (2001a), we assume that as a DM halo collapses,

a fraction $f_b = 0.17$ of its mass is in the form of baryons and collapses with it, consistent with the first-year WMAP result (Spergel et al. 2003). Initially, these baryons are in the form of a diffuse gas with primordial composition, but later they include gas in several phases as well as stars and heavy elements. Conventionally, with the simplifying assumption of an ideal gas which cools isobarically, the cooling time of the gas is computed as the ratio of its specific thermal energy to the cooling rate per unit volume,

$$t_{\text{cool}} = \frac{3}{2} \frac{\bar{\mu} m_p k T}{\rho_g(r) \Lambda(T, Z)}, \quad (2.1)$$

where $\bar{\mu} m_p$ is the mean particle mass, k is the Boltzmann constant, $\rho_g(r)$ is the hot gas density, and $\Lambda(T, Z)$ is the cooling function (Sutherland & Dopita 1993; Maio et al. 2007). Equation (2.1) is valid at temperature higher than $\sim 10^4$ K, where hydrogen and helium remain ionized and the number of particles remains approximately constant.

We assume the post-shock temperature of the infalling gas to be the virial temperature of the halo, $T = 35.9 (V_{\text{vir}}/\text{km s}^{-1})^2$ K, where V_{vir} is the halo virial velocity. Moreover, we assume that the hot gas within a static atmosphere has a simple ‘isothermal’ distribution,

$$\rho_g(r) = \frac{m_{\text{hot}}}{4\pi R_{\text{vir}} r^2}, \quad (2.2)$$

where m_{hot} is the total hot gas mass associated with the halo and is assumed to extend to its virial radius R_{vir} .

In order to estimate an instantaneous cooling rate onto the central object of a halo, given its current hot gas content, we define the cooling radius, r_{cool} , as the radius at which the local cooling time (assuming the structure of Equation (2.2)) is equal to the halo dynamical time, $R_{\text{vir}}/V_{\text{vir}} = 0.1 H(z)^{-1}$ (Springel et al. 2001b; De Lucia et al. 2004; Croton et al. 2006); here $H(z)$ represents the redshift evolution of the Hubble constant. The cooling rate can then be determined through the following continuity equation,

$$\dot{m}_{\text{cool}} = 4\pi \rho_g(r_{\text{cool}}) r_{\text{cool}}^2 \dot{r}_{\text{cool}}. \quad (2.3)$$

More details about our cooling prescriptions can be found in Croton et al. (2006).

The photo-ionization heating of the intergalactic medium suppresses the concentration of baryons in shallow potentials (Efstathiou 1992), and can be responsible of the inefficient accretion and cooling in low-mass haloes. Following Gnedin (2000), we model the effect of such photo-ionization heating by defining a characteristic mass scale, M_F , below which the gas fraction f_b is reduced relatively to the universal value:

$$f_b^{\text{halo}}(z, M_{\text{vir}}) = \frac{f_b^{\text{cosmic}}}{[1 + 0.26 M_F(z)/M_{\text{vir}}]^3}. \quad (2.4)$$

We adopt the $M_F(z)$ parameterization of Kravtsov et al. (2004), which results in a filtering mass M_F of $4 \times 10^9 M_\odot$ at the reionization epoch, and $3 \times 10^{10} M_\odot$ by the present day (but see Hoefl et al. 2006).

In the semi-analytic framework we use in this work, the star formation is assumed to occur at a rate given by:

$$\dot{m}_* = \alpha_{\text{SF}} (m_{\text{cold}} - m_{\text{crit}}) / t_{\text{dyn, disc}}, \quad (2.5)$$

where m_{cold} is the cold gas mass, $t_{\text{dyn,disc}}$ is the dynamical time of the galaxy, defined as the ratio between the disk radius and the virial velocity, m_{crit} corresponds to a critical value for the gas surface density (Kauffmann 1996; Kennicutt 1998; Mo et al. 1998), and $\alpha_{\text{SF}} = 0.03$ controls the efficiency of the transformation of cold gas into stars. Massive stars explode as supernovae shortly after star formation events and are assumed to reheat a gas mass proportional to the mass of stars:

$$\Delta m_{\text{reheated}} = \epsilon_{\text{disk}} \Delta m_*, \quad (2.6)$$

where we set the free parameter $\epsilon_{\text{disk}} = 3.5$ based on the observational data. The energy released by an event which forms a mass Δm_* in stars is assumed to be:

$$\Delta E_{\text{SN}} = 0.5 \epsilon_{\text{halo}} \Delta m_* V_{\text{SN}}^2, \quad (2.7)$$

where $0.5 V_{\text{SN}}^2$ is the mean supernova energy injected per unit mass of newly formed stars, and ϵ_{halo} represents the efficiency with which this energy is able to convert cold interstellar medium into hot, diffuse halo gas. The amount of gas that leaves the DM halo in a ‘‘super-wind’’ is determined by computing whether excess SN energy is available to drive the flow after reheating of material to the halo virial temperature.

We model the disk instabilities using the analytic stability criterion of Mo et al. (1998); the stellar disk of a galaxy becomes unstable when the following inequality is met:

$$\frac{V_c}{(G m_{\text{disk}} / r_{\text{disk}})^{1/2}} \leq 1. \quad (2.8)$$

At each time-step we evaluate the left-hand side of Equation (2.8) for each galaxy, and if it is smaller than unity we transfer enough stellar mass from disk to bulge (at fixed r_{D}) to restore stability.

In the Millennium Run, substructures are followed down to masses of $1.7 \times 10^{10} h^{-1} M_{\odot}$, so that we can properly follow the motion of galaxies inside their hosting DM haloes until tidal truncation and stripping disrupt their subhalos at this resolution limit. At this point, we estimate a survival time for the galaxies using their current orbit and the dynamical friction formula of Binney & Tremaine (1987) multiplied by a factor of 2, as in De Lucia & Blaizot (2007). After this time, the galaxy is assumed to merge onto the central galaxy of its own halo. Galaxy mergers induce starburst which we describe using the ‘‘collisional starburst’’ prescription introduced by Somerville et al. (2001). In this model, a fraction e_{burst} of the combined cold gas from the two merging galaxies is turned into stars as follows:

$$e_{\text{burst}} = \beta_{\text{burst}} (m_{\text{sat}} / m_{\text{central}})^{\alpha_{\text{burst}}}, \quad (2.9)$$

where the two parameters are taken as $\alpha_{\text{burst}} = 0.7$ and $\beta_{\text{burst}} = 0.56$, appropriate for merger mass ratios ranging from 1:10 to 1:1 (Cox 2004).

2.2.3 BH mass accretion and AGN

The ‘radio mode’

When a static hot halo has formed around a galaxy, we assume that a fraction of the hot gas continuously accretes onto the central BH, causing a low-energy ‘radio’ activity in the galaxy centre. Following Croton et al. (2006), the BH mass accretion rate during these phases is postulated to scale

as follows:

$$\dot{M}_{\text{BH,R}} = \kappa_{\text{AGN}} \left(\frac{M_{\text{BH}}}{10^8 M_{\odot}} \right) \left(\frac{f_{\text{hot}}}{0.1} \right) \left(\frac{V_{\text{vir}}}{200 \text{ km s}^{-1}} \right)^3, \quad (2.10)$$

where M_{BH} is the BH mass, f_{hot} is the fraction of the total halo mass in the form of hot gas, and κ_{AGN} is a free parameter set equal to $7.5 \times 10^{-6} M_{\odot} \text{ yr}^{-1}$ in order to reproduce the turnover at the bright end of the galaxy luminosity function. Since f_{hot} is approximately constant for $V_{\text{vir}} \gtrsim 150 \text{ km s}^{-1}$, the dependence of $\dot{m}_{\text{BH,R}}$ on this quantity has a little effect. Note that the accretion rate given by Equation (2.10) is typically orders-of-magnitude below the Eddington limit. In fact, the total mass growth of BHs in the radio relative to the quasar mode discussed below is negligible.

It is also assumed that the *radio mode* feedback injects energy efficiently into the surrounding medium, which can reduce or even stop the cooling flow in the halo centres. The mechanical heating generated by this kind of BH mass accretion and described as $L_{\text{BH}} = \epsilon \dot{M}_{\text{BH}} c^2$, where $\epsilon = 0.1$ is the *accretion efficiency* and c is the speed of light, induces a modified infall rate of the following kind:

$$\dot{m}'_{\text{cool}} = \dot{m}_{\text{cool}} - \frac{L_{\text{BH}}}{0.5 V_{\text{vir}}^2}. \quad (2.11)$$

For consistency we never allow \dot{m}'_{cool} to fall below zero. In this scenario, the effectiveness of radio AGN in suppressing cooling flows is greatest at late times and for large values of the BH mass, which is required to successfully reproduce the luminosities, colours and clustering of low-redshift bright galaxies.

The ‘quasar mode’

In our model BHs accrete mass after a galaxy merger both through coalescence with another BH and by accreting cold gas, the latter being the dominant accretion mechanism. For simplicity, the BH coalescence is modelled as a direct sum of the progenitor masses, thus ignoring gravitational wave losses. Following Kauffmann & Haehnelt (2000), we assume that the gas mass accreted during a merger is proportional to the total cold gas mass present, but with an efficiency which is lower for smaller mass systems and for unequal mergers:

$$\Delta M_{\text{BH,Q}} = \frac{f'_{\text{BH}} m_{\text{cold}}}{1 + (280 \text{ km s}^{-1} / V_{\text{vir}})^2}, \quad (2.12)$$

where

$$f'_{\text{BH}} = f_{\text{BH}} (m_{\text{sat}} / m_{\text{central}}), \quad (2.13)$$

and $f_{\text{BH}} \approx 0.03$ is chosen to reproduce the observed local $M_{\text{BH}} - M_{\text{bulge}}$ relation. Thus, any merger-induced perturbation to the gas disk (which might come from a bar instability or a merger-induced starburst) can in principle drive gas onto the central BH. However, the fractional contribution of minor mergers is typically quite small, so that accretion driven by major mergers is the dominant mode of BH growth in our scenario. This kind of accretion, which we call *quasar mode*, is also closely associated with starbursts, which occur concurrently. We do not model feedback from the quasar activity in the current model, but it can be approximately represented by an enhanced effective feedback efficiency for the supernovae associated with the intense starburst.

AGN luminosity

The output of the model summarized hitherto, called *DeLucia2006a catalogue* (De Lucia & Blaizot 2007), is publicly available at <http://www.mpa-garching.mpg.de/millennium> (Lemson & Virgo Consortium 2006). In this default model, for simplicity, the BH mass accretion triggered by each merger is implemented as an instantaneous event and the BH seed masses are set equal to zero.

In order to study the evolution of AGN inside this cosmological framework, we improve the original model of De Lucia & Blaizot (2007) by adding new semi-analytical prescriptions to describe the BH mass accretion rate during each merger event in the *quasar mode*, and its conversion into radiation. In this implementation, BHs do not accrete mass instantaneously. Instead, the accretion is coupled to the light curve model adopted. If a galaxy undergoes a merger while the central BH is still accreting mass from a previous merger, the cold gas still to be accreted is added to the new gas reservoir, and the accretion re-starts under the new physical conditions. In Sect. 2.3.1 we show that the BH scaling relations are weakly affected by this change. We use the following definitions to parameterize the bolometric luminosity emitted by accretion onto BHs, as a function of the *accretion efficiency*, ϵ , and the *Eddington factor*, $f_{\text{Edd}}(t) := L_{\text{bol}}(t)/L_{\text{Edd}}(t)$,

$$\begin{aligned} L_{\text{bol}}(t) &= \frac{\epsilon}{1-\epsilon} \dot{M}_{\text{BH}}(t) c^2 \\ &= f_{\text{Edd}}(t) L_{\text{Edd}}(t) = f_{\text{Edd}}(t) \frac{M_{\text{BH}}(t)}{t_{\text{Edd}}} c^2, \\ \implies d \ln M_{\text{BH}}(t) &= \frac{dt}{t_{\text{ef}}(t)}, \end{aligned} \quad (2.14)$$

where L_{Edd} is the Eddington luminosity, $t_{\text{Edd}} = \sigma_T c / (4\pi m_p G) \sim 0.45 \text{ Gyr}$ and $t_{\text{ef}}(t) = \frac{\epsilon}{1-\epsilon} \frac{t_{\text{Edd}}}{f_{\text{Edd}}(t)}$ is the e-folding time ($t_{\text{ef}} \equiv t_{\text{Salpeter}}$ if $f_{\text{Edd}} = 1$).

No strong observational constraints are available for ϵ and f_{Edd} , the parameters that regulate the BHs powering the AGN and, more importantly, if and how they depend on redshift, BH masses, AGN luminosities and so on. However, some observations at $z \sim 0$ indicate that $0.04 < \epsilon < 0.16$ and $0.1 < f_{\text{Edd}} < 1.7$ (Marconi et al. 2004). Furthermore, it has been suggested that f_{Edd} may depend on redshift (Shankar et al. 2004) and BH mass (Netzer & Trakhtenbrot 2007). In this modeling, for simplicity, we do not follow the evolution of the BH spins (see, e.g. Volonteri et al. 2007, and references therein) and we take a constant mean value for the accretion efficiency of $\epsilon = \langle \epsilon \rangle = 0.1$ at all redshifts.

For f_{Edd} , which determines the light curves associated with individual quasar events, we consider instead three different prescriptions:

- *I*: $f_{\text{Edd}} = 1$, the simplest possible assumption. Here the quasar is either ‘on’ at its maximum Eddington luminosity, or ‘off’.
- *II*:

$$f_{\text{Edd}}(z) = \begin{cases} f_{\text{Edd},0} & z \geq 3 \\ f_{\text{Edd},0} \cdot [(1+z)/4]^{1.4} & z < 3 \end{cases} \quad (2.15)$$

with $f_{\text{Edd},0} = 0.3$, as suggested by Shankar et al. (2004) to match the BH mass function derived from a deconvolution of the AGN luminosity function and the local BH mass function.

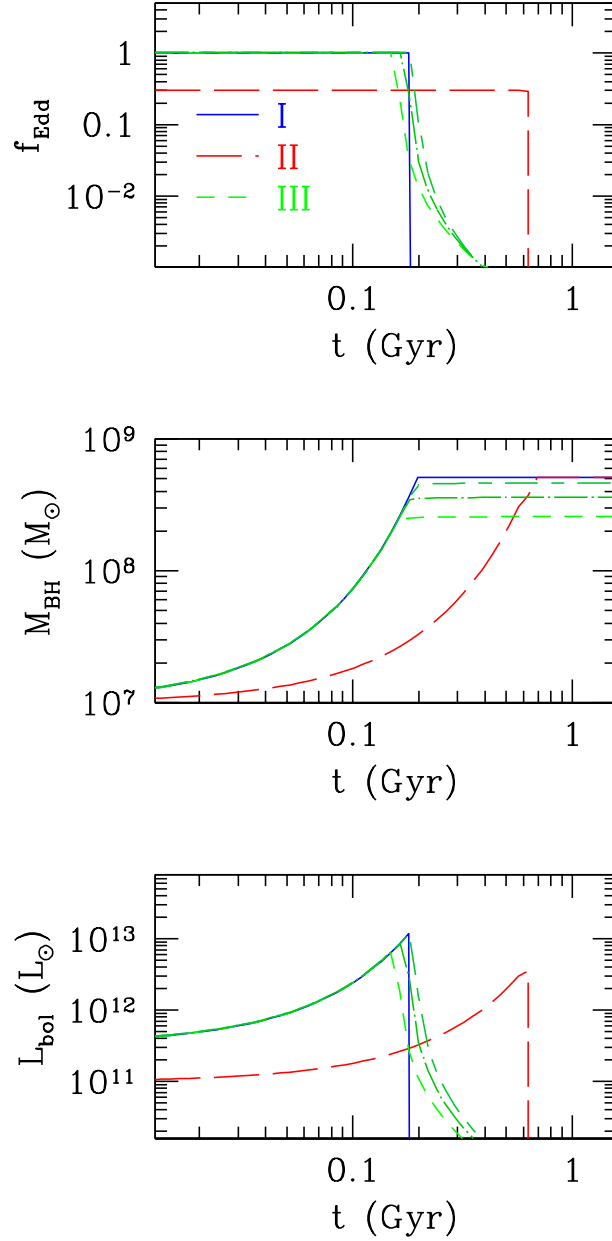


Figure 2.1: The time evolution of f_{Edd} (top panel), M_{BH} (central panel) and L_{bol} (bottom panel) for our three light curve models (I (blue solid lines), II (red short-dashed lines) and III (green lines)), for an illustrative case of a BH of mass $M_{\text{BH}} = 10^7 M_{\odot}$ accreting a mass $\Delta M_{\text{BH,Q}} = 5 \times 10^8 M_{\odot}$, starting at $z = 3$. The three green curves, showing our model III, have been obtained by setting $\mathcal{F} = 0.5$ (short dashed), 0.7 (dotted-long dashed) and 0.9 (short dashed-long dashed).

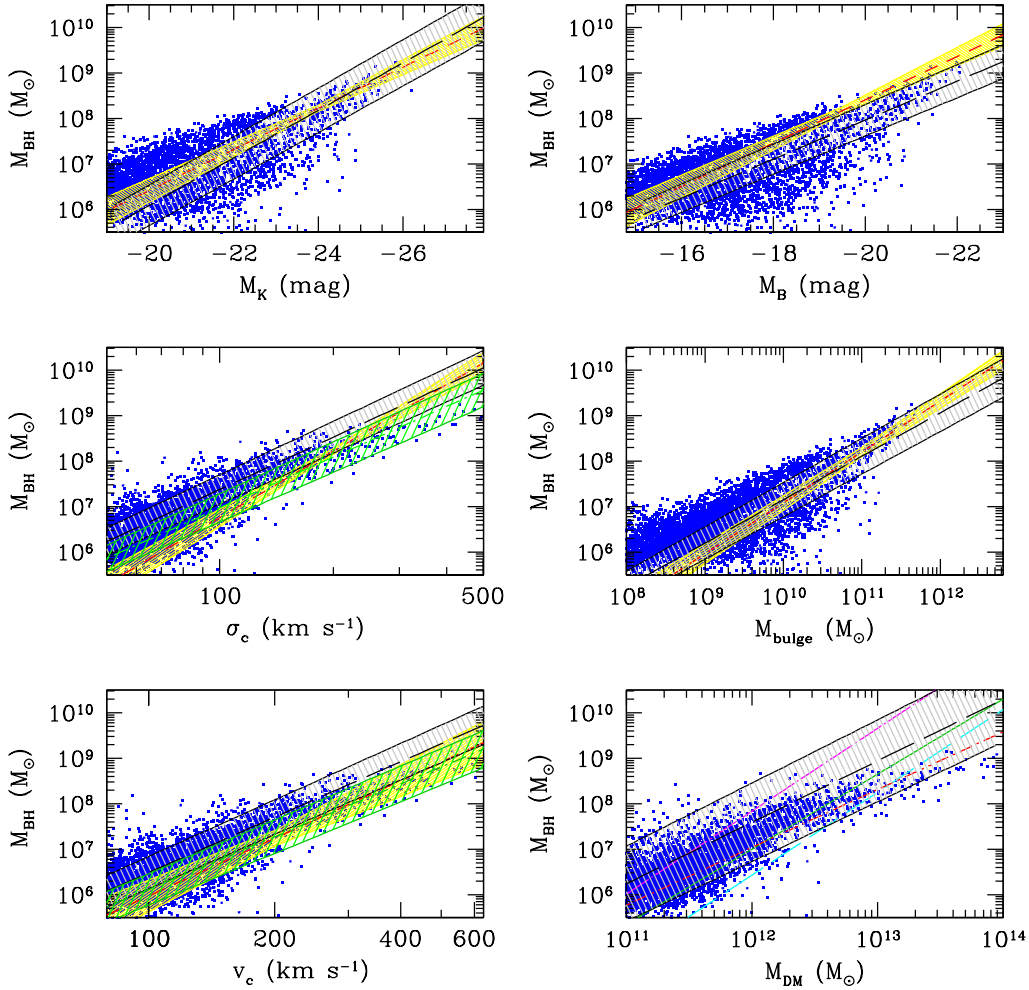


Figure 2.2: Starting from the upper left panel down to the bottom right one, scaling relations between the masses of the central BHs in the simulated galaxies with six different properties of their hosts: the K - and B -band bulge magnitude (top left and right panels, respectively), the bulge velocity dispersion and mass (central left and right panels, respectively), the circular velocity of the galaxy (bottom left panel) and the virial mass of the DM halo (bottom right panel). Blue dots represent the outputs of the DeLucia2006a catalogue, grey and yellow shaded areas show the best fit to the model predictions and to the observational datasets, respectively. Starting from the upper left panel down to the lower right, the yellow shaded areas refer to the best-fit relations obtained by Marconi et al. (2004) (the upper two panels of the plot), Ferrarese & Ford (2005), Häring & Rix (2004), Baes et al. (2003) and, in the lower-right panel, the four curves show the equations 4 (cyan), 6 (green) and 7 (magenta) of Ferrarese (2002) and the results of Baes et al. (2003) (red).

Relation	Normalization (α)	Slope (β)	Scatter	Scatter _{corrected}
$\log(M_{\text{BH}}) - M_{\text{K}}$	-4.37(0.24)	-0.52(0.01)	0.68	0.53
$\log(M_{\text{BH}}) - M_{\text{B}}$	-0.61(0.17)	-0.43(0.01)	0.62	0.53
$\log(M_{\text{BH}}) - \log(\sigma_{\text{c}})$	-0.26(0.16)	3.82(0.08)	0.42	0.28
$\log(M_{\text{BH}}) - \log(M_{\text{bulge}})$	-2.39(0.19)	0.96(0.02)	0.58	0.50
$\log(M_{\text{BH}}) - \log(V_{\text{c}})$	-1.61(0.18)	4.05(0.09)	0.45	
$\log(M_{\text{BH}}) - \log(M_{\text{DM}})$	-8.61(0.42)	1.35(0.04)	0.50	

Table 2.1: Parameters of the linear fits to the scaling relations shown in Figure 2.2. A correlation of the form $y = \alpha + \beta \cdot x$ has been assumed for all relations. The uncertainties in the normalizations and in the slopes are shown in parentheses. For details about the computation of the Scatter and the Scatter_{corrected} see Sect. 2.3.1.

Relation	α	β	γ	Scatter
$\log(M_{\text{BH}}) - M_{\text{K}}$	17.29(0.10)	1.25(0.01)	0.04(0.01)	0.51
$\log(M_{\text{BH}}) - M_{\text{B}}$	9.81(0.03)	0.63(0.01)	0.03(0.01)	0.47
$\log(M_{\text{BH}}) - \log(M_{\text{bulge}})$	14.16(0.07)	-2.21(0.01)	0.15(0.01)	0.44

Table 2.2: Parameters of the fits to the scaling relations shown in Figure 2.3. A correlation of the form $y = \alpha + \beta \cdot x + \gamma \cdot x^2$ has been assumed for all three relations. The uncertainties in the parameters are shown in parentheses. For details about the computation of the Scatter see Sect. 2.3.1.

- *III*: based on the analysis of self-consistent hydrodynamical simulations of galaxy mergers, Hopkins et al. (2005) noticed that the light curves of active BHs are complex, showing periods of rapid accretion after “first passage” of the merging galaxies, followed by a long-lasting quiescent phase, then a transition to a highly luminous, peaked quasar phase, finally a fading away when quasar feedback expels gas from the remnant’s centre in a self-regulated mechanism after the BH reaches a critical mass. In spite of this complexity, as a first order approximation, the typical evolution of an active BH can be simply described as a two-stage process of a rapid, Eddington-limited growth up to a peak BH mass, preceeded and followed by a much longer quiescent phase with lower Eddington ratios. In this latter phase, the average time spent by AGN per logarithmic luminosity interval can be approximated as (Hopkins et al. 2005)

$$\frac{dt}{d \ln L_{\text{bol}}} = |\alpha| t_9 \left(\frac{L_{\text{bol}}(t)}{10^9 L_{\odot}} \right)^{\alpha}, \quad (2.16)$$

where $t_9 \equiv t_Q(L' > 10^9 L_{\odot})$ and $t_Q(L' > L)$ is the total AGN lifetime above a given luminosity L ; $t_9 \sim 10^9$ yr over the range $10^9 L_{\odot} < L_{\text{bol}} < L_{\text{peak}}$. In the range $10^{10} L_{\odot} \lesssim L_{\text{peak}} \lesssim 10^{14} L_{\odot}$, Hopkins et al. (2005) found that α is a function of only the AGN luminosity at the peak of its activity, L_{peak} , given by $\alpha = -0.95 + 0.32 \log(L_{\text{peak}}/10^{12} L_{\odot})$, with $\alpha = -0.2$ (the approximate slope of the Eddington-limited case) as an upper limit. We here interpret the Hopkins model as describing primarily the decline phase of the quasar activity, after the black hole has grown at the Eddington rate to a peak mass $M_{\text{BH,peak}} = M_{\text{BH}}(t_{\text{in}}) + \mathcal{F} \cdot \Delta M_{\text{BH,Q}} \cdot (1 - \epsilon)$, where $M_{\text{BH}}(t_{\text{in}})$ is the initial BH mass and $\Delta M_{\text{BH,Q}}$ is the fraction of cold gas mass accreted. Here \mathcal{F} is an additional free parameter, in the range $0 \leq \mathcal{F} \leq 1$. For $\mathcal{F} = 1$ the BH emits at the Eddington

rate. In the opposite limit ($\mathcal{F} = 0$) the AGN reaches instantaneously a peak luminosity, and the whole light curve is described by equation (2.16). We found that $\mathcal{F} = 0.7$ is the value that best matches the AGN luminosity function. We note that this interpretation of the Hopkins model is plausible but not unique, as part of the time described by equation (2.16) could also be associated with the rising part of the light curve.

From equation (2.16) and with the following definition

$$\tilde{f}_{\text{Edd}}(t) := \frac{L_{\text{bol}}(t)}{L_{\text{peak}}} = f_{\text{Edd}}(t) \frac{L_{\text{Edd}}(t)}{L_{\text{peak}}}, \quad (2.17)$$

we can derive:

$$\frac{d\tilde{f}_{\text{Edd}}(t)}{dt} = -\frac{\tilde{f}_{\text{Edd}}^{1-\alpha}(t)}{\alpha t_9} \left(\frac{L_{\text{peak}}}{10^9 L_{\odot}} \right)^{-\alpha}, \quad (2.18)$$

$$\Rightarrow \tilde{f}_{\text{Edd}}(t) = \left[\tilde{f}_{\text{Edd},0}^{\alpha} + \left(\frac{L_{\text{peak}}}{10^9 L_{\odot}} \right)^{-\alpha} \frac{t}{t_9} \right]^{1/\alpha}. \quad (2.19)$$

Here we neglected the absolute value of α present in equation (2.16), for the purpose of having $\tilde{f}_{\text{Edd}}(t)$ a decreasing function of time. Finally, from equations (2.14), (2.17) and (2.19), we have:

$$M_{\text{BH}}(t) = M_{\text{BH,peak}} + \frac{A}{BC} \left[(1 + Ct)^B - 1 \right], \quad (2.20)$$

where $A = \frac{1-\epsilon}{\epsilon} \frac{M_{\text{BH,peak}}}{f_{\text{Edd}}}$, $B = \frac{1}{\alpha} + 1$, $C = \left(\frac{L_{\text{peak}}}{10^9 L_{\odot}} \right)^{-\alpha} \frac{1}{t_9}$. To derive equation (2.20) we set $\tilde{f}_{\text{Edd},0} = 1$ for continuity. We also impose $f_{\text{Edd}} = 10^{-3}$ as lower limit for the Eddington factor.

Figure 2.1 shows the evolution of $f_{\text{Edd}}(t)$ (top panel), $M_{\text{BH}}(t)$ (central panel) and $L_{\text{bol}}(t)$ (bottom panel) for an illustrative case of a BH of $M_{\text{BH}} = 10^7 M_{\odot}$ accreting a mass $M_{\text{accr}} = 5 \times 10^8 M_{\odot}$, starting at $z = 3$, in the three prescriptions considered. The three green curves refer to light curve model III, in which we set $\mathcal{F} = 0.5$ (short dashed), $= 0.7$ (dot-long dashed) and $= 0.9$ (short dashed-long dashed).

Due to the present uncertainties concerning the origin of the BH seeds and their mass distribution, we assume $M_{\text{BH,seed}} = 10^3 M_{\odot}$ for all seed BHs, irrespective of their halo host properties and their origin. Our results are robust with respect to this hypothesis since, as we have verified, they are basically unaffected by varying $M_{\text{BH,seed}}$ in the range $[10^2 - 10^5] M_{\odot}$ at $z \lesssim 3$. More significant differences occur at higher redshifts, which we will investigate in detail in future work.

The main parameters of our model are listed in Table 1 of Croton et al. (2006), with the exception of, as in De Lucia & Blaizot (2007), the values for the quiescent hot gas BH accretion rate, κ_{AGN} (defined in Equation (2.10)), the star formation efficiency α_{SF} of equation (2.5), and the instantaneous recycled fraction of star formation to the cold disk, R , which we set equal to 0.43 (see Section 3.9 of Croton et al. 2006).

2.3 Models vs. Observations

2.3.1 The BH scaling relations

Several observational evidences indicate that the masses of the BHs hosted at the centres of galaxies strongly correlate with different properties of their host bulges and DM haloes. In this section we

compare the most recently observed BH scaling relations at $z = 0$ with the predictions of the original model of De Lucia & Blaizot (2007), i.e. the predictions we obtain when assuming instantaneous mass accretion. We explore the effect of specifying the mass accretion rate at the end of this section.

One-parameter relations

In Figure 2.2, we show the correlation between the masses of the model BHs with six properties of their hosts, the K- and B-band bulge magnitude (M_B and M_K), the bulge mass and velocity dispersion (M_{bulge} and σ_c), the circular velocity of the galaxy and the virial mass of the DM halo (V_c and M_{DM}). The blue dots represent the outputs of the model, while grey and yellow shaded areas show linear best fits to the model predictions and to the observational datasets, respectively.

The dots in the plot refer to the population of BHs hosted in the central galaxies of FOF groups, or subhalos. We do not include those in satellite galaxies since in this case the host properties cannot be determined accurately. The data we have considered are: the $M_{\text{BH}} - M_B$ and $M_{\text{BH}} - M_K$ relations of Marconi et al. (2004) (top panels) the $M_{\text{BH}} - \sigma_c$ relation of Ferrarese & Ford (2005) (central left) the $M_{\text{BH}} - M_{\text{bulge}}$ relation of Häring & Rix (2004) (central right) and the $M_{\text{BH}} - V_c$ relation of Baes et al. (2003) (bottom left). No direct observational estimate is available for the $M_{\text{BH}} - M_{\text{DM}}$ relation shown in the bottom right panel. The curves shown in this panel have been derived using different assumptions for the $M_{\text{DM}} - V_c$ relation. In particular, the cyan, green and magenta lines correspond to equations (4), (6) and (7) of Ferrarese (2002), while the red curve is taken from Baes et al. (2003).

Model predictions for V_c and σ_c have been obtained by adopting two different assumptions: i) $V_c = V_{\text{max}}$, where V_{max} is the maximum rotational velocity of the subhalo hosting the galaxy at its centre, and ii) $V_c = 1.8 V_{\text{vir}}$ as derived by Seljak (2002). The bulge velocity dispersion σ_c is derived from the $V_c - \sigma_c$ relation of Baes et al. (2003). In the bottom panels, the grey areas correspond to a circular velocity obtained through hypothesis i) while the green ones, in better agreement with the data, assume hypothesis ii).

The linear fit to the model data has been obtained using the bisector modification to the ordinary least squares minimization approach, proposed by Akritas & Bershady (1996), for which the best-fit results correspond to the bisection of those obtained from minimizations in the vertical and horizontal directions. The estimator is robust and has the advantage of taking into account the possible intrinsic scatter in the relation. The values of the best fit slope and the normalization are listed in Table 2.1 along with the scatter around the best fitting line. The uncertainties of the best fit parameters, also reported in the table, have been obtained by imposing $\chi^2_{\text{d.o.f.}} = 1$.

As can be seen in Figure 2.2, the best fits to the model agree well with that to the data, within the scatter. We note that, in all relations plotted, the scatter in the model is larger than that of the real data and also larger than the internal scatter observed in similar relations obtained from the recent hydrodynamical simulations of galaxy mergers (see e.g. Hopkins et al. 2007a). However, we notice that a large fraction of our model BHs are found in low-mass systems for which the scatter in the scaling relation is large. On the contrary, in the real datasets (and hydro-simulations) the majority of BHs belong to massive galaxies for which, according to our model, the scatter in the scaling relation is significantly smaller. To investigate whether the difference in the intrinsic scatter is real or is induced by a different sampling of the BH population, for each BH scaling relation we have discretized the range of the observed host galaxy properties in finite bins and generated 500 sub-samples by randomly extracting $N_{\text{obs}}(\Delta_X)$ model BHs from the parent catalogue, where $N_{\text{obs}}(\Delta_X)$ is the number of BHs in the real dataset in each bin Δ_X . We have repeated the same fitting procedure in

the 500 sub-samples and found that the scatter is significantly reduced in this exercise, as indicated in the last column of Table 2.1, that lists the average scatter in the sub-catalogues. Therefore, the mismatch in the scatter results from sampling different BH populations: small objects in the model, massive objects in the observations. Moreover, for the $M_{\text{BH}} - \sigma_c$ relation the scatter is very close to 0.21, which is the value measured by Hopkins et al. (2007a) both in the observed and simulated data.

Non-linear fits

The agreement between model and data is satisfactory. However, we need to keep in mind that the model predictions for V_c and σ_c and the observed relation between $\log(M_{\text{BH}})$ and $\log(M_{\text{DM}})$ have been obtained assuming further theoretical hypotheses. Consequently, the more constraining and reliable relations are the ones between the BH masses and the bulge magnitudes and masses. Focusing on these relations and thanks to the huge number of model BHs, we have been able to investigate whether a non-linear fit provides a better match to the data. We find that the best fit is a quadratic function, $y = \alpha + \beta \cdot x + \gamma \cdot x^2$. Figure 2.3 shows this fit (heavy green lines), together with the medians, the first and third quartiles (black points with error bars) of the model output, computed in a discrete number of bins. The internal scatter is significantly smaller than in the linear fit case. The values of the best fit parameters are reported in Table 2.2. While we predict, on average, too low BH masses for a fixed M_{B} with respect to the observations (still consistent within the errors) the model predictions are in very good agreement with the data for the $\log(M_{\text{BH}}) - M_{\text{K}}$ and $\log(M_{\text{BH}}) - \log(M_{\text{bulge}})$ relations. Interestingly, the 3-parameters fit of the latter relation is in excellent agreement with the one found by Wyithe (2006) (magenta solid line in lower panel of Figure 2.3).

The fundamental plane relation

In Figure 2.4 we compare the BH fundamental plane relation of our model at different redshifts with that obtained by Hopkins et al. (2007a) using both observational data and the outputs of hydrodynamical simulations of galaxy mergers:

$$\log(M_{\text{BH}}/M_{\odot}) = 7.93 + 0.72 \log(M_{11}^*) + 1.4 \log(\sigma_{200}),$$

where M_{11}^* is the galaxy stellar mass in units of $10^{11} M_{\odot}$, and σ_{200} is the bulge velocity dispersion in units of 200 km s^{-1} . The red lines, bisectors of the plots, show the fundamental plane relation proposed by Hopkins et al. (2007a). Model prediction are represented by blue dots, the black line is the best fit to the model and the shaded area its 1σ scatter. At low redshifts the agreement is very good. This is not surprising since at $z \sim 0$ our model agrees with the $M_{\text{BH}} - M_{\text{bulge}}$ and $M_{\text{BH}} - \sigma_c$ scaling relations that represent fundamental plane projections. A discrepancy appears at high redshifts. However, at $z > 3$ the fit involves only few objects and therefore may not be very significant, especially when we account for the non-zero intrinsic scatter in the fundamental plane proposed by Hopkins et al. (2007a). A remarkable success of our model is that it predicts very little evolution of the fundamental plane relation, at least out to $z = 3$, in agreement with Hopkins et al. (2007a). The intrinsic scatter, which does not evolve with time either, is 3 times larger than in Hopkins et al. (2007a) (we found a value around 0.6 at all redshifts, while the one reported by Hopkins et al. (2007a) is about 0.2). As discussed previously, the mismatch is reduced when using

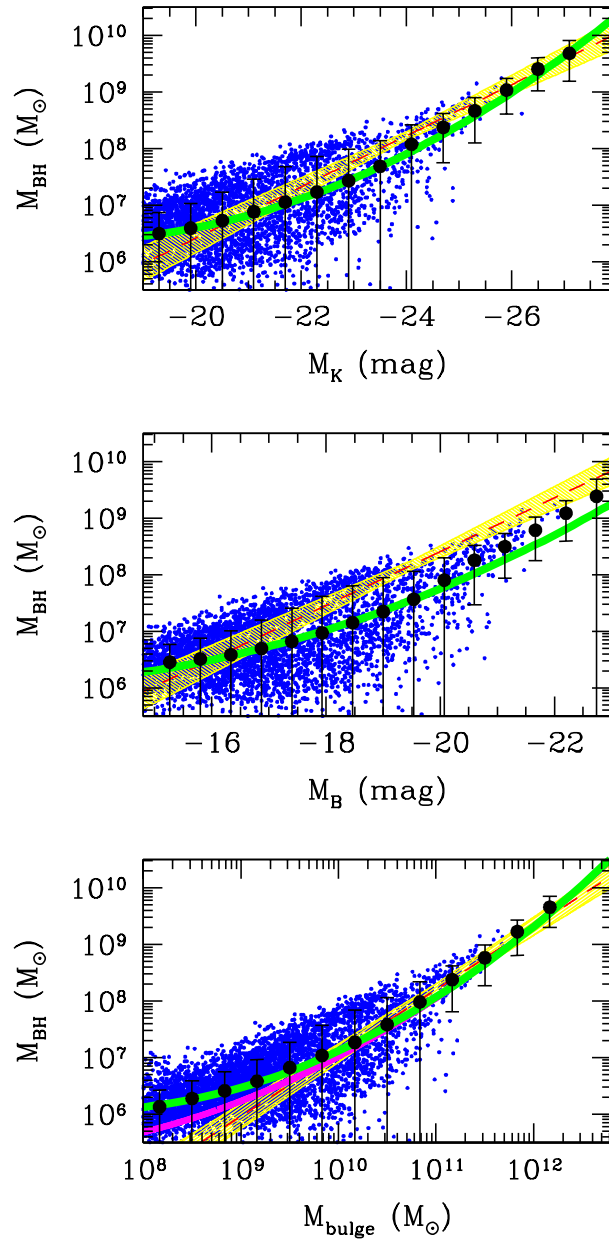


Figure 2.3: *The tree model scaling relations best constrained by observations. Here the black dots (with error bars) represent the medians (and the corresponding first and third quartiles) of the model outputs, computed in a discrete number of bins. The green lines show the best three-parameters fits to the model outputs (blue points). The magenta line in the lower panel refers to the best-fit relation obtained by Wyithe (2006).*

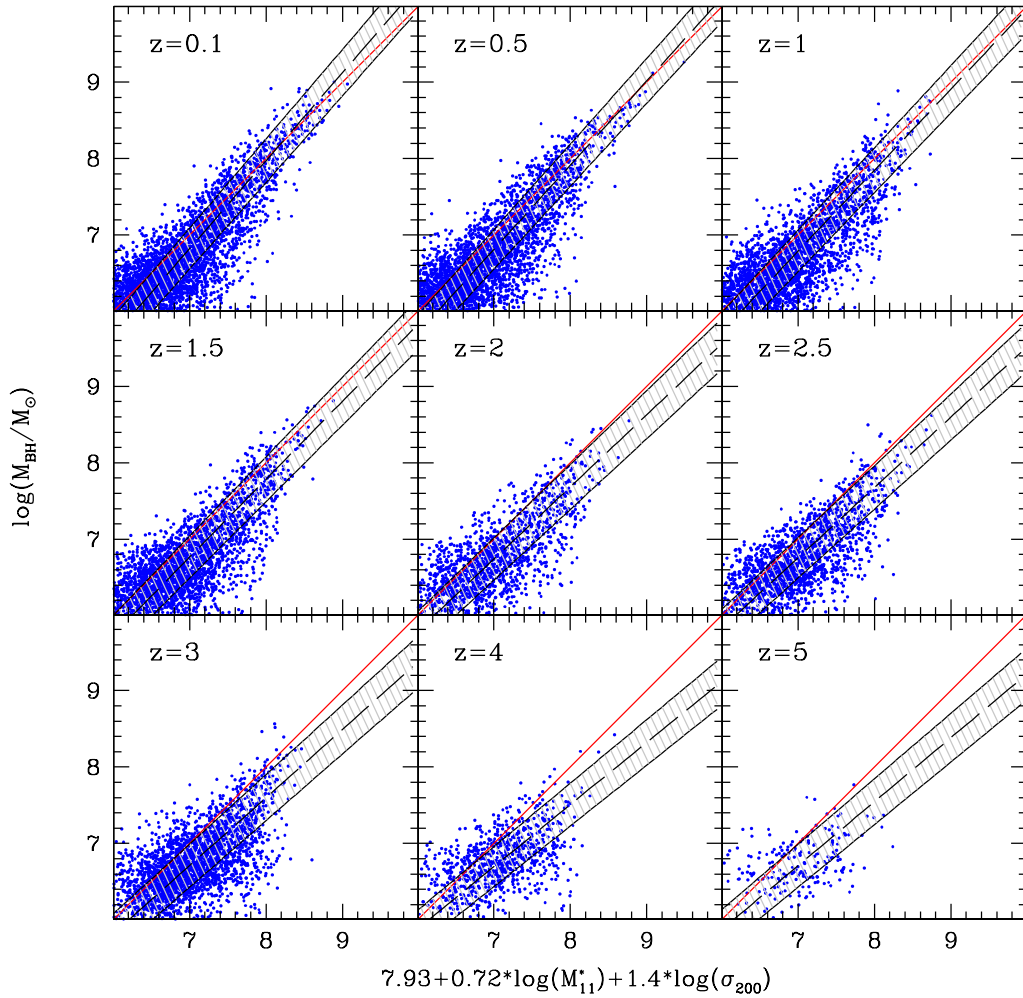


Figure 2.4: The BH fundamental plane in the redshift range $0.1 \leq z \leq 5$. The blue dots are the model outputs, while the grey shaded areas show the best-fits to them. The red lines, corresponding to the bisectors of the plots, are the predictions of Hopkins et al. (2007a). The galaxy stellar mass, M_{11}^* , is given in units of $10^{11} M_{\odot}$, while the bulge velocity dispersion, σ_{200} , is in units of 200 km s^{-1} .

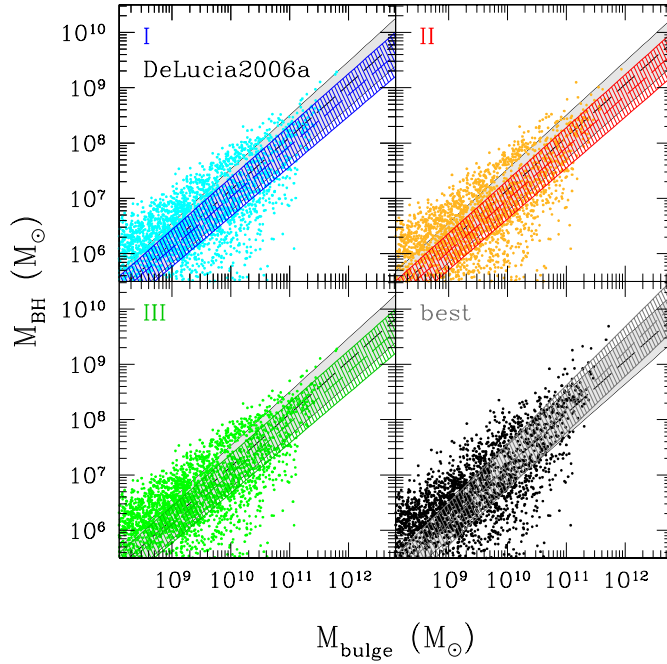


Figure 2.5: The $\log(M_{\text{BH}}) - \log(M_{\text{bulge}})$ scaling relation for our different prescriptions for the BH mass accretion. The filled dots represent model predictions, the grey shaded areas show the linear fit to the DeLucia2006a model scaling relation and the other hatched areas indicate the linear fit to the I, II and III light curve models, as indicated by the labels. The black dots and grey shaded areas, in the lower right panel, show the prediction obtained with the parameterization given by the equations (2.21), as explained in §2.3.3.

a number of model BHs consistent with the observed one.

Dependence on the accretion history

All scaling relations predicted by our model assume that BHs accrete mass instantaneously after merging events. What happens if we relax this assumption and specify the mass accretion rate instead? Figure 2.5 shows the impact of adopting different accretion recipes on the $M_{\text{BH}} - M_{\text{bulge}}$ relation. As usual, filled dots represent model predictions, grey shaded areas show the linear fit to the *DeLucia2006a* model scaling relation and the other hatched areas indicate the linear fit to the model predictions obtained with our different recipes, as indicated by the labels. Clearly, these predictions depend little on the assumed mass accretion histories for each individual quasar event (the fit parameters have fluctuations of no more than about 1%). This is a consequence of the fact that the BH scaling relations depend mainly on the total mass accreted, and very little on the time spent in the accretion process. We have verified that all other scaling relations, including also the fundamental plane relation, does not change significantly by adopting any of the mass accretion prescriptions described in §2.2.3.

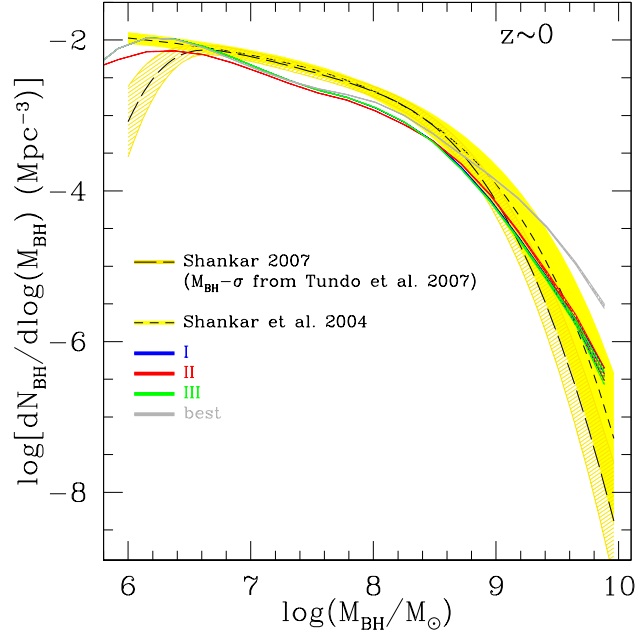


Figure 2.6: Comparison of the BH mass function predicted by light curve models I, II and III with the one observationally derived by Shankar et al. (2004), and with the new one obtained by Shankar (2007, in preparation) using the $M_{\text{BH}} - \sigma$ relation by Tundo et al. (2007). The grey areas show the prediction obtained with the parameterization given by the equations (2.21), as explained in §2.3.3.

2.3.2 The BH mass function

The BH mass function (MF) is defined as the differential co-moving number density of BHs as a function of their mass. In Figure 2.6, we compare the BH MF predicted by our model for the prescriptions I (blue line), II (red) and III (green) with those observed by Shankar et al. (2004) (grey area) and by Shankar (2007, in preparation) (yellow area) at $z \sim 0$. In neither case the BH masses were determined directly: Shankar et al. (2004) derive the BH mass from the observed $M_{\text{BH}} - L_{\text{bulge}}$ relation while Shankar (2007) use the $M_{\text{BH}} - \sigma_c$ relation of Tundo et al. (2007). We note that the model BH MF is in good agreement with the observed ones, within the mass range accessible to observations except in the interval $\sim 10^7 - 10^9 M_{\odot}$, in which the number density of model BHs is smaller than the observed one.

We note that, as shown in Figure 2.6, the model predictions for the BH MF are robust with respect to the prescription adopted for the mass accretion history of the individual quasar episodes.

2.3.3 The AGN bolometric luminosity function

The luminosity function (LF) of AGN, namely the derivative of their co-moving number density with respect to luminosity, represents a unique tool to understand their cosmological evolution. Semi-analytic models predict the total (bolometric) luminosity of a statistically complete AGN catalogue, and to compare model LFs with observations we need to specify a bolometric correction, i.e. how to convert the luminosities observed in a particular band into bolometric ones (Elvis et al. 1994; Marconi et al. 2004; Hopkins et al. 2006a). Another correction is required to account for

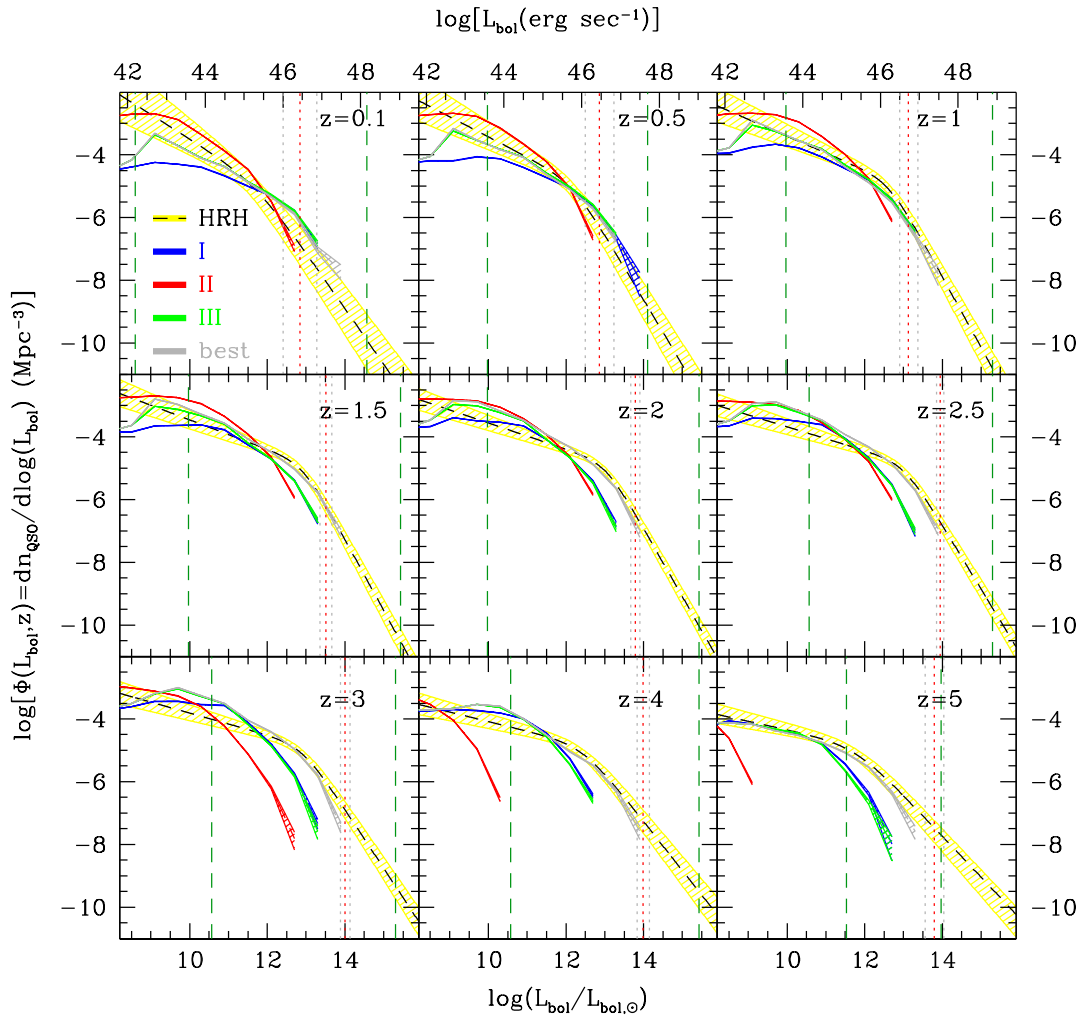


Figure 2.7: The bolometric LFs predicted by our light curve models I (blue bands), II (red bands) and III (green bands), in the redshift range $0.1 \leq z \leq 5$, are here compared with the best-fits to observational data obtained by Hopkins et al. (2007b) (yellow bands). The grey areas show the predictions obtained with the parameterization given by the equations (2.21), as explained in §2.3.3. Uncertainties in the model LFs are computed by assuming Poisson statistics. The dashed vertical green lines mark the range of the bolometric luminosities accessible to observations. The dotted red vertical lines show the luminosities beyond which the LF of Hopkins et al. (2007b) predicts a number of AGN in the whole volume of our simulation smaller than 10. The vertical grey dotted lines around the red ones have been calculated considering the error in the best-fit of Hopkins et al. (2007b).

possible incompleteness effects (see e.g. Comastri 2004; Gilli et al. 2007), which includes the possible existence of a population of obscured AGN whose fraction may depend on the wavelength band and redshift (Elvis et al. 1994; Marconi et al. 2004; La Franca et al. 2005; Lamastra et al. 2006).

Here we compare our predictions with the bolometric LF obtained by Hopkins et al. (2007b) from the LFs observed in different bands: radio (see e.g. Nagar et al. 2005), optical (see e.g. Kennefick et al. 1995; Schmidt et al. 1995; Koehler et al. 1997; Grazian et al. 2000; Fan et al. 2001b; Wolf et al. 2003; Hunt et al. 2004; Cristiani et al. 2004; Croom et al. 2005; Richards et al. 2005, 2006; Siana et al. 2006; Fontanot et al. 2007; Shankar & Mathur 2007; Bongiorno et al. 2007), infra-red (see e.g. Brown et al. 2006; Matute et al. 2006; Babbedge et al. 2006), soft X-ray (see e.g. Miyaji et al. 2000, 2001; Silverman et al. 2005b; Hasinger et al. 2005), hard X-ray (see e.g., Barger et al. 2003b; Ueda et al. 2003; Barger et al. 2003a; Nandra et al. 2005; Sazonov & Revnivtsev 2004; Silverman et al. 2005a; La Franca et al. 2005; Shinozaki et al. 2006; Beckmann et al. 2006), and from emission lines (see e.g. Hao et al. 2005). Uncertainties in these corrections contribute to the scatter in the observed LF, i.e. to the width of the yellow areas in Figure 2.7 that show the AGN bolometric LF of Hopkins et al. (2007b) at different redshifts. The model predictions are also represented by areas with different colours, with a width corresponding to 1σ Poisson error bars. The vertical, green dashed lines bracket the bolometric luminosity range accessible to observations. The vertical, red dotted lines show the luminosities beyond which the LF of Hopkins et al. (2007b) predicts less than 10 AGN in the volume of our simulation, i.e. the maximum luminosities at which our model BH sample is statistically meaningful; 1σ uncertainties on this maximum luminosity are represented by the two grey dotted lines.

From Figure 2.7 we see that, on average, type-*I* light curve underestimates the AGN number density at all epochs. However, while at high redshifts the model matches the faint-end of the LF and underpredicts the number density of the bright objects, the situation is completely reversed at $z \sim 0$, where the model correctly reproduces the number density of bright AGN but underestimates the faint ones. At low redshifts the problem can be alleviated by reducing the Eddington factor, as in our type-*II* light curve. However, in this case the discrepancy between model and data at high redshifts increases. Adopting the type-*III* light curve allows to match observations in the whole range of luminosities in the redshift range $0.5 \lesssim z \lesssim 1$, but overestimates the number of luminous AGN at $z \lesssim 0.5$ and underestimates them at $z \gtrsim 1$.

Therefore, we conclude that in our present semi-analytical framework we can reproduce the observed AGN LF at low and intermediate redshifts. However, at $z \gtrsim 1$, we under-predict the number density of bright AGN, regardless of the BH mass accretion rate and light curve model assumed for each quasar episode. To investigate if it is possible to modify our prescription for the mass accretion to fit the AGN LF at all redshifts, we tried different values of f_{Edd} and ϵ as a function of t and M_{BH} , within physically motivated ranges. Despite of the considerable freedom in choosing $f_{\text{Edd}}(t, M_{\text{BH}})$ we failed to find a model able to match simultaneously the observed BH scaling relations, the BH MF, and the AGN LF, especially at high redshifts. We also used different plausible values for the BH seed mass, and we still were not able to fit the high- z LF. We interpret this failure as an indication that our theoretical framework itself is inadequate to account fully successfully for the AGN phenomenon.

One possible way out is to modify the model assumptions for the efficiency of BH growth in the *quasar mode* following mergers at high z . A significant improvement of our results at high redshifts

can for example be obtained by substituting equation (2.12) and (2.13) with

$$\begin{cases} f_{\text{BH}} = 0.01 \cdot \log\left(\frac{M_{\text{BH}}}{10^3 M_{\odot}} + 1\right) \cdot z & z > 1.5 \text{ and } M_{\text{BH}} > 10^6 M_{\odot} \\ \Delta M_{\text{BH,Q}} = 0.01 \cdot m_{\text{cold}} & z > 6 \end{cases} \quad (2.21)$$

while keeping prescription *III* for the quasar light curves. The predictions of this new model for the $\log(M_{\text{BH}}) - \log(M_{\text{bulge}})$ scaling relation is shown as black dots in the bottom-right plot of Figure 2.5. Model predictions for the BH MF and AGN LF are shown in Figures 2.6 and 2.7, respectively. An accretion efficiency that increases with the redshift has been already advocated in the *dynamical model* of Croton (2006). A physical justification to this assumption is provided by Mo et al. (1998). Indeed, their model predicts that galactic disks were more centrally concentrated in the past, making it more efficient the BH feeding at high redshift. It is worth stressing that equation (2.21) might not provide the best fit to the data as we did not explore the parameter space systematically. However, it suggests that a good match to the observed scaling relations, BH MF and AGN LFs can be obtained within our semi-analytic framework by modest changes of the BH growth at high redshifts. The solution provided by equation (2.21) is not unique either, since larger amounts of mass can be accreted also by invoking alternative mechanisms that trigger gas accretion episodes, for example by secular evolution through disk instabilities, or by alluding to a higher gas cooling efficiency (see e.g. Viola et al. 2007).

2.4 Summary of the chapter

In this chapter we have used and extended a semi-analytic model for the co-evolution of galaxies and their central BHs, developed on the outputs of the Millennium Simulation (Springel et al. 2005c), and described in detail in Croton et al. (2006) and De Lucia & Blaizot (2007). The aim of the model is to reproduce the observed properties of BHs, AGN and their galaxy hosts. The physical assumptions in the model with respect to BH growth can be divided into two sets. The first one concerns the mass accretion history of the central BHs in halos, where we distinguish between *radio mode* and *quasar mode* (Croton et al. 2006). This set makes predictions for the relation between BH and galaxy host properties, which can be compared to the observed scaling relations between BH mass and different properties of their host galaxies. The second set of prescriptions specifies the detailed AGN activity and light curve of individual quasar episodes, and leads to predictions for the AGN LF as a function of redshift. We considered three different models for this detailed AGN activity, one of them motivated by the results of recent hydrodynamical simulations of galaxy mergers that include BH growth and feedback (Hopkins et al. 2005; Di Matteo et al. 2005; Springel et al. 2005b).

The main results of our analysis are as follows:

(i) The semi-analytic model is approximately able to reproduce the observed BH scaling relations over the whole range of BH masses and galaxy properties probed by observations. The intrinsic scatter in the model is significantly larger than in the data, a mismatch that can in part be accounted for by adopting the observational selection criteria to obtain a mock BH catalogue with similar characteristics as the observed one.

(ii) We find evidence that a quadratic relationship provides a significantly better fit to some of the model scaling relationships than a linear one, as already noticed by Wyithe (2006).

(iii) Our model also matches the BH fundamental plane relation derived by Hopkins et al.

(2007a), and successfully predicts very little evolution of this plane, at least out to $z \sim 3$.

(iv) The model BH mass function is in good agreement with the observed one within the mass range accessible by observations, except on the range $\sim 10^7 - 10^9 M_\odot$, in which the number density predicted by the model is smaller than the observed one.

(v) Model predictions for the BH mass function, scaling relations and fundamental plane relation are basically unaffected when using different prescriptions for the AGN light curves of individual quasar events. This is because these predictions are only sensitive to the model assumptions for the absolute growth of the BHs in each merger event.

(vi) The AGN LF is systematically underestimated by assuming that BHs accrete mass with a constant Eddington factor $f_{\text{Edd}} = 1$. The detail of the discrepancy, however, change with redshift since at high z the model matches the faint-end of the LF but underpredicts the number density of the brightest objects, while the situation is reversed at $z \sim 0$, in agreement with the results of several semi-analytic models (see, e.g. Marulli et al. 2007, and references therein). Reducing the Eddington ratio, as in our light curve model *II*, alleviates the faint-end mismatch but amplifies the bright-end discrepancy at high redshifts. A significant improvement at low redshifts is obtained when the Eddington-limited growth of the BH is followed by a long quiescent phase with lower Eddington ratios, as suggested by Hopkins et al. (2005) and implemented in our light curve model *III*. In this case our model is able to match the observed AGN LF in the interval $0.1 \lesssim z \lesssim 1$, over the whole range of luminosities that are accessible to observations and where our predictions are statistically significant. However, our predicted number density of bright AGN is still biased low at $z \gtrsim 1$.

(vii) Our model is able to account for all observations considered in this work apart for the AGN LF at high redshifts. We were not able to eliminate this mismatch by simply modifying the accretion efficiency, ϵ , the Eddington factor, f_{Edd} , or the BH seed mass (when considered in physically plausible ranges). Clearly, we need to modify assumptions in the underlying semi-analytic framework for BH growth. A simple, *ad hoc* increase of the mass fraction accreted during the *quasar mode* at high redshift can indeed remedy the problem. However, this solution is not unique as several high-redshift modifications to the original model, like new mechanisms that trigger BH activity in addition to galaxy merging or more efficient gas cooling resulting in a larger reservoir of cold gas, can be advocated to bring the predictions in line with observations. However, it remains to be seen whether any of these alternatives is physically plausible.

(viii) Our model predictions at $z < 3$ are robust to changes in the assumed BH seed mass, but are sensitive to it at larger redshift.

From our analysis we conclude that the AGN LF at high redshifts constitutes a strong constraint for semi-analytic models that describe the co-evolution of galaxies, BHs and AGN. This suggests that significant improvements can be obtained in two ways. From the theoretical side, we need to develop a physically motivated mechanism capable of increasing the number density of bright AGN at $z \gtrsim 1$ without modifying the model predictions at low redshifts. From the observational point of view, we need to improve the AGN LF estimates at high redshift, both by enlarging current high- z AGN samples and by reducing the current uncertainties originating from bolometric and incompleteness corrections, in particular for the population of Compton Thick AGN.

Chapter 3

The large-scale clustering of simulated quasars

In this chapter¹ we analyze the properties of the large-scale clustering of our quasars simulated using the procedure described in the previous chapter.

We show that, at all luminosities, the quasar two-point correlation function is fit well by a single power-law in the range $0.5 \lesssim r \lesssim 20 h^{-1}\text{Mpc}$, but its normalization is a strong function of redshift. When we select only quasars with luminosities within the range typically accessible by today's quasar surveys, their clustering strength depends only weakly on luminosity, in agreement with observations. This holds independently of the assumed light curve model, since bright quasars are black holes accreting close to the Eddington limit, and are hosted by dark matter haloes with a narrow mass range of a few $10^{12}h^{-1}M_{\odot}$. Therefore the clustering of bright quasars cannot be used to disentangle light curve models, but such a discrimination would become possible if the observational samples can be pushed to significantly fainter limits.

We start with a detailed introduction to the topic of this chapter in §3.1. Then, in §3.2, we describe the specific assumptions for the black hole evolution used to generate the quasar population on which we base the subsequent analysis. In §3.3 the general properties of the clustering of the quasar population are described and compared with the most recent observational optical data. We show the relation between luminous BHs, quiet BHs and their host haloes in §3.4 and finally, in §3.5, the main results of this chapter are summarized and discussed

3.1 Introduction

As firstly suggested by Soltan (1982), it seems that most of the mass in today's BHs must have been accumulated during phases of bright AGN activity. The duration of these highly-efficient accretion phases could range from a few 10^7yr (Yu & Tremaine 2002) up to 10^8yr (Marconi et al. 2004), values that strongly depend on the BH mass range considered and on the assumed radiation efficiency ϵ . In fact, the precise value of this quasar lifetime is still an open question (Martini 2004). Estimates of the duration of individual accretion events using, for example, the *proximity*

¹This chapter follows the paper *Modeling the cosmological co-evolution of supermassive black holes and galaxies II.: the clustering of quasars and their dark environment.* by Silvia Bonoli, Federico Marulli, Volker Springel, Simon D.M. White, Enzo Branchini, Lauro Moscardini (MNRAS, 396, 423).

effect (Carswell et al. 1982; Bajtlik et al. 1988), have suggested lifetimes of the order of 1 Myr (Kirkman & Tytler 2008).

Haiman & Hui (2001) and Martini & Weinberg (2001a) suggested to use quasar clustering to obtain estimates of the quasar lifetime (see also the seminal work of Cole & Kaiser 1989). The reasoning behind this conjecture is simple: if quasars are strongly clustered, their hosts must be rare objects, and therefore they must also be long events in order to account for the total quasar luminosity density observed. If, on the other hand, their clustering is comparable to the clustering of small dark matter haloes, their hosts must be much more common, and their luminous phases must therefore have short duration.

The advent of wide-field surveys like SDSS and 2dFQSO (York et al. 2000; Croom et al. 2004) with their observation of thousands of quasars has allowed a detailed investigation of the clustering properties of accreting BHs. Croom et al. (2005) and Porciani et al. (2004) calculated the correlation function of quasars observed in 2dF in the redshift range $0.5 \lesssim z \lesssim 2$. Both groups found that the clustering strength is an increasing function of redshift, but that it does not depend significantly on quasar luminosity. The inferred values of the bias would suggest that quasars of the observed luminosities are hosted by haloes of a few $10^{12}h^{-1}M_{\odot}$, which remains approximately constant with redshift, since haloes of a fixed mass are progressively more clustered towards higher redshift (see also Grazian et al. 2004). Following the approach of Haiman & Hui (2001) and Martini & Weinberg (2001a), the estimated quasar lifetime would be a few 10^7 yr, reaching $\sim 10^8$ yr at the highest observed redshifts. More recent studies on larger samples and at different redshifts have confirmed these results (Shen et al. 2007; Myers et al. 2007a; Coil et al. 2007; da Ângela et al. 2008; Padmanabhan et al. 2008; Ross et al. 2008). However, the magnitude range covered by these surveys is typically quite narrow, and this may explain the lack of evidence for a significant dependence of clustering on luminosity. When Shen et al. (2009b) analyze the clustering of the 10% brightest objects of their sample, they find that these quasars have a higher bias compared to the full sample.

Using hydrodynamical simulations of isolated galaxy mergers (Springel et al. 2005b; Di Matteo et al. 2005), Hopkins et al. (2005) studied the luminosity distribution of accreting BHs, whose activity is triggered by the merger event. Hopkins et al. (2005) found that the luminosity distribution of the simulated AGN is equivalent to a highly efficient accretion phase (with very high Eddington ratios), followed by a decaying phase where AGN spend most of their life. During this extended period, they would appear as faint AGN, even though they may, in fact, contain quite massive BHs.

Based on these results, Lidz et al. (2006) explored the dependence of quasar clustering on luminosity, using an analytic approach to connect quasars, black hole masses and halo masses. In a quasar model in which the bright end of the luminosity function is populated by BHs accreting close to their peak luminosity, and the faint end is mainly populated by BHs accreting at low Eddington ratio, there should be no strong dependence of clustering on quasar luminosity, i.e., bright and faint AGN should actually be the same type of objects, but seen in different stages of their evolution. They should therefore be hosted by dark matter haloes of similar masses and hence exhibit similar clustering properties. Assuming a relation between the quasar B-band peak luminosity and the mass of the host haloes, Lidz et al. (2006) tested this prediction, and indeed found that only a narrow range of halo masses should host active quasars, with a median characteristic mass of $M_{\text{halo}} \sim 1.3 \times 10^{13}M_{\odot}$. As pointed out by the authors, only future surveys that will be able to observe the faint quasars in their quiescent stage will be able to test this picture, and to rule out the

alternative hypothesis of luminosity-dependent quasar clustering.

Compared to other theoretical work, we do not have to make assumptions about the halo population hosting BHs nor about the relation between the halo mass and the quasar luminosity (or BH mass), since they are a natural outcome of the simulation of the galaxy formation process. However, we have to make assumptions about the physics of BH accretion, and what triggers AGN activity. In what follows, we are especially interested in testing the assumption that galaxy mergers are the primary physical mechanism responsible for triggering accretion onto massive BHs. To this end we explore the simulation predictions for quasar clustering and the quasar luminosity function obtained with a pure Eddington-limited lifetime model and a model that includes a low-luminosity accretion mode as described in the previous chapter and in Hopkins et al. (2005) and Marulli et al. (2008).

3.2 Models for Black Hole accretion and emission

As described in details in the previous chapter, in the semi-analytic model a fraction of the mass of a halo is assigned to baryons in the form of hot gas, which, as time evolves, will cool and form a galaxy. We also add a ‘seed’ BH of very small mass to each newly formed halo. As galaxies evolve, their central BHs are allowed to grow through mergers with other BHs and through gas accretion during the ‘radio mode’ and during the ‘quasar mode’. The quasar mode is the phase during which BHs accrete most of their mass, and during which BHs can shine as bright AGN. In this section we describe the different phases of BH growth and emission adopted in our model to generate the AGN population used in the rest of the chapter, and review some basic properties of our simulated AGN.

3.2.1 BH seeding

In §1.5.1, we described different scenarios for the origin of supermassive black holes. Essentially, there are two competing scenarios: either they are the remnants of Pop III stars (with masses of $\sim 10^2 - 10^3 M_\odot$), or could they could originate from the direct collapse of a low-angular momentum gas cloud (with masses $\sim 10^5 M_\odot$).

Here we assume here that every newly-formed galaxy hosts a central BH of $10^3 M_\odot$. This seed BH may then start accreting through the processes described below. Note however that a much larger seed would only influence the BH evolution in our model at very high redshifts, but it would not influence the results in the redshift range of main interest in what we present here, simply because the large growth factor soon cancels any information about the seed mass.

3.2.2 Radio mode

When a static hot halo has formed around a galaxy, we assume that a fraction of the hot gas continues to accrete onto the central BH, causing low-level ‘radio’ activity in the galaxy center. For clarity, this phase, which is called in jargon *radio mode* because it is associated with the activity of radio galaxies at the centre of galaxy clusters Best et al. (2005), does not include the powerful emission of FR II radio loud QSOs. Following Croton et al. (2006), the BH mass accretion rate during these phases of *radio mode* activity is postulated to scale as follows:

$$\dot{M}_{\text{BH,R}} = \kappa_{\text{AGN}} \left(\frac{M_{\text{BH}}}{10^8 M_\odot} \right) \left(\frac{f_{\text{hot}}}{0.1} \right) \left(\frac{V_{\text{vir}}}{200 \text{ km s}^{-1}} \right)^3, \quad (3.1)$$

where M_{BH} is the BH mass, f_{hot} is the fraction of the total halo mass in the form of hot gas, V_{vir} is the virial velocity of the halo and κ_{AGN} is a free parameter set equal to $7.5 \times 10^{-6} M_{\odot} \text{yr}^{-1}$ in order to reproduce the turnover at the bright end of the galaxy luminosity function. Since f_{hot} is approximately constant for $V_{\text{vir}} \gtrsim 150 \text{ km s}^{-1}$, the dependence of $\dot{M}_{\text{BH,R}}$ on this quantity has little effect. Note that the accretion rate given by equation (3.1) is typically orders-of-magnitude below the Eddington limit. In fact, the total mass growth of BHs in the *radio* relative to the *quasar mode* (discussed below) is negligible Croton et al. (2006).

It is also assumed that *radio mode feedback* injects energy efficiently into the surrounding medium, which can reduce or even stop the cooling flows in halo centers. The mechanical heating generated by this kind of BH mass accretion is parameterized as $L_{\text{BH}} = \epsilon \dot{M}_{\text{BH}} c^2$, where $\epsilon = 0.1$ is the *accretion efficiency* and c is the speed of light. The heating modifies the infall rate due to cooling according to:

$$\dot{m}'_{\text{cool}} = \dot{m}_{\text{cool}} - \frac{L_{\text{BH}}}{0.5V_{\text{vir}}^2}. \quad (3.2)$$

For consistency we never allow \dot{m}'_{cool} to fall below zero. In this scenario, the effectiveness of radio AGN in suppressing cooling flows is greatest at late times and for large values of the BH mass, which is required to successfully reproduce the luminosities, colors and clustering of low-redshift bright galaxies.

3.2.3 Quasar mode

This is the phase during which BHs accrete cold gas and build up most of their final mass. This phase has recently acquired the jargon name *quasar mode* because it is only through the very efficient accretion of cold gas that a BH can shine as a bright AGN, but we stress that this phase is also meant to include accretion of cold gas at low Eddington ratios.

The tight relation observed locally between BH mass and the host bulge (e.g., Magorrian et al. 1998; Ferrarese & Merritt 2000; Tremaine et al. 2002; Marconi & Hunt 2003) suggests that bulges and BHs might form during the same events and/or they strongly influence each other as they evolve. Simulations have shown that during mergers of gas-rich disk galaxies gas is channeled toward the nuclei of the merging galaxies through gravitational torques Barnes & Hernquist (1996), and this process can indeed be responsible for the formation of bulges as well as for BH accretion Springel et al. (2005b); Di Matteo et al. (2005).

Based on these results, and following Kauffmann & Haehnelt (2000), in the present work we assume that the quasar phase is triggered by galaxy mergers. In practice, during merger events, we assume that the BHs hosted by the merging galaxies instantaneously coalesce and form a single BH whose mass is the sum of the progenitor BHs, and that this resulting BH starts accreting a fraction of the available cold gas. In the previous chapter we found that we need to feed BHs more efficiently at high redshifts in order to build massive BHs by $z = 5$ without invoking super-Eddington accretion or much more massive seed masses. In this work we assume that the amount of cold gas accreted during each merger depends linearly on redshift Croton (2006):

$$\Delta M_{\text{BH,Q}} = \frac{f'_{\text{BH}} m_{\text{cold}}}{1 + (280 \text{ km s}^{-1} / V_{\text{vir}})^2} (1 + z_{\text{merg}}), \quad (3.3)$$

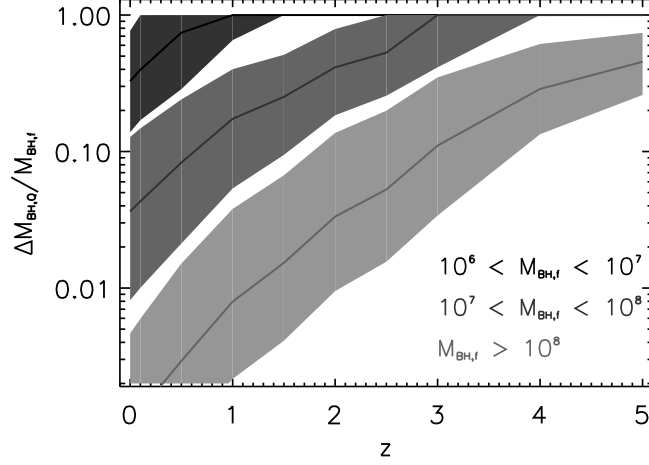


Figure 3.1: Median accreted gas $\Delta M_{\text{BH},Q}$ relative to the final BH mass for each accretion event, for three different final mass bins. The filled contours enclose the 25 and 75 percentiles.

where m_{cold} is the total mass of cold gas in the final galaxy, z_{merg} is the redshift of the merger and

$$f'_{\text{merg}} = f_{\text{merg}} (m_{\text{sat}}/m_{\text{central}}), \quad (3.4)$$

where $f_{\text{merg}} \approx 0.02$ is a normalization parameter chosen to match the observed local $M_{\text{BH}} - M_{\text{Bulge}}$ relation and $m_{\text{sat}}/m_{\text{central}}$ is the mass ratio of the merging galaxies.

In Figure 3.1 we show, as a function of redshift, the median accreted mass $\Delta M_{\text{BH},Q}$, relative to the value of the BH mass at the end of a single accretion event, for three final mass bins. Small-mass BHs accrete efficiently at all epochs (higher curve), whereas BHs that, at the end of the accretion event, end-up in massive objects (lower curve) accrete most of their mass at early times: at low-redshifts, the amount of ‘new’ gas accreted is relatively small compared to the mass already acquired. This behavior is in agreement with the apparent ‘anti-hierarchical’ growth of BHs: observations in the soft and hard X-rays have shown that the number density of bright AGN declines with decreasing redshift, while the density of fainter active nuclei shows the opposite trend (Cowie et al. 2003; Steffen et al. 2003; Ueda et al. 2003; Hasinger et al. 2005). Heckman et al. (2004) used the emission lines of type 2 AGN observed with SDSS to investigate whether the decrease of the space density of bright objects is simply due to a decrease in the accretion rate or a decrease in the typical mass of actively growing BHs. These authors found that the typical mass of BHs that are today actively accreting is $\lesssim 10^7 M_{\odot}$, and that larger BHs are experiencing little accretion.

In the previous chapter we showed that, at $z = 0$, this model for BH accretion is able to reproduce not only the observed $M_{\text{BH}} - M_{\text{Bulge}}$ relation (Häring & Rix 2004), but also other scaling relations, such as the ones between the BH mass and the galaxy central velocity dispersion or color (Marconi & Hunt 2003; Ferrarese & Ford 2005). The $z = 0$ differential mass density of our simulated BHs is shown in Figure 3.2 compared with the observational estimate of Shankar et al. (2004). The corresponding local mass density (for our cosmology with $h = 0.73$) is $\rho_{\text{BH}} = 3.35 \times 10^5 M_{\odot} \text{Mpc}^{-3}$, which is in good agreement with Graham & Driver (2007) (we refer to these authors for a summary of the values quoted in the literature).

To study the redshift evolution of the BH population, it is important to not only to consider

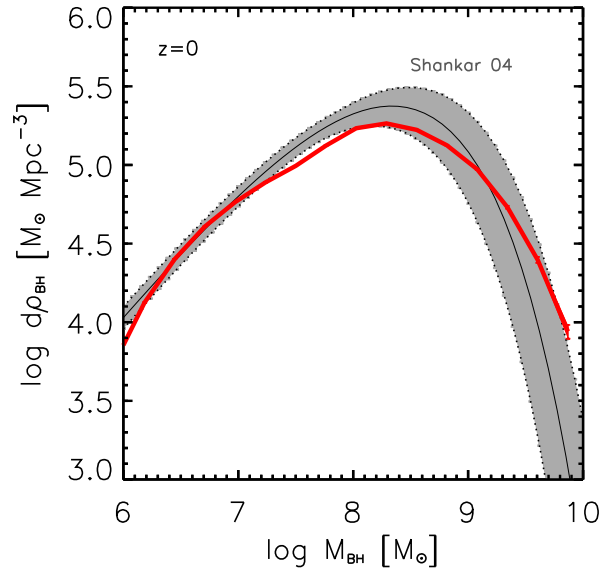


Figure 3.2: Differential BH mass density at $z = 0$ (red thick line) compared to the observational estimate of Shankar et al. (2004) (solid black line, with errors enclosed in the grey shaded area).

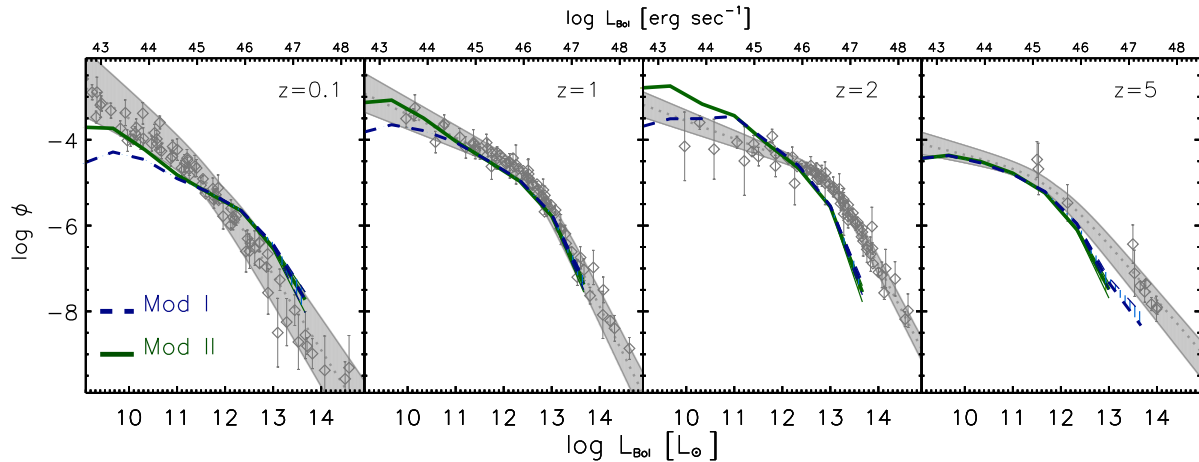


Figure 3.3: Bolometric luminosity function assuming Eddington-limited accretion (Mod I, blue-dashed curve), or Eddington-limited accretion followed by a quiescent phase of low luminosity (Mod II, green-solid curve), with errors calculated using Poisson statistics. The luminosity functions are compared with the compilation of Hopkins et al. (2007b) (grey points with best fit given by the grey band).

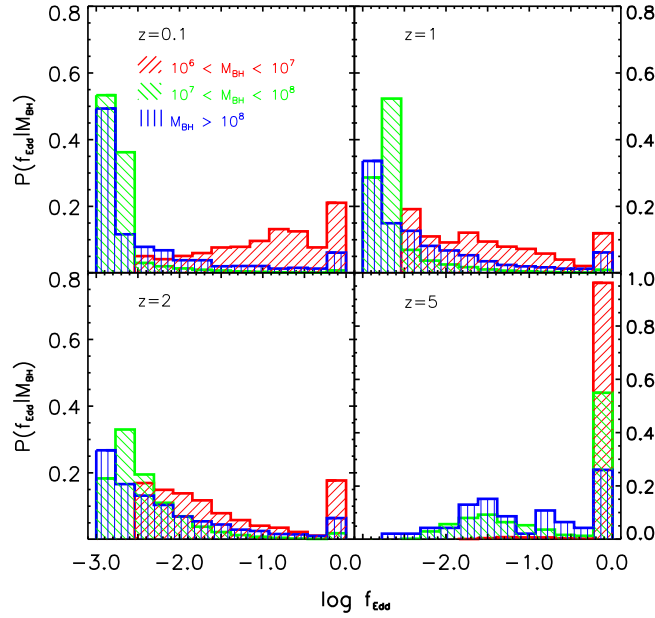


Figure 3.4: Probability distribution of f_{Edd} , as a function of BH mass and redshift. The limits in the BH mass bins are shown in the first panel in units of M_{\odot} . At high redshift, most of the BHs accrete at the Eddington limit. Today, only the smallest BHs are experiencing efficient accretion.

the evolution of the BH mass, but also to relate this to the radiation output of the accretion. If we are interested in the instantaneous brightness of a quasar, we not only need to calculate how much mass it accretes, but also how long this takes. In other words, we need to model the light curve of individual phases of quasar activity. In the previous chapter we introduced and tested different models for the AGN light curve, and we compared our results with the AGN bolometric luminosity function of Hopkins et al. (2007b). We here briefly describe the light curve models adopted for the present study.

At any given time, the bolometric luminosity emitted by an accreting BH is given by

$$\begin{aligned}
 L_{\text{bol}}(t) &= \epsilon \dot{M}_{\text{accr}}(t) c^2 = \frac{\epsilon}{1 - \epsilon} \dot{M}_{\text{BH}}(t) c^2 \\
 &= f_{\text{Edd}}(t) L_{\text{Edd}}(t) = f_{\text{Edd}} \frac{M_{\text{BH}}(t)}{t_{\text{Edd}}} c^2,
 \end{aligned} \tag{3.5}$$

where ϵ is the radiative efficiency, L_{Edd} is the Eddington luminosity, f_{Edd} is the fraction of Eddington luminosity emitted, and $t_{\text{Edd}} = \sigma_{\text{T}} c / (4\pi m_p G) \sim 0.45 \text{ Gyr}$ (note that we are here considering only the luminosity emitted during the *quasar mode* phase, thus ignoring the contribution from $\dot{M}_{\text{BH,R}}$). If, at any given time, the radiative efficiency and the Eddington ratio are known, the accretion rate is given by:

$$d \ln M_{\text{BH}}(t) = \frac{dt}{t_{\text{ef}}(t)}, \tag{3.6}$$

where $t_{\text{ef}}(t) = \frac{\epsilon}{1 - \epsilon} \frac{t_{\text{Edd}}}{f_{\text{Edd}}(t)}$ is the e-folding time ($t_{\text{ef}} \equiv t_{\text{Salpeter}}$ if $f_{\text{Edd}} = 1$).

For simplicity, we assumed a constant radiative efficiency $\epsilon = 0.1$ (average value for a thin

accretion disk, as discussed in the Appendix A), and we explored different models for the time-evolution of f_{Edd} . In this work we choose not to explore all the four models discussed in Chapter 2. Instead, we will focus on two of them, which we regard as representative cases. The first one illustrates the simple case of an AGN that shines at the Eddington luminosity. It represents a very simple model commonly used in the literature, that we regard as a reference case, despite the fact that, as shown in the previous chapter, fails to reproduce the AGN luminosity function at low and high redshifts. The second model is very close to the model called 'best' in the previous chapter and illustrates the impact of adopting a non trivial AGN light-curve, motivated by numerical experiments. As discussed in Chapter 2 this second model provides a better fit to the AGN luminosity function. In what follows, we present a more detailed description of the two models:

- *Model I:* $f_{\text{Edd}}(t) = \text{const} = 1$. This is the simplest case, in which we assume that, when active, BHs accrete and radiate at the Eddington limit.
- *Model II:* Here we assume that BHs undergo an Eddington-limited phase that leads to a peak luminosity L_{peak} , which is then followed by a long quiescent phase at progressively lower Eddington ratios. Following the work of Hopkins et al. (2005), we assume that in this long quiescent phase the average time that an AGN spends in a logarithmic luminosity interval can be approximated by:

$$\frac{dt}{d \ln L_{\text{bol}}} = |\alpha| t_9 \left(\frac{L_{\text{bol}}(t)}{10^9 L_{\odot}} \right)^{\alpha}, \quad (3.7)$$

where $t_9 \equiv t_Q(L' > 10^9 L_{\odot})$ and $t_Q(L' > L)$ is the total AGN lifetime above a given luminosity L . Hopkins et al. (2005) found from merger simulations that $t_9 \sim 10^9$ yr over the range $10^9 L_{\odot} < L_{\text{bol}} < L_{\text{peak}}$; here, we assume always $t_9 = 10^9$ yr. In the range $10^{10} L_{\odot} \lesssim L_{\text{peak}} \lesssim 10^{14} L_{\odot}$, Hopkins et al. (2005) also found that α is a function of only the AGN luminosity at the peak of its activity, L_{peak} , given by $\alpha = -0.95 + 0.32 \log(L_{\text{peak}}/10^{12} L_{\odot})$, with $\alpha = -0.2$ as an upper limit.

In this scenario, the peak luminosity L_{peak} reached at the end of the first accretion phase is $L_{\text{Edd}}(M_{\text{BH,peak}})$, where

$$M_{\text{BH,peak}} = M_{\text{BH}}(t_{\text{in}}) + \mathcal{F} \cdot \Delta M_{\text{BH,Q}} \cdot (1 - \epsilon). \quad (3.8)$$

Here $M_{\text{BH}}(t_{\text{in}})$ is the BH mass at the beginning of the accretion, $\Delta M_{\text{BH,Q}}$ is the fraction of cold gas mass accreted, and \mathcal{F} sets the fraction of gas that is accreted during the Eddington-limited phase. After this first phase, the BH keeps accreting the remaining cold gas at a progressively slower rate, as described by equation (3.7). In the modeling of the previous chapter, we set $\mathcal{F} = 0.7$, a value that balances the needs of efficiently building-up massive BHs and of explaining low- f_{Edd} BHs in the local Universe. Most of the available gas is therefore accreted during the Eddington-limited phase, and the light curve model introduced by Hopkins et al. (2005) is used to describe only the quiescent phase.

A direct comparison of the luminosity functions obtained using Mod I and Mod II is shown in Figure 3.3. Mod I and Mod II give a similar population of high-luminosity AGN: bright AGN are always produced by BHs accreting close to the Eddington limit. At high redshifts, the faint-end of the luminosity function produced by the two models is very similar as well, suggesting that at very high redshifts BHs of all masses typically accrete at $f_{\text{Edd}} = 1$. It is in the faint-end of the luminosity

function at low redshifts where the two models predict a different behavior for the AGN luminosity: only Mod II (with $\mathcal{F} = 0.7$) is able to fit the low-redshift faint-end of the luminosity function, implying that a model in which BHs experience long, quiescent accretion phases can indeed explain the number density of low-luminosity AGN at low redshift. This is because in Mod II the average lifetime of AGN is much higher (a larger fraction of time is spent at low luminosities); it is therefore more probable to observe, at a given redshift, an AGN shining at low luminosities.

We have already mentioned that observations indicate that the more massive BHs have accreted most of their mass at early times, whereas in the local Universe BHs with a mass $\lesssim 10^7 M_\odot$ are accreting efficiently (Heckman et al. 2004). These results have been confirmed more recently by Netzer & Trakhtenbrot (2007), who found that at all redshifts f_{Edd} is smaller for larger mass BHs. Similar compilations that use emission lines to estimate Eddington ratios have shown that the f_{Edd} of quasars seems to be log-normally distributed, with a peak around $f_{\text{Edd}} \approx 10^{-1} - 10^{-0.6}$ (Kollmeier et al. 2006; Shen et al. 2008). In Figure 3.4 we show, for Mod II, the redshift evolution of the probability distribution $P(f_{\text{Edd}}|M_{\text{BH}})$ of the Eddington ratios, given the BH mass. At high redshifts all BHs accrete close to the Eddington limit. At lower redshifts instead only the smaller BHs are accreting at high Eddington ratios, while the more massive ones accrete at much lower rates. Note that this figure includes all active BHs from our simulation, and therefore a direct comparison with observed data is not possible. We postpone a more detailed analysis of this point to a future work, but we stress that a model with a quiescent phase could account for the low-redshift behavior of the more massive BHs (see also the recent work of Hopkins & Hernquist 2008).

3.3 Clustering properties

In this section we discuss the clustering properties of our simulated AGN sample. We first compare the predicted two-point correlation with the autocorrelation of the DM particles. We then compare the AGN clustering properties with the clustering of the dark matter haloes of the Millennium simulation, and in particular examine the differences between Mod I and Mod II. We then explore the luminosity dependence of the clustering of the global AGN population and of an optically-visible sub-sample. Finally, we directly compare the clustering of our simulated L_* quasars with recent observational results.

3.3.1 Brief description of the correlation parameters used

We refer to Appendix B for the definition of the two-point spatial correlation function $\xi(r)$ and the correlation length r_0 .

At scales between $\sim 1 h^{-1}\text{Mpc}$ up to few tens of Mpc the observed quasar correlation function can be approximated by a power-law, usually expressed as:

$$\xi(r) = \left(\frac{r}{r_0}\right)^{-\gamma}. \quad (3.9)$$

To calculate r_0 , unless otherwise stated, we will fit the two-point correlation with such a power-law in the range $1 < r < 20 h^{-1}\text{Mpc}$ (see the next subsection for details on this).

As also described in Appendix B, the *bias* between two classes of objects (e.g., AGN and dark matter) is defined as the square-root of the ratio of the corresponding two-point correlation

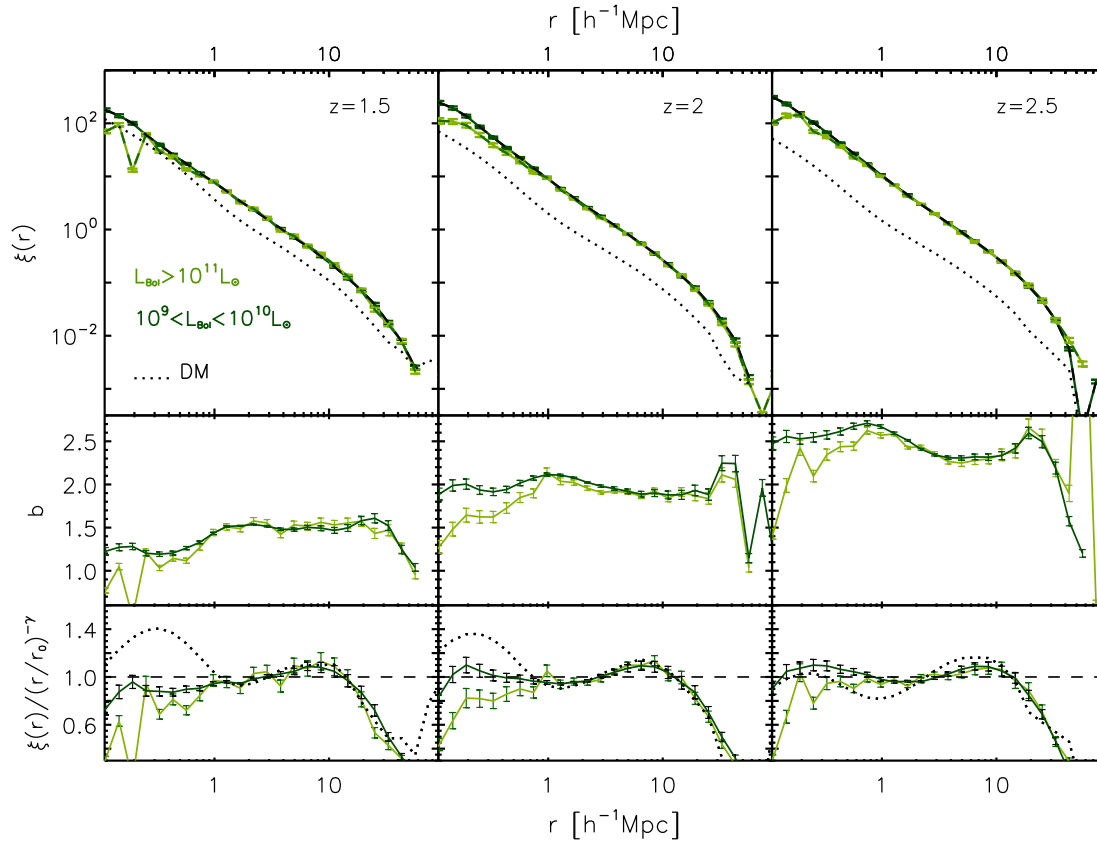


Figure 3.5: *Upper panels: two-point correlation function of the Millennium dark matter particles (dotted line) compared with the correlation of the AGN population, divided into a faint and a luminous subsample, depending on their bolometric luminosity (as indicated in the first panel. Central panels: bias between the two AGN samples and the dark matter as a function of scale. Lower panels: two-point correlation from the upper panels divided by a power-law fit. If $\xi(r)$ was a perfect power-law, the ratio should be constant with scale and equal to unity (dashed horizontal line). We refer to the text for a description of the errors.*

functions:

$$b_{\text{AGN, DM}} \equiv \sqrt{\frac{\xi_{\text{AGN}}(r)}{\xi_{\text{DM}}(r)}}. \quad (3.10)$$

In principle, an accurate determination of the ‘cosmic-variance’ errors of these quantities as measured from the simulation could be calculated from the variance over many different realizations of the universe. As we have only one simulation as large as the Millennium run at our disposal, this is not practical. A reasonable alternative is to estimate the errors by subdividing the whole Millennium volume into sub-cubes, and then by calculating the variance among the measurements for each of these sub-volumes, an approach we will follow here.

In order to directly estimate the impact of the cosmic variance in the predicted AGN clustering, it is necessary to model the AGN properties in mock samples designed to match the real ones. We have followed this approach in a parallel work (Marulli et al. 2009), where we have used the same semi-analytic model presented here to construct mock AGN catalogues mimicking the Chandra deep fields.

3.3.2 AGN and dark matter clustering

We here show the results for the shape of the two-point correlation of the AGN sample, comparing it to the one of the Millennium dark matter particles. For simplicity, we present only the results obtained with Mod II, since the conclusions of this subsection are independent of the assumed model for the light curve.

In the top panels of Figure 3.5, we plot the two-point correlation of the DM particles (dotted line) and the two-point correlation of faint ($L_{\text{Bol}} < 10^{10} L_{\odot}$) and bright ($L_{\text{Bol}} > 10^{11} L_{\odot}$) AGN (dashed lines), at three different redshifts. As can be seen at a glance, the main difference between $\xi_{\text{DM}}(r)$ and $\xi_{\text{AGN}}(r)$ lies in the normalization, they are substantially biased relative to each other. This bias ($[\xi_{\text{AGN}}(r)/\xi_{\text{DM}}(r)]^{1/2}$) is plotted in the next set of panels of Figure 3.5. The bias is approximately scale-independent (at least in the range $1 < r < 20 h^{-1}\text{Mpc}$), and its average value increases with redshift. The error $\sigma_{\log \xi_{\text{AGN}}}(r)$ of the two-point correlation is here the variance (in log-space) of the two-point correlation functions calculated in eight sub-volumes. The errors on the bias have been calculated assuming negligible error for DM autocorrelation. By error propagation, the error on the bias is then $\sigma_b(r) = b(r) \sigma_{\log \xi_{\text{AGN}}}(r) (\ln 10)/2$.

Finally, in the lower panels of Figure 3.5 we show how the two-point correlations deviate from a power-law, that is, we divide the calculated $\xi(r)$ by the fit calculated using eq. (3.9). As is well known (e.g., Springel et al. 2005c), the DM correlation function deviates from a pure power-law at low and intermediate scales. The AGN correlation function shows a similar shape at intermediate scales ($r \sim \text{few } h^{-1}\text{Mpc}$), but not at small scales, where the AGN two-point correlation function is a significantly ‘better’ power-law than that of the DM. This is highly reminiscent of the findings for the clustering of galaxies (Springel et al. 2005c).

As we will again see in the next subsection, the lack of a strong correlation signal at small scales is due to the fact that our BHs accrete gas and can shine as bright AGN only after merger events, which, in our model, happen mainly in the central galaxies of dark matter haloes (whose mean separation is $\approx 1 h^{-1}\text{Mpc}$). Also note that each of our mergers lights up only one BH, the merged BH of the two progenitor galaxies, i.e. our model does not account for the possibility that the two BHs exhibit activity as a close quasar pair already prior to coalescence. Also, as a BH is still accreting cold gas, it can happen that its host halo merges with another halo which could have

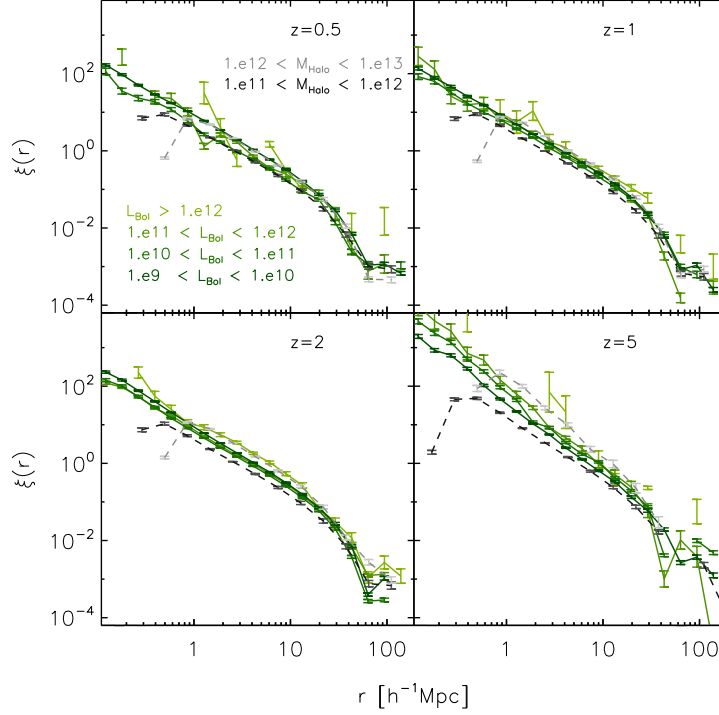


Figure 3.6: Two-point correlation function for the AGN sample compared to the two-point correlation of the Millennium FOF haloes, at various redshifts. The AGN are divided into 4 luminosity bins (depending on the bolometric luminosity), whereas the haloes are divided into two bins, depending on the value of their virial mass in units of $h^{-1}M_{\odot}$. The AGN in this figure have been obtained using Mod II for the light curve. In Figure 3.8, the main difference in the correlation between the two models is highlighted.

at its center another accreting BH. This is also why the correlation power at scales $\lesssim 1 h^{-1}\text{Mpc}$ is non-zero, but negligible. In the future, we plan to compare a pure merger-triggered AGN scenario, with a model in which the possible galaxy disk instability also could contribute in feeding BHs. In this last case we expect a larger AGN halo occupation distribution (number of AGN in a single halo), and a different behavior in the small-scale clustering regime.

3.3.3 AGN and halo clustering

In this subsection we compare the AGN clustering with the clustering of the Millennium haloes. In our model, BHs are allowed to accrete cold gas only during merger events, which are experienced mainly by the galaxies sitting at the centers of FOF haloes. As discussed above, only a small fraction of AGN can be hosted by satellite haloes. Due to this uncertainty in the quasar pair regime, we focus in the present work on the clustering on intermediate and large scales, and we refrain from drawing strong conclusions from the results at scales much smaller than the average halo separation.

In Figure 3.6, we show at different redshifts the two-point correlation function of the AGN population, divided in four luminosity bins depending on their intrinsic bolometric luminosity. This is compared with the two-point correlation of the FOF haloes, divided into two bins according to their virial mass. The AGN shown in this figure have been obtained using Mod II for the light curve. The corresponding correlation lengths are shown in the lower panel of Figure 3.7. In the

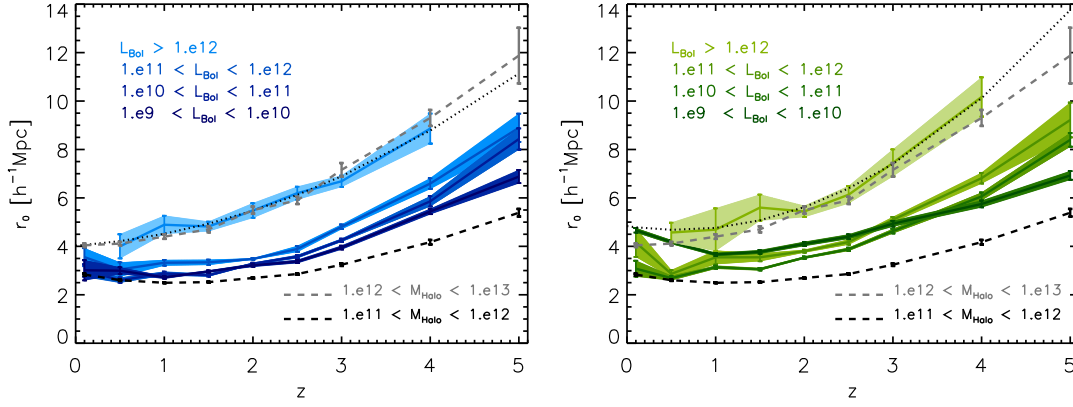


Figure 3.7: Correlation length as a function of redshift of the AGN sample divided in four bolometric luminosity bins, compared with the correlation length of the Millennium FOF haloes divided in two mass bins. The AGN have been obtained using Mod I (upper panel) or Mod II (lower panel) as light curve models, respectively. Fits to the brightest bins are shown with the dotted curve.

upper panel of the same figure the correlation lengths of the AGN obtained using Mod I are plotted, also divided in four luminosity bins. In the analysis of the results, we allow the exponent γ of the power-law ansatz for the correlation function to vary in each fit. The values of r_0 and γ for the two models thus obtained are given in Table 3.1. We also fitted the brightest bin with a quadratic function ($r_0(z) = a + b(1+z) + c(1+z)^2$) to compactly summarize the results, and the values of the coefficients are given at the end of each table.

Comparing the values of the correlation lengths obtained with the two models, we do not find significant differences, except for the faintest AGN ($L_{\text{Bol}} < 10^{10} L_{\odot}$). An enlarged view of the behavior of the correlation strength of these faint objects obtained with Mod I (solid blue curve) and with Mod II (dotted green curve) is shown in Figure 3.8. While at high redshifts there is hardly any difference between the two models, at low redshift the faint objects obtained with Mod II are much more strongly clustered. This is because most of the population is composed of large BHs that are accreting at low f_{Edd} (as shown in Figure 3.4) and that are hosted by large haloes. In the lower panel of Figure 3.8, we see that the correlation length of the faint objects obtained with Mod II is comparable to the ones of haloes with $M_{\text{vir}} \approx 10^{12} - 10^{13} M_{\odot}$, while faint objects obtained with a pure Eddington-limited accretion model are sitting in haloes of much lower mass. Observational clustering measurements have been used in recent years to estimate the typical halo masses that host quasars (e.g., Porciani et al. 2004; Grazian et al. 2004; Croom et al. 2005). This is usually done by comparing the bias of observed quasars with the halo bias obtained from analytical estimates (e.g., Mo & White 1996; Sheth & Tormen 1999). With our approach, the host halo mass is an output of the simulation, and therefore we can directly examine the relation between black hole mass, quasar luminosity and halo mass. In §3.4, we exploit this for a direct study of the dark environment of luminous BHs.

Based on Figure 3.7, it seems that the redshift-evolution of the clustering of quasars is consistent with the redshift-evolution of the clustering of dark matter haloes (quasars of a given luminosity reside at all times in haloes of a fixed mass). Again, the only substantial difference to this trend is for the faint objects obtained with Mod II: since their clustering is more constant with redshift, it implies that their typical host halo mass changes with redshift.

Mod I								
z	L_1		L_2		L_3		L_4	
	r_0	γ	r_0	γ	r_0	γ	r_0	γ
0.1	-	-	3.55 ± 0.37	1.4	3.0 ± 0.26	1.79	3.01 ± 0.42	1.5
0.5	4.0 ± 0.5	1.69	3.04 ± 0.29	1.49	2.6 ± 0.11	1.53	3.0 ± 0.14	1.49
1.0	4.89 ± 0.37	1.62	3.32 ± 0.12	1.63	2.88 ± 0.08	1.5	2.72 ± 0.06	1.52
1.5	4.82 ± 0.2	1.79	3.34 ± 0.11	1.57	2.81 ± 0.06	1.56	2.96 ± 0.04	1.57
2.0	5.48 ± 0.3	1.71	3.48 ± 0.03	1.55	3.28 ± 0.04	1.55	3.22 ± 0.06	1.5
2.5	6.2 ± 0.27	1.54	3.89 ± 0.12	1.58	3.57 ± 0.07	1.54	3.37 ± 0.07	1.55
3.0	6.69 ± 0.23	1.79	4.81 ± 0.09	1.6	4.25 ± 0.06	1.59	3.95 ± 0.08	1.57
4.0	8.86 ± 0.62	1.77	6.59 ± 0.22	1.76	5.86 ± 0.21	1.7	5.44 ± 0.11	1.66
5.0	-	-	8.89 ± 0.58	2.04	8.43 ± 0.44	1.89	6.88 ± 0.27	1.81
fit for L_1 : $r_0 = a + b(1+z) + c(1+z)^2$, with $a, b, c = [4.01, -0.21, 0.23]$								

Mod II								
z	L_1		L_2		L_3		L_4	
	r_0	γ	r_0	γ	r_0	γ	r_0	γ
0.1	-	-	4.15 ± 0.6	1.69	3.08 ± 0.33	1.72	4.66 ± 0.09	1.61
0.5	4.57 ± 0.96	1.96	2.86 ± 0.15	1.27	2.69 ± 0.1	1.45	4.18 ± 0.08	1.58
1.0	4.69 ± 0.88	1.62	3.55 ± 0.28	1.58	3.14 ± 0.06	1.51	3.67 ± 0.07	1.56
1.5	5.6 ± 0.53	1.89	3.55 ± 0.16	1.52	3.05 ± 0.05	1.53	3.77 ± 0.07	1.56
2.0	5.44 ± 0.23	1.68	3.8 ± 0.06	1.54	3.53 ± 0.04	1.56	4.1 ± 0.09	1.58
2.5	6.13 ± 0.36	1.52	4.18 ± 0.11	1.57	3.88 ± 0.07	1.56	4.4 ± 0.09	1.59
3.0	7.45 ± 0.55	1.72	5.1 ± 0.11	1.65	4.63 ± 0.09	1.6	4.94 ± 0.12	1.64
4.0	10.17 ± 0.81	1.82	6.82 ± 0.22	1.77	6.06 ± 0.16	1.77	5.75 ± 0.14	1.72
5.0	-	-	9.22 ± 0.72	2.01	8.4 ± 0.28	1.87	6.93 ± 0.18	1.84
fit for L_1 : $r_0 = a + b(1+z) + c(1+z)^2$, with $a, b, c = [5.84, -1.47, 0.46]$								

Table 3.1: Upper table: Values of the correlation lengths shown in the left panel of Figure 3.7. Lower table: the same, but for the AGN obtained with Mod II (right panel of Figure 3.7). We also added the values of the corresponding power-law slope γ . L_1 corresponds to the brighter bin, L_4 to the faintest. We also give the values of the parameters of the quadratic fit done on r_0 for the brightest bin.

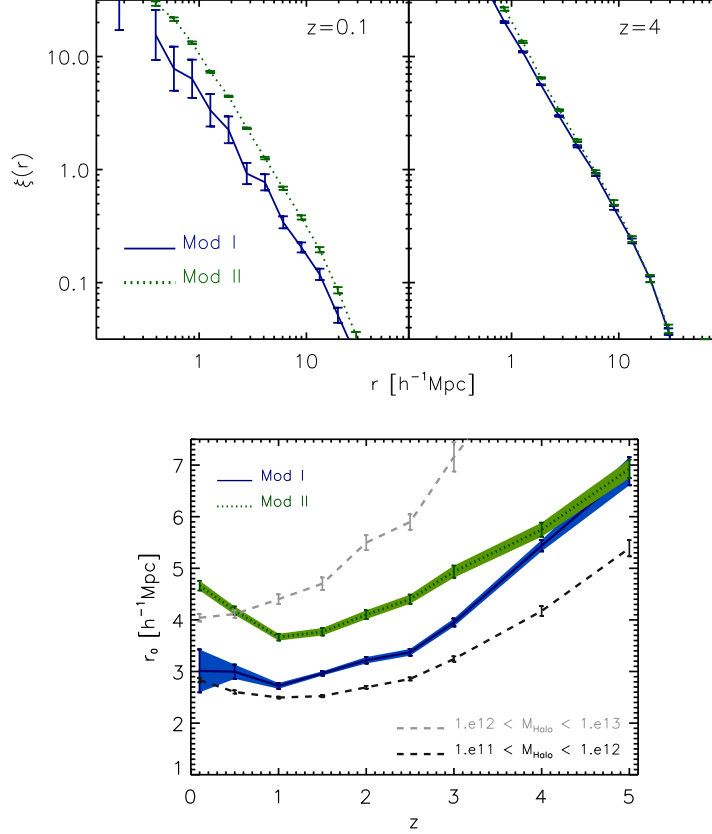


Figure 3.8: We compare here the correlation function of faint AGN ($L_{\text{Bol}} < 10^{10}L_{\odot}$) obtained using Mod I (solid blue line) and Mod II (dotted green line). We show the result at very high redshift, where there is no difference in the two models, and at low redshift, where the difference becomes significant. In the lower panel the corresponding correlation function is shown as a function of redshift, and the correlation of FOF haloes is shown for reference.

3.3.4 Luminosity dependence of AGN clustering and comparison with data

In this subsection we first examine the dependence of AGN clustering on luminosity, looking at the global population, and then considering a subsample that would be observable in the optical band.

Observationally, quasar clustering seems not to depend significantly on luminosity (e.g., Porciani et al. 2004; Croom et al. 2005; da Ângela et al. 2008). Only Shen et al. (2009b) found indications of a luminosity-dependence of the clustering when they compared the two-point correlation of their 10% brightest objects with the rest of the sample. Figure 3.7 provides information on how the correlation length evolves with luminosity in our models. Except for the faintest bin (see Figure 3.8), there is not a substantial difference between the two models, as pointed out before. In both models we see some moderate evolution with luminosity, and in particular, in both cases the brightest quasar bin is substantially more strongly clustered than the lower luminosities.

Note that in this analysis a very large range in luminosities is covered (≈ 5 dex in luminosity, corresponding to ≈ 12.5 absolute magnitudes). Observationally, the accessible luminosity range is always much smaller than that. To give predictions that can be compared with future observations,

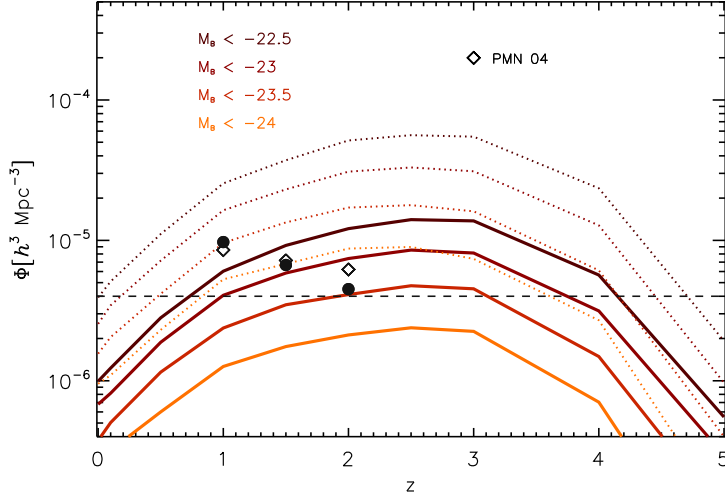


Figure 3.9: Space density as a function of redshift for four subsamples selected with B-band magnitude cuts as indicated on the plot. The solid lines are give the space density when the possible obscuration is taking into account. If we allow all our objects to be optically visible, we obtain the space densities described by the dotted curves. The dashed line marks the point below which we have less than 500 objects remaining in in the Millennium simulation volume. The open diamonds are the observed values from Porciani et al. (2004), obtained in different magnitude ranges depending on the redshift (see text for details). The number densities obtained with our model using the same magnitude ranges and accounting for obscuration are indicated with the filled circles.

we now extract from the global AGN population sub-samples of optically visible bright AGN. First of all, to account for obscuration, we calculate the fraction of objects that would be visible in the optical using the ‘observable fraction’ from Hopkins et al. (2007b). This gives, as a function of luminosity, the probability for an object to be seen in a given band:

$$f(L) = f_{46} \left(\frac{L}{10^{46} \text{ergs}^{-1}} \right)^\beta, \quad (3.11)$$

where $f_{46} = 0.260$ and $\beta = 0.082$) for the B-band.

To convert from bolometric luminosity to B-band luminosity, we used the bolometric corrections again from Hopkins et al. (2007b):

$$\frac{L_{\text{bol}}}{L_{\text{band}}} = c_1 \left(\frac{L_{\text{bol}}}{10^{10} L_\odot} \right)^{k_1} + c_2 \left(\frac{L_{\text{bol}}}{10^{10} L_\odot} \right)^{k_2}, \quad (3.12)$$

where (c_1, k_1, c_2, k_2) are respectively $(6.25, -0.37, 9.0, -0.012)$ for the B-band.

In Figure 3.9 we show as a function of redshift the number density of our simulated AGN for different luminosity cuts (solid lines). In order to directly compare our number densities with the values inferred from observational data used for clustering measurements, we calculated in the same figure the number density of objects in the magnitude ranges given by Porciani et al. (2004) at three different redshifts: the values of M_{min} and M_{max} are $[-25.32, -21.72]$ at $z \sim 1.0$, $[-25.97, -22.80]$

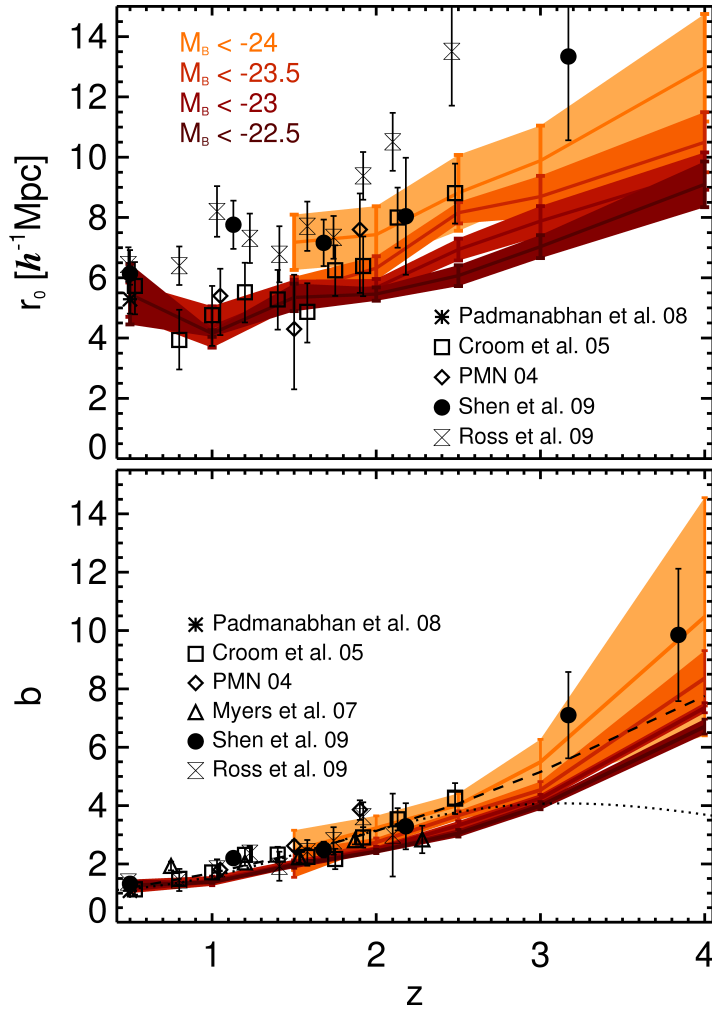


Figure 3.10: Correlation length (top panel) and bias (lower panel) for the AGN selected using the cuts of Figure 3.9 (neglecting the effects of obscuration). Due to lack of enough objects, the clustering properties of the two brightest bins are calculated only down to $z = 1.5$. Our predictions are plotted together with observational data (for the Shen et al. (2009b), we included their lower estimates). For the bias, the dotted line is the prediction of Hopkins et al. (2007a) and the short-dashed line is the best fit from Croom et al. (2005).

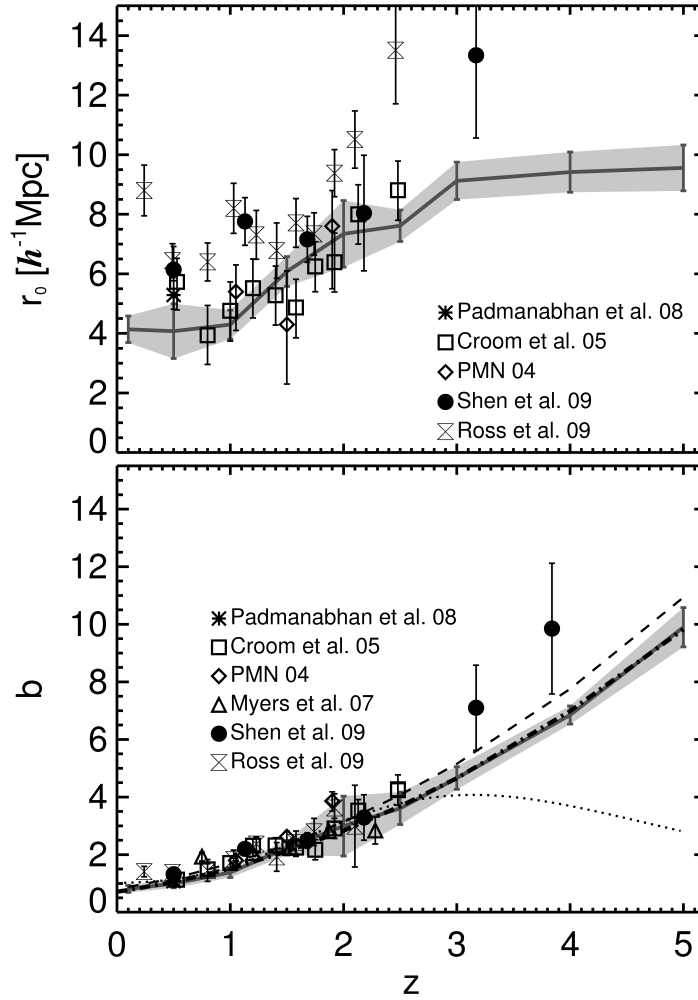


Figure 3.11: Correlation length (top panel) and bias (lower panel) for L_* quasars. The gray line is our prediction (with errors enclosed in the grey area). The observational data are the same of Figure 3.10. A fit to our predicted bias as a function of redshift is given in equation (3.13).

at $z \sim 1.5$, and finally $[-26.44, -23.37]$ at $z \sim 2.0$ (see their Table 1). Note that their value are in b_J , and to convert from B to the b_J -band we used the relation given by these authors in their Appendix 1, where $M_B = M_{b_J} + 0.07$. In the Figure, our points are the black dots, while the numbers quoted by Porciani et al. (2004) are shown with diamonds (the errors quoted by these authors are comparable to the size of the symbol, and therefore are omitted). The agreement is quite good, even though we slightly underestimate the number of bright quasars at $z = 2$, as expected (see the bright-end of the luminosity function at this redshift in Figure 3.3). In Figure 3.9 we also show the number density of our simulated AGN for the same luminosity cuts, but without accounting for obscuration (dotted lines). As described above, we account for obscuration by calculating for each object its probability of being optically visible and then by randomly extracting objects that satisfy the imposed condition. Since this probability is a weak function of luminosity, and since clustering analysis is independent of random sampling, for our study we ignore the effect of obscuration. This allows us to push the analysis to brighter magnitude cuts, since for a statistically-accurate clustering analysis we need at least few hundred objects (the dashed horizontal line shows the point at which, in the full simulation volume, we cannot expect more than 500 objects).

The correlation lengths of the AGN selected with these luminosity cuts are shown in Figure 3.10. We see that at low and intermediate redshifts the correlation length and the bias depend weakly on luminosity when a narrow range of luminosities is examined. Since bright quasars are always powered by BHs accreting close to the Eddington limit, it seems difficult to use quasar clustering observations to disentangle between different light-curve models, unless much larger luminosity ranges are probed. The present observations indicate however that, over the range of luminosities observed, quasars reside in haloes of similar masses. Based on our results, we conclude that the lack of a significant dependence of clustering on luminosity is not primarily a result of invoking light curve models with a wide distribution of Eddington ratios, but rather arises because in a merger-driven scenario there is a small scatter in the typical halo mass hosting quasars close to their peak luminosity.

In Figure 3.10 we added observational data from several works, to qualitatively compare our results with observations. We stress though that the error bars in these figures are calculated to describe the effect of cosmic variance as described in §3.3.1; since we are here ignoring the effect of obscuration, thus improving our statistic, a direct comparison with the error bars given by observational works is not possible.

Most of the observed quasars have a typical magnitude around $M_{b_J}^*$, Croom et al. (2005), with faint limits that strongly depend on redshift (at very low redshifts surveys can reach fainter magnitudes, whereas at very high redshifts the limiting magnitudes can be higher than M_*). At $z \lesssim 1$ the faintest observed magnitudes are $M_B \approx -22$, going up to ≈ -24 at $z \sim 2 - 3$. Since each observational study uses different magnitude cuts, we can not do a detailed comparison with all the observations available, but overall our results for the values of the correlation length and the bias and their evolution with redshift are in good agreement with the observational results.

We also compared observational data with simulated quasars around L_* , calculated using equation 9 from Hopkins et al. (2007b), and selecting objects with an intrinsic luminosity larger than $L_*/0.5$ dex (which corresponds to a minimum luminosity approximately 1.2 mag fainter than M_*). Our predictions for the correlation length and the bias for L_* objects as a function of redshifts are shown in Figure 3.11, again together with the available observational data. The discrepancies with Shen et al. (2009b) for the correlation length can be due in differences in the calculation of this quantity (as already mentioned, here we do not fix the value of γ). For the bias, we show also

the best fit from Croom et al. (2005) and the prediction of Hopkins et al. (2007a). The latter was probably fitted only up to $z = 3$, thus explaining the turn-over at redshifts above 3 that seems to not be consistent with the trend shown by the observations. A good approximation to our prediction for the bias is given by the fitting function

$$b(z) = 0.42 + 0.04(1 + z) + 0.25(1 + z)^2. \quad (3.13)$$

Quasars with luminosities around L_* are typically objects very close to their peak luminosity, therefore correspond to objects accreting at high Eddington ratios. As mentioned before, we cannot use these results as a sensitive test of our light curve models. However, the good agreement with observations indicates that our merger-triggered BH accretion model predicts a spatial distribution of quasars that is consistent with observations. This is a prediction of a consistent model of the joint evolution of dark matter, galaxies and black holes, evolving Λ CDM initial conditions from high redshift to the present. While the parameters of the semi-analytic model had been tuned to fit the bulk $z = 0$ properties of the BH population and the AGN luminosity function as a function of redshift, information on clustering had not been considered in the construction of the model, and therefore must be regarded as genuine model predictions.

3.4 BHs, Quasars and their dark environment

In this section we explore directly the connection between BHs, quasars and their dark matter environment. As in our simulations the dark matter halo merger trees are the backbone upon which the baryonic component is treated, we can also use them to study the dark environment of our AGN. This in particular allows tests of the validity of the approach typically adopted in the interpretation of observational quasar clustering results (e.g., Porciani et al. 2004; Croom et al. 2005), where the observed quasar bias is compared with the halo bias predicted by analytical halo models (e.g., Mo & White 1996; Sheth & Tormen 1999).

The mass distribution of the haloes hosting AGN of given luminosities, $P(M_{\text{Halo}}|L_{\text{AGN}})$, is shown in Figure 3.12. The AGN are here sub-divided into a faint and a bright sub-sample, depending on their bolometric intrinsic luminosity. The cut in bolometric luminosity is here L_* , calculated in the same way as for §3.3.4. Based on the results on the Eddington ratio distribution (see Figure 3.4) and on the clustering, we expect the distribution of the masses of the haloes hosting bright AGN to be similar both for Mod I and Mod II. The main difference should be in the distribution of haloes hosting faint AGN: in the Eddington-limited model, the faint AGN population is composed of small-mass BHs accreting at Eddington, whereas in the model that includes a long quiescent phase the faint-AGN population at low redshifts includes also quite massive BHs accreting at low Eddington ratios.

In Figure 3.12 we indeed see that for Mod I there is a direct proportionality between the luminosity of the AGN and the mass of the host halo: the brighter the AGN, the larger the BH and the host halo. Instead, for Mod II most of the low-luminosity AGN at low redshifts are hosted by more massive haloes, i.e., massive BHs accreting at low Eddington ratio. In the same figures we also plot the mass distribution of haloes hosting L_* quasars. To get a large enough sample, at any given redshift we included objects in a range of ± 0.5 dex around L_* . The similar behavior of haloes hosting L_* quasars in both models suggests that L_* objects are mainly BHs accreting close to the Eddington limit.

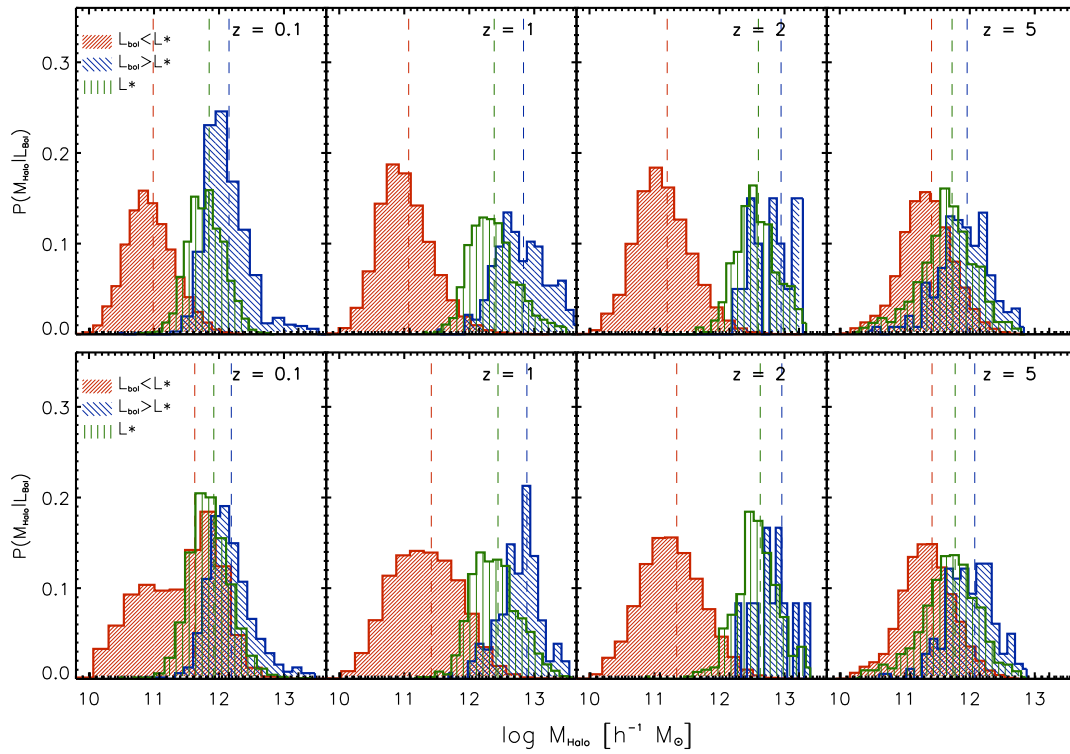


Figure 3.12: Distribution of dark matter halo masses hosting faint-AGN, bright AGN and L_* quasars. The vertical dashed line indicates the median of the distribution for each luminosity bin, and we refer the reader to the legend on the plot for details in the color/pattern-coding. The AGN have been obtained using Mod I (upper panel) of Mod II (lower panel) for the light curve, respectively.

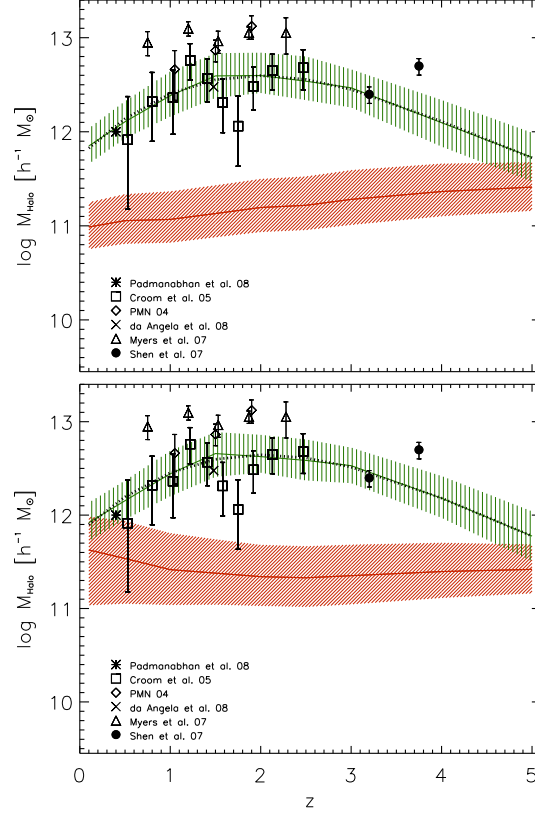


Figure 3.13: In these two panels we show the redshift evolution of the median mass of dark matter haloes hosting AGN of different luminosities from the previous Figure (3.12). For clarity in the plot, we only show the values obtained for objects with $L_{\text{Bol}} < L_*$ and with $L_{\text{Bol}} \sim L_*$. The dotted black curve shows the best fit to the evolution of the typical host mass of L_* quasars. The contours indicate the 25 and 75 percentiles. We overplot here estimates obtained by different groups who examined the clustering properties of observed quasars (see legend on the plots).

The mean values of the distributions are shown as a function of redshift in Figure 3.13. In recent years many groups have analyzed the clustering properties of quasars to estimate the typical mass of their host haloes, at low- (Padmanabhan et al. 2008), intermediate- (Croom et al. 2005; Porciani et al. 2004; da Ângela et al. 2008; Myers et al. 2007a) and high- (Shen et al. 2007) redshifts. These works used quasars observed with SDSS and 2dF, with a typical luminosity around L_* (except for the very high-redshifts measurements). The masses of the dark matter haloes hosting quasars estimated by these groups are overplotted in Figure 3.13. Almost all these estimates are in the range predicted by our model: the typical halo mass hosting L_* quasars seems to grow up to $z \approx 1.5 - 2$, and then it decreases again at higher redshifts. To compactly represent our simulation results, we fitted our results with a cubic function

$$M_{\text{halo}} = a_0 + a_1 z + a_2 z^2 + a_3 z^3, \quad (3.14)$$

with $a_i = [11.873; 0.944; -0.318; 0.026]$ for the second panel of Figure 3.13 (the values of these coefficients are similar for the fit of the L_* curve of the upper panel, which we omit for brevity).

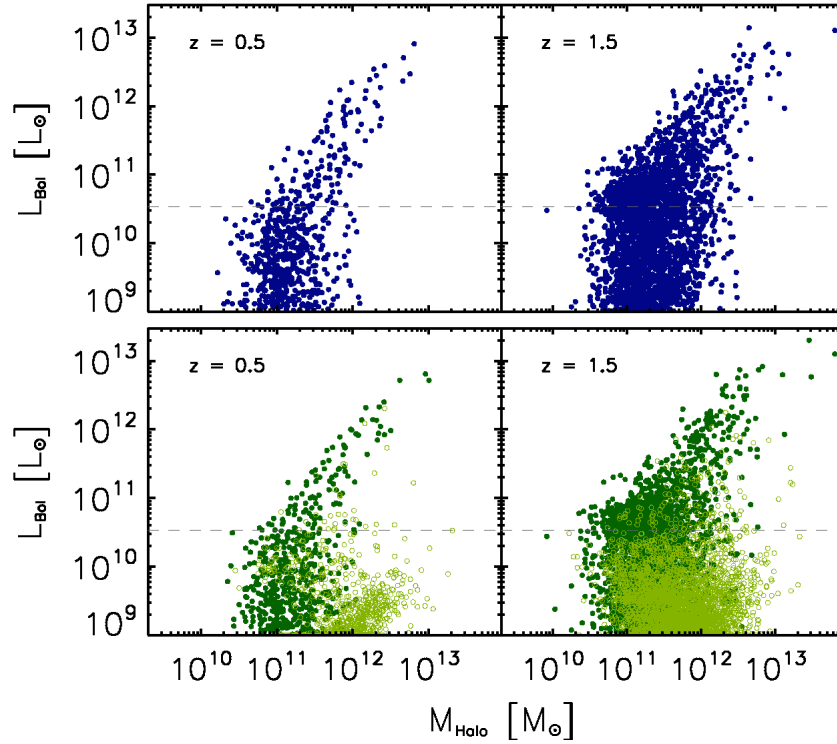


Figure 3.14: Relation of L_{Bol} of the AGN versus dark matter halo mass. In the upper panel, BHs accrete according to the Mod I light curve, while in the lower panel the predictions are produced using Mod II. While all very bright objects are BHs accreting close to the Eddington limit, the main difference between the two models lies in the faint objects, where we have a dense population of faint AGN hosted by large haloes (the light-green open circles in the lower panel refer to AGN in the quiescent phase). For reference, the dashed line marks the Eddington luminosity corresponding to a BH mass of $10^6 M_{\odot}$.

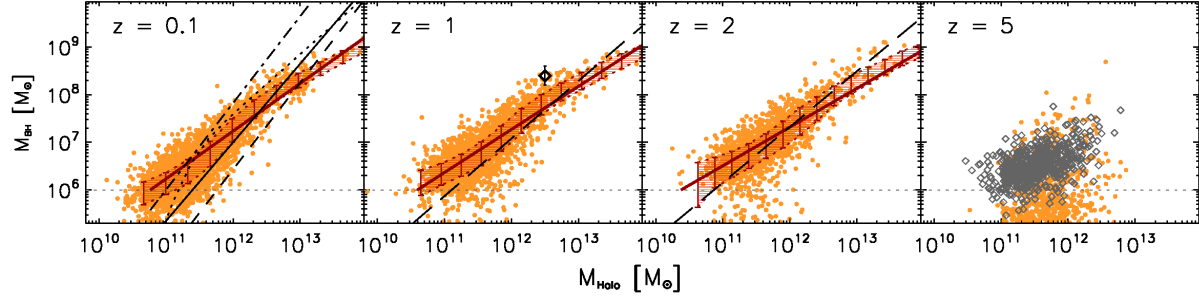


Figure 3.15: $M_{\text{BH}} - M_{\text{Halo}}$ relation for BHs sitting in central galaxies. The points are our simulated objects, and the red line is the best-fit assuming a linear relation. The filled region encloses the 25 and 75 percentiles. For reference, we show at $z = 0.1$ the result that Ferrarese (2002) obtained at $z = 0$ assuming $v_{\text{vir}} = v_c$ (dashed line), $v_c = 1.8v_{\text{vir}}$ (dot-dashed line) and the prescription from Bullock et al. (2001) for this relation (solid line). At $z = 0.1$ we show also the result from Shankar et al. (2006) (dotted curve). The point at $z = 1$ is the zero-point of this relation obtained by Fine et al. (2006). The dashed lines at $z = 1$ and at $z = 2$ are from Colberg & di Matteo (2008) (for $z = 2$ we used their result at $z = 3$). The horizontal dashed line marks $M_{\text{BH}} = 10^6 M_{\odot}$, which is approximately our resolution. This plot was obtained assuming Mod I for the light curve, but the result does not change using Mod II, since the final BH masses are the same. The diamonds at $z = 5$ show the relation between BH mass and halo mass if BHs accreted the available mass instantaneously.

Our results for bright quasars (objects around L_*) are also consistent with the estimates of Lidz et al. (2006) and Hopkins et al. (2007a), who calculate that the typical mass of haloes hosting quasars is $\approx 4 \times 10^{12} h^{-1} M_{\odot}$. These authors argue that bright and faint quasars are the same type of objects but seen in different evolutionary states, and therefore their typical host halo mass should be similar. Since only the brightest quasars are objects accreting at high f_{Edd} , only for these objects we expect a tight relation between the instantaneous luminosity and the host halo mass. The relation between AGN luminosity and halo mass is shown in Figure 3.14. Indeed, only for the very bright quasars there is a direct proportionality between luminosity and halo mass. These are objects that are close to their peak luminosity, have accreted most of the gas available, and at this point their BH is tightly correlated with the mass of the host halo (see also next figure). During the rising phase of the light curve (even if BHs are accreting at Eddington), BHs are not yet strongly correlated with the host halo, reflected in a lack of correlation between quasar luminosity and halo mass. During the decaying phase, Mod II produces a dense population of faint objects sitting in massive haloes (see open circles in Figure 3.14).

White et al. (2008a) claimed that the very high bias observed for high-redshift quasars implies a small dispersion in the above relation. Estimates of high Eddington ratios for bright objects at high redshifts (Kollmeier et al. 2006; Shen et al. 2008) indeed seem to support that for very bright objects a tight relation exists between quasar luminosity and halo mass (Fine et al. 2006). However, we would like to point out that just looking at the bright quasar population it is not sufficient to distinguish between different light curve models.

The observed scaling relations between BH masses and different properties of the host galaxy have suggested the possibility of a more fundamental connection between the mass of the BH and the host system. Using measurements of stellar velocity dispersions and assuming a relation between this quantity and the circular velocity of the galaxy and the BH mass, Ferrarese (2002),

Baes et al. (2003) and Shankar et al. (2006) estimated how the BH mass could be connected to the dark halo mass in the local Universe. At higher redshifts these estimates are of course more problematic, because studies of the stellar kinematics are unavailable and we also are not certain yet how the $M_{\text{BH}} - \sigma$ relation evolves with redshift. Fine et al. (2006) explored the relation between BHs and quasar host haloes at $z = 0.5 - 2.5$ using BH virial masses estimates from the width of broad emission lines and DM halo mass obtained from quasar clustering from Croom et al. (2005). In Figure 3.15, we plot the $M_{\text{BH}} - M_{\text{Halo}}$ relation for our simulated BHs. We include here only BHs residing in central galaxies of FOF haloes. This is because in our model only central galaxies can merge, and therefore it is mainly BHs hosted by FOF haloes that can grow (the results of Li et al. (2006b) indicate that this could be supported by observations). Indeed, we find a well-defined relation which gets tighter with decreasing redshift. In the previous chapter we already showed this relation at redshift $z = 0$ and we found good agreement with other works (Ferrarese 2002; Baes et al. 2003; Shankar et al. 2006). Here we overplot the results of Ferrarese (2002) and Shankar et al. (2006) at $z = 0.1$ for reference; at $z = 1$ we overplot the zero-point in the relation estimated by Fine et al. (2006) ($M_{\text{BH}} = 10^{8.4 \pm 0.2} M_{\odot}$ for a halo of $M_{\text{halo}} = 10^{12.5} M_{\odot}$) and at $z = 1$ and $z = 2$ the results from direct hydrodynamical simulations of Colberg & di Matteo (2008) (for $z = 2$ we used their result at $z = 3$).

Note that the fact that BHs need to accrete most of the available gas before they ‘sit’ on the above relation could be influenced at high redshifts by the resolution limit of the Millennium simulation, which does not resolve low-mass haloes below $\sim 10^{10} h^{-1} M_{\odot}$. We will explore this high-redshift behavior in more details in future work.

3.4.1 Duty cycle

The time BHs spend shining as quasars is still an open question (see the review by Martini 2004). The definition itself of a ‘quasar lifetime’ is somewhat ambiguous. Observationally it is defined as the time BHs spend shining at luminosities higher than some limit (for quasars, the usual definition is the time an active nuclei shines with a B-band magnitude $M_B < -23$ mag). Theoretically, it can be defined in a simpler way as the total time a BH shines at high Eddington ratio. The quasar lifetime is often also simply defined through the duty cycle, which is given by ratio of the quasar number density and the number density of the haloes that can host them: $t_q \sim t_{\text{Hubble}} n_q / n_{\text{Halo}}$ (e.g., Adelberger & Steidel 2005).

Haiman & Hui (2001) and Martini & Weinberg (2001a) suggested to use the observed quasar clustering to estimate the quasar lifetime, upon the assumption that a monotonic relation exists between quasar luminosity and halo mass (see also Haehnelt et al. 1998). Adelberger & Steidel (2005) pointed out that the theoretical estimate of the duty cycle through clustering analysis depends on the Eddington ratio distribution, on obscuration and on the scatter in the relation between quasar luminosity and halo mass. As we have seen, the assumption of a tight relation between luminosity and halo mass is overly simplistic for realistic lifetime models, and it is therefore interesting to use our simulations directly to examine the distribution of quasar lifetimes.

In Figure 3.16 we show the fraction of active haloes (or duty cycle), as a function of quasar luminosity, redshift and halo mass, for both Mod I (left panels) and Mod II (right panels). At high redshifts massive haloes have a very high duty cycle, i.e., most of haloes host a bright quasar. As expected, the duty cycle evolves more strongly with redshift for the more luminous AGN: by redshift $z = 0.1$ only $\approx 0.1\%$ of the more massive haloes host a quasar, and this result is independent on the light curve model assumed. Again, the difference in the two models is in the faint AGN population:

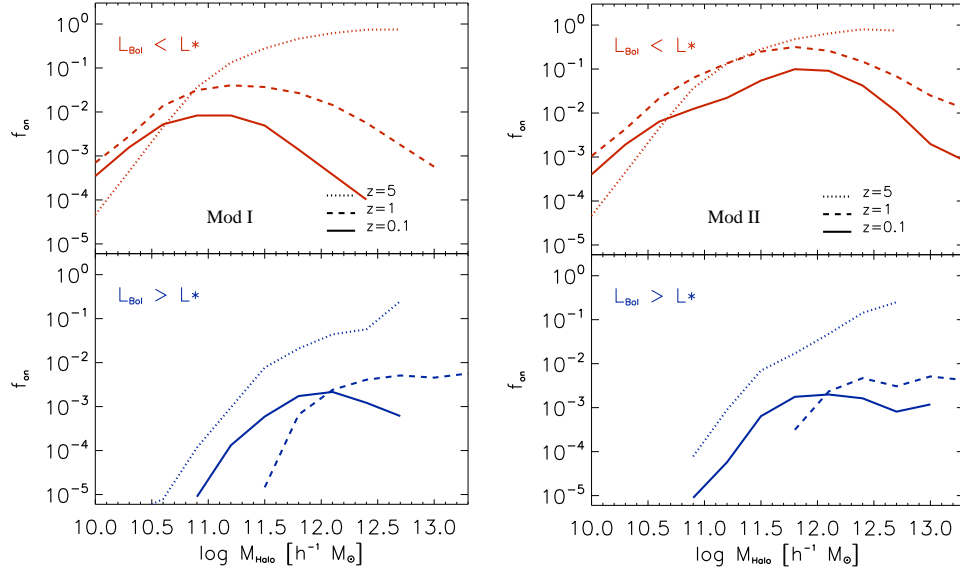


Figure 3.16: *Fraction of active haloes (or duty cycle), as a function of redshift, halo mass and AGN luminosity. We compare the results obtained for Mod I (left panels) and Mod II (right panels).*

the duty cycle of faint objects evolves strongly with redshift and mass for Mod I, since at low redshift only the smallest haloes host an active BH. On the other side, if the AGN light curve includes a long low-level phase, then at low redshift also massive haloes are hosting a low-luminosity object.

Estimates of the quasar lifetime obtained from quasar clustering suggest timescales of the order of $10^7 - 10^8$ yr, depending on the redshift. At high redshifts ($z \geq 3.5$), Shen et al. (2007) estimated lifetimes of the order of $30 \sim 600$ Myr, while at $2.9 \leq z < 3.5$ the estimated range decreases to $4 \sim 50$ Myr. Porciani et al. (2004) suggest $t_q \sim 10^7$ yr at $z \sim 1$, and values approaching 10^8 yr at higher redshifts. As we approach low redshifts and the local Universe, the quasar lifetimes seem to decrease: Padmanabhan et al. (2008) suggest values $< 10^7$ yr for their sample of quasars at $0.2 < z < 0.6$. As we have shown in Figure 3.16, a strong evolution of the quasar lifetime is also expected from our models: at intermediate-high redshifts our results are compatible with lifetimes of a few 10^8 yr, but the detailed evolution of the duty cycle also depends strongly on the range of host halo mass considered.

3.5 Summary of the chapter

In this chapter, we used the spatial distribution of active BHs as a further test of our model for BH accretion described in the previous chapter, and that has its foundations on the assumption that galaxy mergers are the primary physical mechanism responsible for efficiently feeding central BHs.

Throughout the chapter, we compared the results obtained adopting two different theoretical models for the quasar lifetime: pure Eddington-limited accretion (Mod I), and a model in which Eddington-limited accretion is followed by a long, weak accretion phase (Mod II), modeled after Hopkins et al. (2005). The main difference between the predictions of the two models is in the faint-end of the luminosity function. The long low-luminosity accretion phase allowed by Mod II gives rise to a large population of massive BHs that at low redshifts are accreting at low Eddington

ratios, in agreement with the observational results of, for example, Heckman et al. (2004) and Netzer & Trakhtenbrot (2007), who found that in the local Universe only BHs with mass $\lesssim 10^7 M_\odot$ are experiencing high-efficient accretion. As also recently pointed out by Hopkins & Hernquist (2008), it is only by studying the properties of the faint AGN population that the quiescent phase described by Hopkins et al. (2005) can be tested.

Independent of the model adopted for the light curve, the two-point correlation function of our simulated AGN can be approximated by a single power-law in the range $0.5 \lesssim r \lesssim 20 h^{-1} \text{Mpc}$. The bias between AGN and the dark matter is a strong function of redshift, but, at a given epoch, it is approximately constant in the range $1.0 \lesssim r \lesssim 20 h^{-1} \text{Mpc}$. As expected, the correlation lengths of AGN obtained with Mod I or Mod II differ only for the faint population: the correlation length of faint AGN obtained with Mod II is consistent with the correlation length of $10^{12} - 10^{13} h^{-1} M_\odot$ haloes, whereas faint AGN obtained with Mod I exhibit the same clustering as $10^{11} - 10^{12} h^{-1} M_\odot$ haloes.

Recent results from optical quasar surveys like SDSS and 2dFQSO have not found evidence for a strong dependence of clustering on luminosity (Porciani et al. 2004; Croom et al. 2005; Myers et al. 2007a; da Ângela et al. 2008, e.g.), except for Shen et al. (2009b) who detect an excess of clustering for their 10% brightest quasars. Our results are consistent with these observations if we consider only quasars with an intrinsic luminosity within the range probed by these surveys. However, if we compare the clustering properties of AGN over a very extended range of luminosity, then the correlation length becomes a moderately strong function of luminosity and the value of the correlation length of the faint population in particular is seen to depend on the light curve model assumed. The fact that the clustering of the observed quasars does not depend on luminosity could be explained in two ways: quasars of different luminosities are powered by BHs of the same mass that are in different stages of their evolution, and/or the typical mass of haloes hosting quasars is approximately constant for the luminosity range probed by observations. From our results the second hypothesis seems to be clearly favoured. The mass range of haloes hosting L_* quasars is narrow enough that a significant luminosity dependence of clustering cannot be detected with the current observational samples, independent of the light curve model.

We also directly compared the clustering of our L_* quasars with the most recent observational data, and found very good agreement. Since quasars at these luminosities are objects very close to their peak luminosity, and therefore correspond to objects accreting at high Eddington ratios, we cannot, however, use these results as a sensitive test of our light curve models. Nevertheless, the good agreement with observations indicates that our merger-triggered BH accretion model predicts a spatial distribution of quasar that is consistent with observations. This non-trivial outcome can be viewed as a further success of the hierarchical galaxy formation paradigm, and the cold dark matter hypothesis.

We note that a similar result for the luminosity dependence of AGN clustering has been found in Marulli et al. (2009), who analyzed mock AGN Chandra catalogues constructed with the same semi-analytic model adopted in this work. Furthermore, Thacker et al. (2009) have recently found very similar results modeling the AGN spatial properties in an hydrodynamical simulation.

In future work we will compare the merger-triggered quasar model with alternative suggestions for the physical triggering mechanism of quasar activity, such as disk-instabilities occurring in isolated galaxies. We expect that quasar clustering statistics can here be a potentially powerful discriminant to further constrain the viable physical models for the evolution of supermassive black holes, and their co-evolution with galaxies.

Chapter 4

The *merger bias*

In the work presented in this chapter¹, we use the large catalogues of haloes available for the Millennium Simulation to test whether recently merged haloes exhibit stronger large-scale clustering than other haloes of the same mass. This effect could help to understand the very strong clustering of quasars at high redshift. However, we do not find statistically significant excess bias for recently merged haloes over the redshift range $2 \leq z \leq 5$, with the most massive haloes showing an excess of at most $\sim 5\%$. We also consider galaxies extracted from a semi-analytic model built on the Millennium Simulation. At fixed stellar mass, we find an excess bias of $\sim 20 - 30\%$ for recently merged objects, decreasing with increasing stellar mass. The fact that recently-merged galaxies are found in systematically more massive subhaloes than other galaxies of the same stellar mass accounts for about half of this signal, and perhaps more for high-mass galaxies. The weak merger bias of massive systems suggests that objects of merger-driven nature do not cluster significantly differently than other objects of the same characteristic mass over the range $5 < r < 25 h^{-1}$ Mpc. In §4.1 we introduce the problematic discussed in this chapter. In §4.2 we briefly describe the simulation and how we identify recent mergers both of haloes and galaxies. In §4.3 we show results for the merger bias both of haloes and of galaxies, and in §4.4 we discuss the implications of our results for the clustering of quasars. A summary and conclusions for the chapter are presented in §4.5.

4.1 Introduction

In the last decade, much theoretical work has tried to constrain the cosmological evolution of supermassive black holes (BHs) by simultaneously interpreting the statistics of quasars/BHs and their clustering as a function of redshift and luminosity (e.g., Kauffmann & Haehnelt 2002; Wyithe & Loeb 2005; Lidz et al. 2006; Hopkins et al. 2007a; Thacker et al. 2009; Bonoli et al. 2009; Shankar et al. 2008, 2009b). In fact, if quasars are hosted by haloes whose bias is only mass-dependent, clustering measurements can be used to infer the mass M_{Halo} of the host dark matter halo, which in turn provides host number densities, quasar duty cycles (here defined as the ratio between quasar and halo number densities) and scatter in the relation between quasar luminosity L and halo mass (Cole & Kaiser 1989; Haehnelt et al. 1998; Martini & Weinberg 2001a; Haiman & Hui 2001). Measuring a high bias implies high halo masses, low host number densities, high duty

¹This chapter follows the paper *On merger bias and the clustering of quasars* by Silvia Bonoli, Francesco Shankar, Simon D.M. White, Volker Springel and J. Stuart B. Wyithe (MNRAS, in press).

cycles, and vice versa. At fixed duty cycle, increasing the scatter in the mean $L - M_{\text{Halo}}$ relation implies increasing the contribution of less massive and less biased haloes to the same luminosity bin, thus lowering the overall bias.

In §1.3.3 we summarized the observational results on quasar clustering mainly based on the large SDSS and the 2dFQSO surveys (York et al. 2000; Croom et al. 2004), which have allowed a detailed investigation of the clustering properties of accreting BHs from the local Universe up to $z \sim 5$ (e.g., Porciani et al. 2004; Croom et al. 2005; Shen et al. 2007; Myers et al. 2007a; Coil et al. 2007; da Ângela et al. 2008; Padmanabhan et al. 2009; Ross et al. 2009). Assuming that haloes hosting quasars are typical in the way they trace the dark matter density field, these studies concluded that quasars reside at all times in a relatively narrow range of halo masses, $M_{\text{Halo}} \sim 3 \times 10^{12} - 10^{13} h^{-1} M_{\odot}$.

Interestingly, the very high clustering amplitude of luminous quasars at $z > 3$ measured with the SDSS (Shen et al. 2007), has posed some nagging theoretical problems for the simultaneous interpretation of the clustering and the luminosity function at these epochs. The high clustering appears to imply that the quasars live in very massive haloes. But the extreme rareness of such haloes is difficult to reconcile with the observed quasar luminosity function, especially at $z \sim 4$, unless a high quasar duty cycle and a very low scatter in the $L - M_{\text{Halo}}$ relation are assumed (White et al. 2008b). Moreover, matching the high $z \gtrsim 3 - 4$ quasar emissivity to the low number density of hosts constrains the ratio of the radiative efficiency of accretion ϵ to the Eddington ratio f_{Edd} to be $\epsilon > 0.7 f_{\text{Edd}} / (1 + 0.7 f_{\text{Edd}})$, implying $\epsilon > 0.17$ for $f_{\text{Edd}} > 0.25$ (Shankar et al. 2008), which are rather extreme values. However, these conclusions can be relaxed if quasar hosts cluster more strongly than typical haloes of similar mass (Wyithe & Loeb 2009). This would then imply that quasars live in less massive but more numerous haloes, allowing for lower duty cycles and less extreme values for ϵ .

Several analytical and numerical studies have investigated whether haloes of similar mass have different large-scale clustering properties, depending, in a non-trivial way, on their growth history, concentration, spin, or environment (e.g., Kolatt et al. 1999; Lemson & Kauffmann 1999; Kauffmann & Haehnelt 2002; Gao et al. 2005; Wechsler et al. 2006; Gao & White 2007; Angulo et al. 2008). In particular, Wyithe & Loeb (2009) suggest that the possible merger-driven nature of quasars might cause an excess bias, if the large-scale clustering of recently-merged haloes is higher than expected for typical haloes of the same mass (“merger bias”). This suggestion was based on the model by Furlanetto & Kamionkowski (2006), who analytically calculated that close merging pairs might possess a merger bias of a factor of $\gtrsim 1.5$.

Recent work has indeed shown that clustering strength depends not only on halo mass, but also on other parameters. Gao et al. (2005) found that later forming haloes with mass $M < M_*$ (where M_* is the mass for which $\sigma(M_*) = 1.69/D(z)$) are less clustered than typical haloes of the same mass (“assembly bias”). Wechsler et al. (2006) extended this study to show that less concentrated haloes more massive than the non-linear mass scale are instead more biased than average. Li et al. (2008) explored various definitions of halo formation time, and concluded that the dependence of clustering on halo history depends strongly on the precise aspect of the history that is probed: while they confirmed previous results on assembly bias, they did not find any dependence of clustering on the time of the last major merger. Other numerical work that specifically looked at merger bias found inconclusive results, probably due to the different ranges of masses, redshifts and scales used and the poor statistics available (Gottlöber et al. 2002; Percival et al. 2003; Scannapieco & Thacker 2003). Wetzell et al. (2007) used a large dark matter simulation to study the clustering of very massive haloes ($M_{\text{Halo}} > 5.0 \times 10^{13} h^{-1} M_{\odot}$), and found that, at redshift $z \lesssim 1$, merger remnants

show an excess bias of $\sim 5 - 10\%$.

In the next sections, we make use of the large, publicly available catalogues of the Millennium Simulation (Springel et al. 2005c) to explore for a wider range of masses the level of excess bias for high redshift merger remnants.

4.2 Identifying merging haloes and galaxies in the Millennium Simulation

4.2.1 The Millennium Simulation and its galaxy population

As already described in §2.2 the Millennium Simulation (Springel et al. 2005c) is an N-body simulation which follows the cosmological evolution of $2160^3 \simeq 10^{10}$ dark matter particles, each with mass $\sim 8.6 \times 10^8 h^{-1} M_\odot$, in a periodic box of $500 h^{-1} \text{Mpc}$ on a side. The cosmological parameters used in the simulation are consistent with the WMAP1 & 2dFGRS ‘concordance’ Λ CDM framework: $\Omega_m = 0.25$, $\Omega_\Lambda = 0.75$, $\sigma_8 = 0.9$, Hubble parameter $h = H_0/100 \text{ kms}^{-1} \text{Mpc}^{-1} = 0.73$ and primordial spectral index $n = 1$ (Spergel et al. 2003). In this chapter we focus on the clustering of galaxies and haloes from $z = 2$ to $z = 5$, where the time between two simulation outputs varies from approximately 200 Myr to 100 Myr. This time resolution is good enough to capture merger events reliably and in these time intervals any change in the large-scale distribution of merger remnants is negligible.

Detailed merger trees were constructed for the simulation by identifying haloes and subhaloes with, respectively, a friends-of-friends (FOF) group-finder and an extended version of the SUBFIND algorithm (Springel et al. 2001a): particles are included in the same FOF group if their mutual separation is less than 0.2 of the mean particle separation. The SUBFIND algorithm then identifies locally overdense and self-bound particle structures within FOF groups to isolate bound subhaloes (which are required to contain a minimum of 20 particles). For further details on the Millennium Simulation and the tree building procedure we refer the reader to Springel et al. (2005c).

The formation and evolution of galaxies has been followed in a post-processing simulation which uses the dark matter merger trees as basic input combined with analytical treatments of the most important baryonic physics in galaxy formation, including the growth of central BHs (see chapter 2). This has produced remarkably successful galaxy formation models which reproduce a large set of observational findings about the local and high redshift galaxy populations with good accuracy. While not perfect, this match justifies substantial trust in the basic paradigm of hierarchical galaxy formation in CDM cosmologies, and motivates detailed studies of the merger and clustering statistics using the Millennium Simulation. Below we describe our definition of major mergers both for dark matter haloes and galaxies, which lies at the heart of our investigation of the merger bias phenomenon.

4.2.2 Halo mergers

We note that different definitions of halo formation time have led to somewhat different quantitative conclusions regarding the effect of assembly history on the large-scale clustering of haloes (e.g., Gao et al. 2005; Wechsler et al. 2006; Li et al. 2008). Here we are interested in the possible bias caused by recent merger activity, which might induce a non-trivial relation between the clustering of dark matter haloes and objects whose formation is triggered by mergers (such as quasars). We are therefore not interested in tracking the full mass accretion history of dark matter haloes, but rather

want to focus on the violent major merger events that are thought to trigger efficient BH accretion and starburst activity.

In the present work, we consider as *major mergers* those events in which two separate haloes with comparable masses encounter each other for the first time, that is, when they join the same FOF group. At a given time z_n , we define as recently merged haloes those that, at the previous snapshot z_{n-1} , have two or more progenitors belonging to separate FOF groups whose mass (defined through the number of particles of the FOF group) was $> 20\%$ that of the descendant (corresponding to a minimum ratio $m_{\text{sat}} : m_{\text{central}} = 1 : 4$). This choice of mass ratio is motivated by results of simulations of galaxy mergers: for example, Younger et al. (2008) found that, for mergers above the 1 : 4 threshold, galactic discs are completely destroyed and black holes efficiently fed. In any case, we checked that adopting a different threshold does not change our conclusions. Our definition of a major merger is similar to the one of Scannapieco & Thacker (2003), who defined as merger remnants haloes that, within the time interval of a single snapshot, accreted at least 20% of their final mass. These authors, however, also considered haloes that experienced considerable smooth mass accretion, whereas we strictly require the merger remnant to be the product of the encounter of two sufficiently massive FOF progenitors. We note that Wetzel et al. (2007) used different definitions of halo merger, finding their results depend on the value of the mass ratio, but they seem to be independent of the precise definition of halo merger.

In our definition of major mergers we also include encounters of groups that at some later time might split again. This can occasionally happen since the FOF algorithm sometimes links two haloes that are just passing close to each other but that in the future will (at least temporarily) separate again. To check whether this might impact our overall results, we also used the merger trees extracted from the Millennium Simulation by Genel et al. (2009), who carefully excluded all mergers of FOF groups containing subhaloes that at a future time will belong to two different FOF groups. Moreover, Genel et al. (2009) define as halo mass the sum of just the gravitationally bound particles. We checked, however, that our results do not change when switching to the Genel et al. (2009) halo trees. The differences from our reference catalogues affect the halo population only at very low redshifts and at low halo masses, much below the ranges of interest here.

We have also checked that our definition of halo mass based on the number of linked particles instead of a spherical overdensity mass estimate does not affect our result. As an alternative to the FOF group masses, we used as group masses the mass within the radius that encloses a mean overdensity of 200 times the critical density, or the mass within the radius where the overdensity is that expected for virialization in the generalized top-hat collapse model for our cosmology. However, we found that this did not lead to any significant differences in the large-scale clustering properties of haloes as a function of mass.

4.2.3 Galaxy mergers

In the Millennium Simulation, the orbits of dark matter subhaloes are followed until tidal truncation and stripping due to encounters with larger objects cause them to fall below the simulation resolution limit (20 particles, equivalent to a mass of $\sim 1.7 \times 10^{10} h^{-1} M_{\odot}$). Galaxies follow the orbits of their host subhalo until this point, and then their remaining survival time as satellite galaxies is estimated using their current orbit and the dynamical friction formula of Binney & Tremaine (1987), calibrated as in De Lucia & Blaizot (2007). At the end of this interval, a satellite galaxy is assumed to merge with the central galaxy of the host dark matter halo, which can either be a subhalo or, more frequently, the main halo of the associated FOF group (Angulo et al. 2009).

In the event of a minor galaxy merger, the cold gas of the satellite galaxy is transferred to the disc component of the central galaxy together with the stars produced in a starburst (as described below); moreover, the bulge of the central galaxy grows by incorporating all the stars of the satellite. If instead a major galaxy merger has occurred, the discs of both progenitors are destroyed and all stars in the merger remnant are gathered into the spheroidal bulge component. In the galaxy formation model studied here, the starbursts induced by galaxy mergers are described using the ‘‘collisional starburst’’ prescription introduced by Somerville et al. (2001): the fraction e_{burst} of cold gas which is converted into stars in the merger remnant is given by: $e_{\text{burst}} = \beta_{\text{burst}}(m_{\text{sat}}/m_{\text{central}})^{\alpha_{\text{burst}}}$, where $\alpha_{\text{burst}} = 0.7$ and $\beta_{\text{burst}} = 0.56$, chosen to provide a good fit to the numerical results of Cox et al. (2004).

We define as major merger remnants those galaxies that have, in the immediately preceding simulation output, two progenitors with stellar masses larger than 20% of the stellar component of the descendant (as for the FOF haloes, this imposes a minimum mass ratio $m_{\text{sat}} : m_{\text{central}} = 1 : 4$). Note that this definition is close, but not identical, to the distinction between minor/major mergers adopted in the underlying galaxy formation model.

4.3 Results

4.3.1 Clustering analysis and the excess bias F

We refer to Appendix B for the definition of the correlation function and the bias. But, since the number density of merging objects at a given snapshot is too low for a statistically significant auto-correlation study (see §4.4), we adopt a cross-correlation analysis instead. In this case the bias is given by

$$b_{H,DM}(r) \equiv \frac{1}{b_{R,DM}(r)} \frac{\xi_{H,R}(r)}{\xi_{DM}(r)}, \quad (4.1)$$

where $b_{R,DM}(r)$ is the bias (relative to the dark matter) of the population we are using as reference in our cross-correlation analysis, and $\xi_{H,R}(r)$ is the cross-correlation function between the haloes and the reference population. By definition, the bias is a function of scale. However, the scale dependence becomes weak or even vanishes at large scales. Since we are here interested in the behavior of the merger bias at very large scales, we estimate the bias on these scales by finding the best constant value over the range $5 < r < 25 h^{-1}$ Mpc. This adds robustness to our results by reducing noise from counting statistics.

We can define the merger bias as the excess in the clustering of merger remnants at large scales with respect to the global population of objects selected with similar properties:

$$F(r) = \xi_{M,R}(r)/\xi_{H,R}(r), \quad (4.2)$$

where $\xi_{M,R}$ is the cross-correlation between merger remnants and the reference sample, and $\xi_{H,R}$ is the cross-correlation between the global population and the reference sample.

We estimate errors for our measurements using the bootstrap method, generating for each sample 50 bootstrapped samples of the same size, drawn at random from the parent sample and allowing for repetitions (the error estimates converge already when using just a few dozen bootstrap samples). For each bootstrap sample, we calculate the correlation functions, the bias and the excess bias. The standard deviation among these quantities is then taken as error estimate. Recently, Norberg et al. (2009) pointed out that the variance on the two-point correlation function is overestimated when

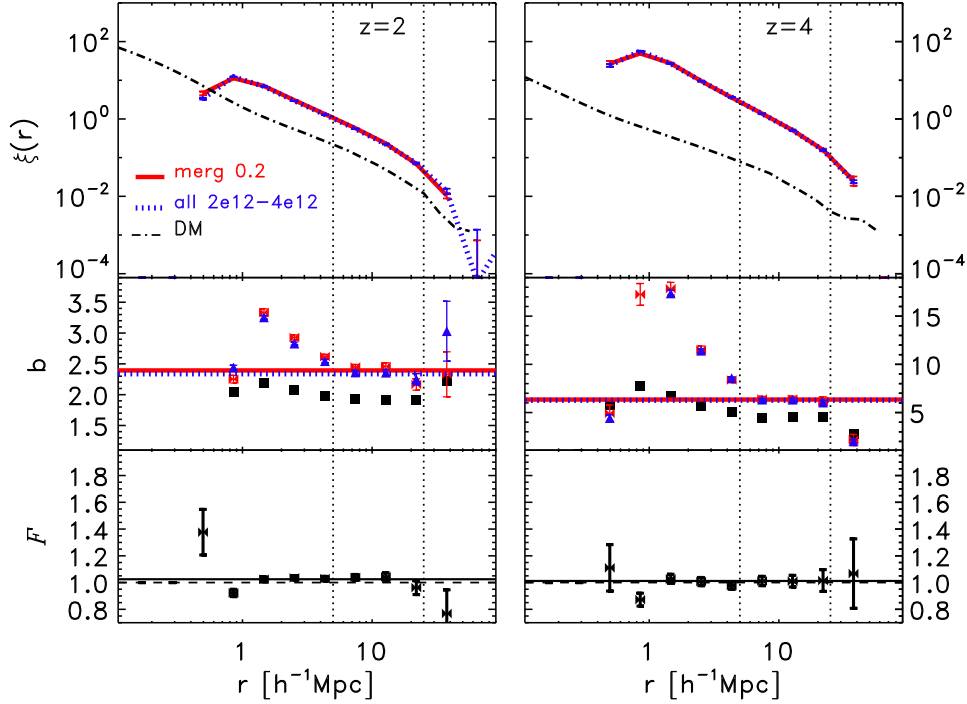


Figure 4.1: Upper panels: Examples of the two-point cross-correlation function at $z = 2$ and $z = 4$ (left and right, respectively) between the reference sample and the haloes with mass in the range $2.0 < M_{\text{Halo}} < 4.0 \times 10^{12} h^{-1} M_{\odot}$ (blue-dotted lines), and between the reference sample and the subsample of recently merged haloes (red lines). The auto-correlation of the underlying dark matter is shown as dot-dashed line. Middle panels: Bias as a function of scale for all the haloes in the mass bin (blue triangles), for the corresponding merger remnants (red bow-ties) and for the reference sample (black squares). The horizontal lines indicate the fit to the points, over the range indicated by the vertical dotted lines. Lower panels: Excess bias F for the merger remnants relative to the whole halo population as a function of scale. The horizontal dashed line indicates $F = 1$. We refer the reader to the text for details of the calculation of errors and the fitting procedure.

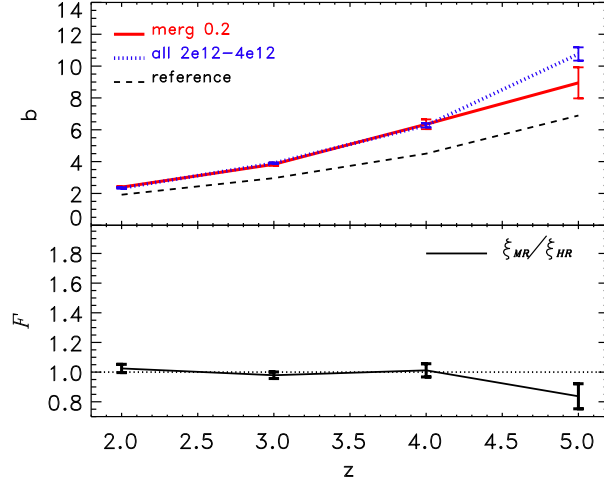


Figure 4.2: Bias and F parameter as a function of redshift, from the best fit obtained for the halo samples shown in Figure 4.1.

calculated with bootstrap techniques. Keeping this in mind, we deliberately choose the bootstrap method in order to be conservative in our error estimates. Another option would have been to estimate errors by subdividing the whole Millennium volume into subvolumes (for example eight octants) and then to calculate the variance of the $\xi(r)$ measured within individual subvolumes. This method becomes inaccurate at large scales (few tens of Mpc) due to the smaller volume probed by each subvolume.

4.3.2 The merger bias for DM haloes

In our study of the merger bias for haloes we proceed as follows:

- We take all FOF haloes with mass in the range $5 \times 10^{11} < M_{\text{Halo}} < 1.6 \times 10^{13} h^{-1} M_{\odot}$. For the redshifts analyzed in this work, this mass range is well above the collapsing mass M_* , defined by: $\sigma(M_*) = 1.69$ (at $z = 2$, $M_* \sim 1.3 \times 10^{10} h^{-1} M_{\odot}$). This entire sample is used as reference sample for the cross-correlation analysis. It is large enough that the error on its auto-correlation can be safely neglected with respect to other sources of error in the b and F parameters (it is composed of $\sim 3.5 \times 10^4$ haloes at $z = 5$ up to $\sim 5.5 \times 10^5$ at $z = 2$).
- We subdivide this sample into five mass-bins, with constant logarithmic spacing $\Delta \log M_{\text{Halo}} = 0.3$ (a factor of two in mass). We will refer to these five samples as H_i .
- We then checked which haloes in each of the bins of H_i had a recent major merger, as described in §4.2.2. The subsamples of recently-merged objects are denoted by M_i . The fraction of merger remnants is $\sim 10\%$ at $z = 2$, and increases to $15 - 20\%$ at $z = 5$. The mass bins are narrow enough that, within each bin, the merger remnants and the parent population have effectively the same distribution of masses.

For the bootstrap error calculation, we created 50 samples from each of the H_i halo samples, and from these new samples we extracted the corresponding catalogues of the recently-merged haloes.

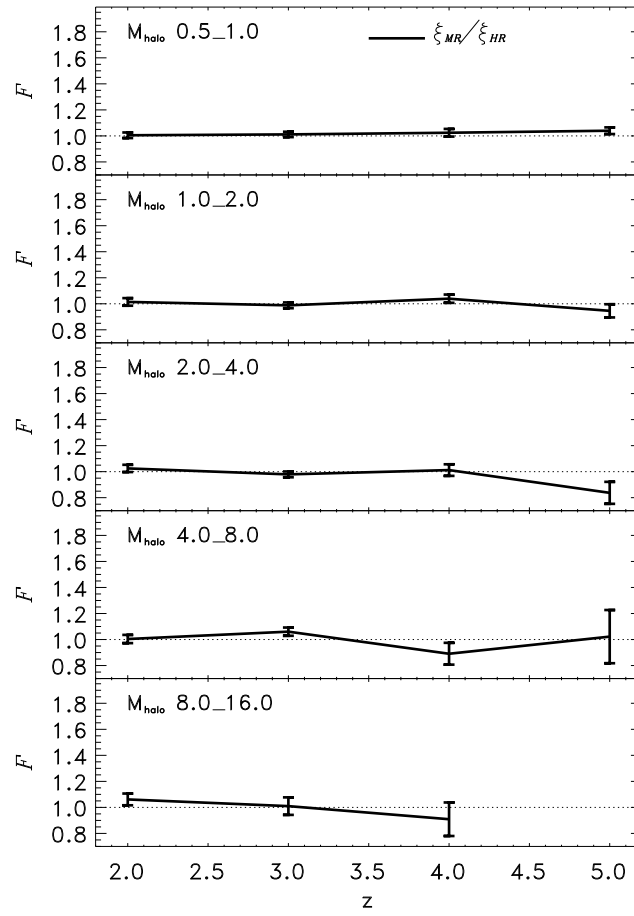


Figure 4.3: Excess bias for DM haloes in separate mass bins, as indicated in each panel in units of $10^{12} h^{-1} M_{\odot}$.

If $\xi_{M_i,R}$ is the cross correlation between the merger remnants and the reference sample, and $\xi_{H_i,R}$ is the cross correlation between all the haloes in the bin and the reference sample, the excess bias parameter is given by $F = \xi_{M_i,R}/\xi_{H_i,R}$. One of our principal aims is to quantify how much F deviates from unity.

In Figure 4.1, we show at two different redshifts an example of the two-point cross-correlation function, the bias and the F parameter for haloes with masses in the range $2.0 < M_{\text{Halo}} < 4.0 \times 10^{12} h^{-1} M_{\odot}$. In the top panels, the red and blue curves are the cross-correlation functions between the reference sample and the merger and parent halo samples, respectively. The error bars show the 1σ dispersion of the bootstrap samples. The correlation power drops at small scales as expected for FOF haloes (by definition, two haloes cannot be closer than twice their virial radius, hence the “1-halo” term, i.e., the contribution to the correlation function from subhaloes within the virial radius, is missing). In the middle panels, we show at each scale the bias of the merger sample, of the parent sample and of the reference sample (red bow-ties, blue triangles and black squares, respectively); in the lower panels the excess bias $F = \xi_{M_i,R}/\xi_{H_i,R}$ is also shown as a function of scale. The errors on each point on b (and F) are from the 1σ dispersion of the bias (F) calculated for each bootstrap sample. Both for b and F the horizontal lines show the best constant fits to the points in the range $5 < r < 25 h^{-1}\text{Mpc}$.

The resulting fits for the bias and F as a function of redshift are shown in Figure 4.2. The errors on these fits are given by the 1σ dispersion of the fits calculated for each bootstrap sample. The excess bias F corresponding to each halo mass bin considered is shown in Figure 4.3. If at a given snapshot there are less than 10 mergers, we do not show the result, since the corresponding cross-correlation function would be too noisy. That is why for the higher mass-bins (lower panels) the results are not shown at all redshifts.

In these results, we do not find any statistically significant merger bias, over the full redshift range probed in our analysis. Only in the most massive bins (lower panels), we see a small deviation of the F from unity, which is at most at the $\lesssim 5\%$ level for the smallest redshift. At high redshifts, we also see a small bias deficit, but the larger error bars prevent us from making firm conclusions on this deficit. We stress that switching to the Genel et al. (2009) catalogs or changing our mass definition, as well as adopting a higher mass ratio, does not alter the results presented in the Figures discussed above.

4.3.3 The merger bias for galaxies

We investigated the merger bias of galaxies with a procedure similar to the one adopted above for dark matter haloes. All the galaxies with stellar mass in the range $5 \times 10^9 < M_{\text{star}} < 1.6 \times 10^{11} h^{-1} M_{\odot}$ have been divided into five mass bins, G_i , and from each bin we extracted subsamples of recently-merged galaxies M_i , obtained as described in §4.2.3. We use as reference sample the entire galaxy population in this range ($5 \times 10^9 < M_{\text{star}} < 1.6 \times 10^{11} h^{-1} M_{\odot}$, which is composed of $\sim 10^5$ galaxies at $z = 5$ up to $\sim 1.4 \times 10^6$ at $z = 2$). This sample is again large enough that the error on its auto-correlation can be safely neglected.

In Figure 4.4, we show an example of the two-point cross-correlation function for the intermediate mass bin. We refer to the description of Figure 4.1 for details on the derivation of the bias b and the excess bias F . Unlike for FOF groups, where it only makes sense to consider the clustering properties on large scales, for the galaxies we can compute the correlation function down to very small scales $\sim 0.01 h^{-1}\text{Mpc}$, allowing for a rather accurate description of the 1-halo term as well, at least at $z < 4$. We find that while F at large scales is approximately constant, it steadily

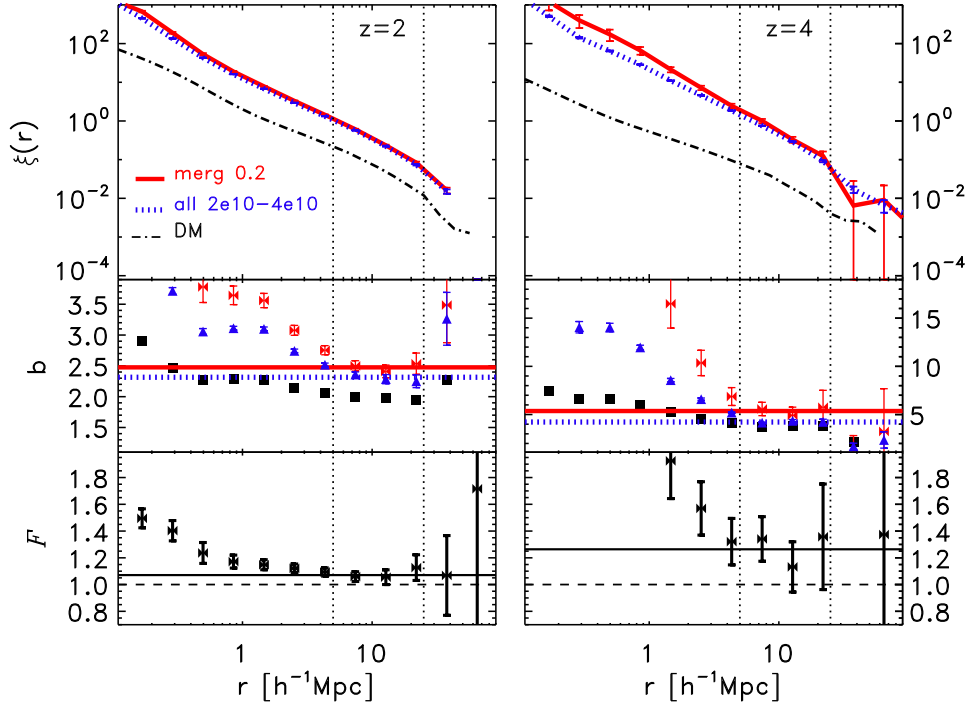


Figure 4.4: *Upper panels: Examples of the two-point cross-correlation function at $z = 2$ and $z = 4$ (as labeled) between the reference sample and galaxies with stellar mass in the range $2.0 < M_{\text{star}} < 4.0 \times 10^{10} h^{-1}M_{\odot}$ (blue-dotted lines), and between the reference sample and the sub-sample of similar mass merger remnants (red lines). The auto-correlation of the underlying dark matter is shown as dot-dashed line. Middle panels: Bias as a function of scale for all the galaxies in the mass bin (blue triangles), for the corresponding merged galaxies (red bow-ties), and for the reference sample (black squares). The horizontal lines show fits to the points, over the range indicated by the vertical dotted lines. Lower panels: Excess bias F for the merged galaxies relative to the whole galaxy population as a function of scale. The horizontal dashed line indicates an absence of excess bias (i.e., $F = 1$). We refer the reader to the text for details of the calculation of errors and the fitting procedure.*

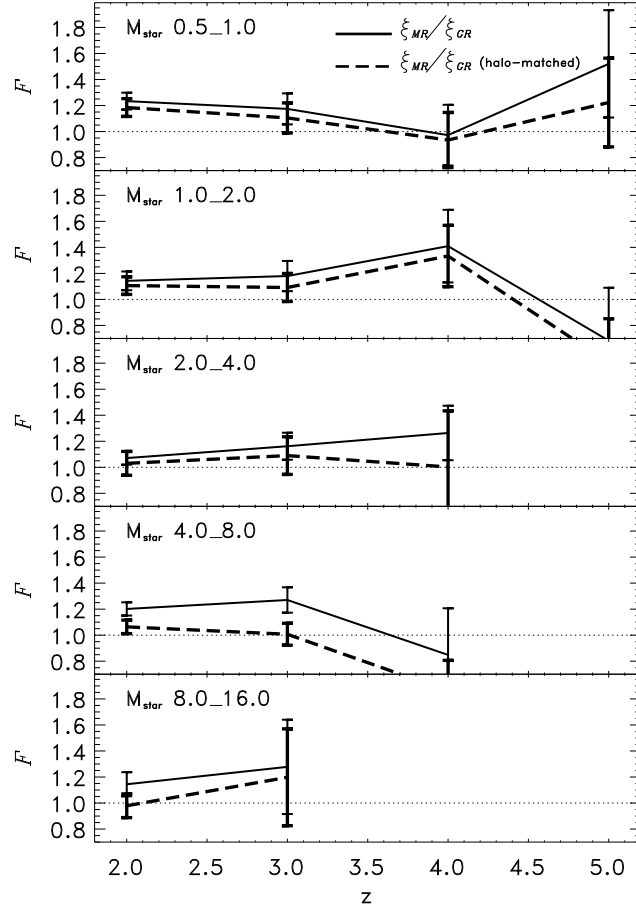


Figure 4.5: Excess bias between merger remnants and the parent galaxy population (solid lines), for different stellar mass bins (the mass range is indicated in the upper-left corner of each panel in units of $10^{10}h^{-1}M_{\odot}$). The dashed lines show the excess bias after matching the distribution of host subhalo masses. No excess bias is present if $F = 1$ (thin dotted line).

increases at the smallest scales probed by our study. The detection of a steady increase of the excess bias F with decreasing scale might be of potential interest. Observationally, there are some indication of a rise in the quasar clustering at small scales (Serber et al. 2006; Hennawi et al. 2006, 2009; Myers et al. 2007b, 2008; Shen et al. 2009a), and other theoretical works have also found such an excess for recently merged subhaloes (Thacker et al. 2006; Wetzel et al. 2009). Indeed, a detailed comparison between model predictions and the observed small-scale clustering of quasars at different redshift and luminosity thresholds could also provide insights on the merger-driven nature of quasars, and we postpone a more careful analysis of this subject to future work.

The excess bias F fitted on scales larger than $5 h^{-1}\text{Mpc}$ is plotted as a function of stellar mass and redshift in Figure 4.5 (solid lines). Excess bias of size 20 – 30% ($F \sim 1.2 - 1.3$) is clearly present for all mass bins and at all redshifts, despite the large error bars at the highest redshifts. In essence, we find that, at fixed stellar mass, recently merged galaxies are more strongly clustered on large scales.

We also examined the mass-distribution of the dark matter subhaloes hosting the galaxies

considered in this analysis. For galaxies that sit in the main halo of a FOF group, this mass is given by the virial mass of the group (defined as the mass within the radius that encloses a mean overdensity of 200 times the critical density of the simulation), whereas for galaxies that are located in substructures, the parent halo mass is defined simply as the number of particles bound to the substructure (as determined by the SUBFIND algorithm). We found that, for each galaxy bin, the distribution of masses of the host subhaloes is typically log-normal, and peaks at systematically higher subhalo masses for recently-merged galaxies. The median host subhalo masses for the stellar-mass bins are shown as a function of redshift in Figure 4.6.

This raises the natural question of whether the excess bias detected for galaxies could be due simply to this offset in the typical mass of the host subhalo population. To test this idea, we generated for each galaxy bin a new parent galaxy population with the same distributions of stellar mass *and* host subhalo mass. The excess bias between this “corrected” galaxy population and the corresponding recently-merged galaxies is shown in Figure 4.5 as a dashed line. This exercise significantly decreases the excess bias signal, and no clear dependence on stellar mass or redshift remains. Nevertheless, a statistically significant excess bias (at the $\sim 10 - 20\%$ level) still seems to be present, especially for the lower stellar-mass bins. In summary, while for FOF dark matter haloes we did not find any statistically significant merger bias, for galaxies a signal is present at a level of $\sim 10 - 20\%$ for the smallest systems. However, when we restrict ourselves to galaxies at the center of FOF groups ($\sim 75 - 85\%$ of galaxies at $z = 2$ and $\sim 95 - 98\%$ at $z = 5$, depending on stellar mass), the excess bias approaches that obtained for dark matter haloes alone (§4.3.2). The differing results obtained for haloes and the galaxy population must therefore be due to the physics of the merger of galaxies, which goes beyond that of halo merging. Wetzel et al. (2009) and Angulo et al. (2009) found that recently-merged dark matter satellites sit in more massive haloes. This could in principle explain the different large-scale clustering behaviour, when including or excluding satellite galaxies. However, even when matching by halo mass instead of subhalo mass, we do not find an appreciable difference in the results. The treatment of satellite mergers is still a topic of active research in galaxy formation modelling, and we thus do not want to make firm conclusions on these results.

4.4 Implications for the clustering of quasars

The large clustering amplitude of quasars observed by Shen et al. (2007) at high redshift appears to suggest that these objects live in very massive haloes. In Figure 4.7, the bias associated with FOF halo merger events for different mass ranges and at different redshifts, is compared to the observed quasar bias², as calculated by Shen et al. (2009b). The high observed clustering is compatible with the clustering associated with the most massive DM haloes, which, at least up to $z \sim 4$, we find to be in better agreement with the analytical predictions of Jing (1998), rather than those of Sheth et al. (2001), though still somewhat higher at the highest redshifts.

As discussed in § 4.1, the high observed clustering signal forces quasar models to adopt extreme values for some of the relevant parameters, such as assuming very low scatter in the $L - M_{\text{Halo}}$ relation, high duty cycles, and high radiative efficiencies (White et al. 2008b; Shankar et al. 2008). However, an excess bias applying specifically to quasar hosts compared with random haloes of the same mass might reduce the need for such strong assumptions (Wyithe & Loeb 2009). The results

²To correct for the different cosmologies used, the large scale quasar bias measurements from Shen et al. (2009b) have been multiplied by $D_{\text{Shen}}(z) \sigma_{8, 0.78} / (D_{\text{Mill}}(z) \sigma_{8, 0.9})$, where D_{Shen} and D_{Mill} are the growth factor calculated for the cosmology used by Shen et al. (2009b) and the Millennium cosmology, respectively.

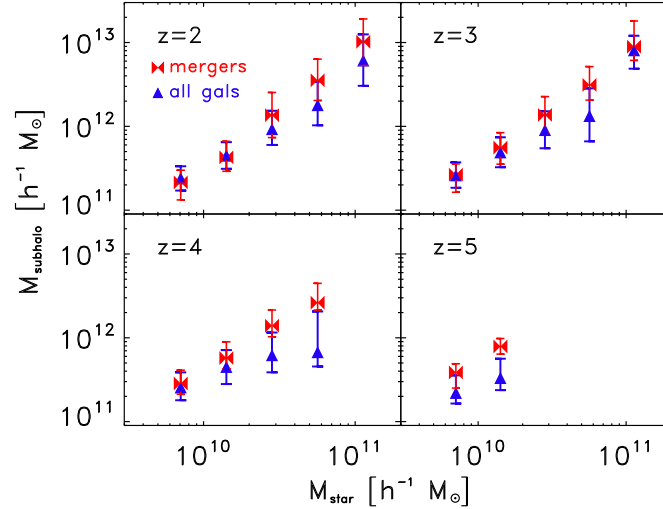


Figure 4.6: Median host DM subhalo mass corresponding to different stellar masses at different redshifts. The red bow-ties correspond to haloes hosting recently merged galaxies whereas blue triangles refer to the corresponding parent population. The error bars represent the 25 and 75 percentiles of the distribution.

of the previous sections for massive haloes and galaxies represent a challenge to this attractive explanation, at least if the excess bias is to be of merger origin. Figure 4.7 suggests that quasars at $z > 2$ live in haloes $\sim 10^{13} h^{-1} M_{\odot}$ which is broadly consistent with the average host halo mass estimated for lower redshift quasars (e.g., Croom et al. 2005).

If bright quasars have no significant excess bias due to their merger-driven nature, as our results suggest, then either there is another unknown source of excess bias, or, more simply, their clustering must trace the clustering of their host DM haloes and the discrepancy mentioned above must be explained in some other way. At this point it is therefore important to carry out a simple consistency check to see if there are enough massive haloes to host the luminous quasars actually observed in SDSS at $z \gtrsim 3$.

In the upper panel of Figure 4.8, we compare the number density of observed high-redshift quasars from Shen et al. (2007) with the number density of major halo mergers in the Millennium Simulation. Note that the information extracted from the simulation is a *rate* of mergers, i.e., the number of merger events within the time interval between two snapshots (see § 4.2). Therefore, when comparing with quasar number densities we are forced to assume a quasar optical visibility time t_q , that several independent studies have constrained to be relatively short and of the order of $t_q \sim 10^7 - 10^8$ yr (e.g., Shankar et al. 2004; Marconi et al. 2004; Martini 2004; Yu & Lu 2004; Bird et al. 2008, and references therein). In Figure 4.8 we choose to multiply the rates by a quasar visibility time of 10^8 yr, which is, at those redshifts, the approximate time between two snapshots of the Millennium Simulation. The resulting cumulative number densities are plotted in Figure 4.8 and are compared with the Shen et al. (2007) quasar number densities. The latter, taken from Table 5 in Shen et al. (2007) and converted to our cosmology, are shown with a grey band in Figure 4.8, which takes into account a factor of three uncertainty due to possible sources not visible in optical surveys due to obscuration/dust extinction and selection effects (from Hopkins et al. (2007b), the fraction of optically visible bright AGN is $\sim 1/3$).

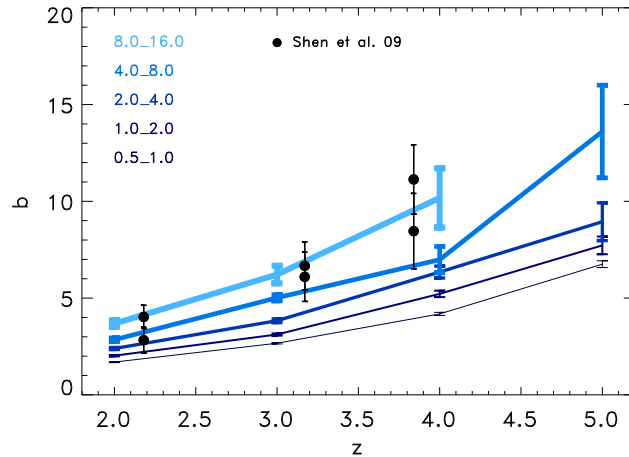


Figure 4.7: Bias of FOF halo merger remnants as a function of redshift for different mass ranges (as indicated on the plots, in units of $10^{12} h^{-1} M_{\odot}$). The symbols indicate the bias of bright quasars calculated by Shen et al. (2009b), inferred from the clustering observations of Shen et al. (2007) (at each redshift, Shen et al. (2009b) quote two values for the bias, which come from including or excluding negative points of the correlation function when performing the power-law fits to calculate the bias)

From this plot we conclude find that if $t_q \gtrsim 10^8$ yr, there are potentially enough mergers of massive haloes in the Millennium Simulation to match the number density and the large-scale clustering properties of $z > 3$ quasars. A merger model would require a fraction 20-25% of haloes with mass $\gtrsim 8 \times 10^{12} h^{-1} M_{\odot}$ to be active at $3 < z < 4$, in nice agreement with the analytical models of Shankar et al. (2008), who find a duty cycle of 0.2 – 0.4 within the same redshift range. We stress here that our mapping between haloes and quasars neglects any scatter between halo mass and quasar luminosity, which could spoil the agreement as discussed by White et al. (2008b). Significant scatter in the $L_{\text{QSO}} - M_{\text{halo}}$ relation would decrease the bias of quasars, since many would be hosted by lower mass (and hence less clustered) haloes.

The red-colored, dotted lines in Figure 4.8 mark instead the cumulative number densities of galaxy major mergers above different final masses, as labeled. The galaxy model predicts that, on average, the most massive galaxies that recently merged ($M_G \gtrsim 8 \times 10^{10} h^{-1} M_{\odot}$) reside in the most massive haloes of mass $\gtrsim 8 \times 10^{12} h^{-1} M_{\odot}$, with a stellar-to-halo mass ratio consistent with the one empirically inferred from the cumulative number matching between the stellar and halo mass functions (e.g., Vale & Ostriker 2004; Shankar et al. 2006; Conroy & Wechsler 2009; Moster et al. 2010). However, we find that the number of major mergers for such massive galaxies is below the number of major mergers of the corresponding hosts, as clearly seen in Figure 4.8 when comparing dotted to solid lines.

Keeping in mind that dynamical friction causes a time delay between halo mergers and galaxy mergers, there are several reasons why the number of mergers of haloes and galaxies at a given redshift is not equivalent. First of all, when two haloes merge, their host galaxies will merge at some later time only if the new satellite halo loses enough mass to fall below the resolution limit of the simulation. Moreover, in the current treatment of galaxy mergers, when a galaxy becomes a satellite, it loses its hot gas component; cooling is then inhibited and the stellar component grows only moderately from the cold gas previously available (we refer the reader to Wang & Kauffmann

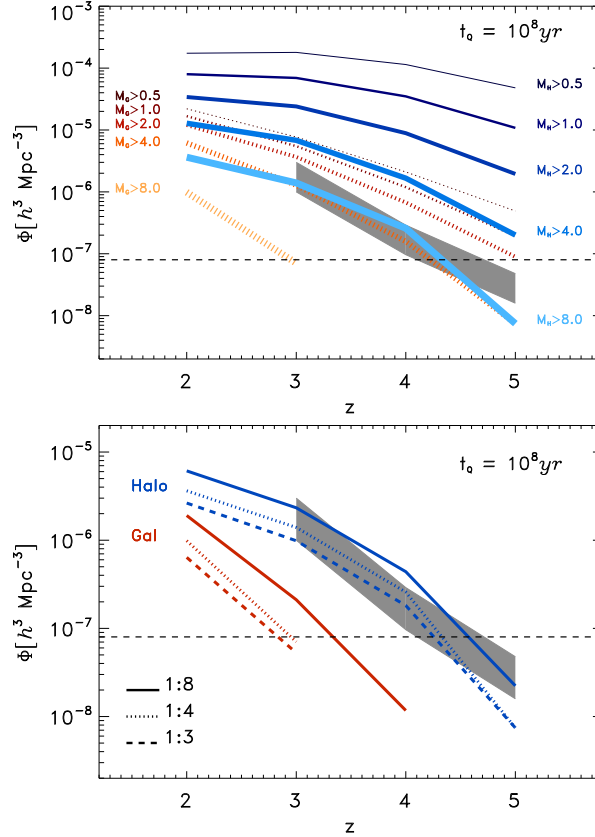


Figure 4.8: *Upper panel: Number density of observed bright quasars from Shen et al. (2007) (gray line), compared with the number of major mergers in the Millennium Simulation, obtained by multiplying the merger rate by a quasar lifetime $t_q = 10^8 \text{yr}$. The solid blue lines refer to the cumulative number density of halo mergers, whereas the red dotted lines show the cumulative number of galaxy mergers. The minimum mass corresponding to each line is shown in the plot in units of $[10^{10} h^{-1} M_\odot]$ for the galaxies and in units of $[10^{12} h^{-1} M_\odot]$ for the haloes. The number densities quoted by Shen et al. (2007) have been multiplied by a factor of three to account for objects missing from optical surveys due to obscuration. Lower panel: Number of major mergers for the most massive bins of galaxies and haloes ($M_G \gtrsim 8 \times 10^{10} h^{-1} M_\odot$ and $M_H \gtrsim 8 \times 10^{12} h^{-1} M_\odot$), obtained assuming different threshold for the mass ratios, as labeled.*

(2008) for a more detailed discussion on this). Therefore, although a given FOF halo merger may be counted as a major merger, by the time the corresponding galaxy merger occurs it may fall below our chosen threshold for a major merger. In any case, despite the fact that the number of major mergers is lower for galaxies than for haloes, the number of mergers of galaxies more massive than ($M_G \gtrsim 4 \times 10^{10} h^{-1} M_\odot$) is still large enough to explain the observed number densities of bright quasars.

Here we have assumed that only mergers with mass ratio above the adopted threshold (1 : 4) are able to trigger quasar activity. If a quasar could be turned on also by less dramatic events, the number density of predicted quasars would be higher. In the lower panel of Figure 4.8, we show the number density of merger events with different mass ratios mass ratio, for the most massive galaxies and haloes and assuming again an average lifetime of 10^8yr . From a 1 : 3 to a 1 : 8 mass ratio, the number of mergers increases but only by a factor of 2 – 3, and, even for the 1 : 8 threshold the

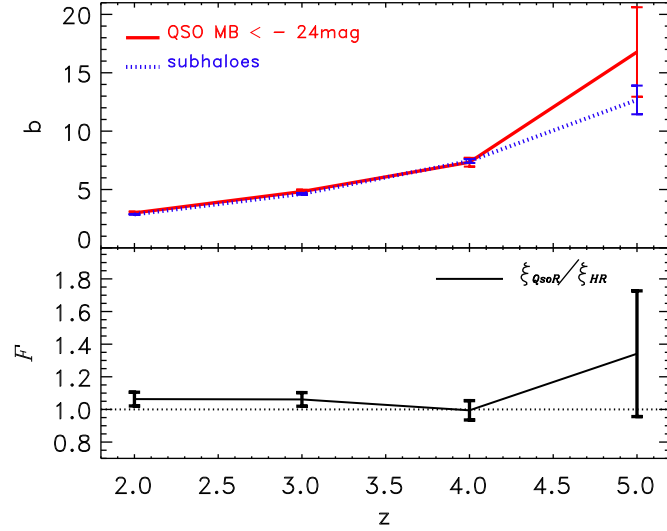


Figure 4.9: *Upper panel:* Bias of simulated bright quasars (B -band magnitude < -24 mag), compared with the bias of randomly selected subhaloes with the same mass distribution as the ones hosting the quasars. *Lower panel:* Excess clustering between the two populations.

number of galaxy mergers is not sufficient to explain the observed quasar number densities, unless the lifetime of bright quasars is much longer than 10^8 yr. We note that the number of galaxy mergers evolves more rapidly than the one of halo mergers, and, by $z \sim 2$, the two are discrepant only by a factor of a few.

Taken at face value, the galaxy model would then predict that the SDSS luminous quasars detected at $z > 2$ should be hosted by galaxies as massive as $\gtrsim 4 \times 10^{10} h^{-1} M_{\odot}$. Given that virial relations point to BHs more massive than $\gtrsim 3 \times 10^8 M_{\odot}$, this would suggest an increase, by a factor of $\gtrsim 3$, of the BH-to-stellar mass ratio with respect to local values (Häring & Rix 2004). In addition, we find that the clustering of galaxies with stellar mass $M_G \geq 4 \times 10^{10} h^{-1} M_{\odot}$ is too weak to match the observed quasar clustering.

To better address the connection with the semi-analytical galaxy models, we compare our results with the outputs of the detailed model for the coevolution of quasars and galaxies presented in Chapters 2 and 3. Figure 4.9 shows the bias of luminous optical quasars modeled with the assumption that quasar activity is triggered during galaxy mergers. In the previous chapter we showed that such a model predicts well the clustering properties of observed optical quasars at a variety of redshifts and luminosities, independent of the specific light curve characterizing the active phase of a BH. In the upper panel of Figure 4.9, the bias of bright quasars in the model is compared with the bias of randomly selected dark-matter subhaloes with the same mass distribution as the ones hosting the quasars. The ratio between the two-point correlation functions of the two samples is shown in the lower panel: the excess bias is at most $\sim 5\%$, except at $z = 5$, where the small number of simulated quasars results in a statistically unreliable result.

It is clear that if bright quasars were hosted by DM subhaloes less massive than inferred from the clustering analysis, the BH-to-stellar mass ratio would be even higher (see also the discussion in, e.g., Shankar et al. 2008). To address, in an independent way, the evolution of the average expected relation between the BH and its host, we compute the expected baryonic mass locked in BHs following the method outlined by previous authors (e.g., Ferrarese 2002; Cirasuolo et al.

2005; Shankar et al. 2006; Shankar & Mathur 2007; Shankar et al. 2008): first, we map haloes to their appropriate virial velocities V_{vir} at a given redshift z applying the virial theorem (e.g., Barkana & Loeb 2001). We then link V_{vir} to the velocity dispersion σ as calibrated in the local Universe by, e.g., Ferrarese (2002), and finally we compute the associated BH mass via the local $M_{\text{BH}}-\sigma$ relation (e.g., Tundo et al. 2007). If we assume that these BHs are accreting at an Eddington ratio $f_{\text{Edd}} \gtrsim 0.5$, we find that, at $z = 4$, all haloes above $\sim 5 \times 10^{12} h^{-1} M_{\odot}$ can indeed host a BH luminous enough to be recorded in the high- z quasar sample of Shen et al. (2009b). This simple exercise proves that if quasars are associated to normally biased haloes, the ratio between BH mass and halo mass could be similar to that observed locally. We stress, however, that in this simple exercise we ignored any possible scatter in all the relations that connect the black hole mass to the halo mass; such scatter would weaken the conclusions, since quasars could then be hosted by less massive, and therefore less clustered, haloes. We further note that while a no-evolution scenario for the $M_{\text{BH}} - M_{\text{halo}}$ relation could be viable, the relation between black hole mass and stellar mass must evolve, given the arguments on cumulative number matching shown in Figure 4.8 and also the recent observational results on the evolution of the $M_{\text{star}} - M_{\text{halo}}$ relation of Moster et al. (2010).

4.5 Summary of the chapter

In this chapter we exploited the large halo and galaxy samples extracted from the Millennium Simulation to test the idea that “merger bias”, a tendency of recently merged systems to be more strongly clustered on large scales than typical systems of similar mass, could help reconcile the apparent discrepancy between the observed abundance and clustering of high redshift quasars with those predicted for massive dark haloes. Previous studies have, in fact, shown that the quasar number density and clustering can be simultaneously explained theoretically either by models characterized by high duty cycles and negligible scatter in the $L_{\text{QSO}} - M_{\text{halo}}$ relation (White et al. 2008b; Shankar et al. 2008), or by models with non-zero scatter *and* an excess bias for the haloes hosting quasars (Wyithe & Loeb 2009).

We quantify the importance of merger bias at different redshifts and for different halo mass ranges. Defining as major mergers those events in which two friend-of-friend haloes of comparable mass merge into a single system between two simulation outputs, we found that recently merged haloes with masses in the range 5×10^{11} to $1.6 \times 10^{13} h^{-1} M_{\odot}$ show no significant excess clustering when compared to other haloes of similar mass.

To connect with physically motivated models of galaxy formation, we also looked for a possible merger bias among samples of galaxies selected from the semi-analytical model built on the Millennium Simulation (see the description of the model in Chapter 2). We considered galaxies with stellar mass in the range $5 \times 10^9 - 1.6 \times 10^{11} h^{-1} M_{\odot}$ and found that merger remnants are typically 10 – 30% more clustered than other galaxies of the same mass. The merger remnants are hosted by systematically more massive subhaloes than other galaxies, explaining a substantial part of this signal. However, even after correcting for this, we still observe excess bias at the level of $\sim 5\%$ for the most massive galaxy merger remnants, and of $\sim 20\%$ for our low-mass objects, which are insufficiently clustered to match the high bias of observed quasars. If we further restrict the analysis to central galaxies (i.e. galaxies at the center of a friend-of-friend group), for which a clear definition of halo mass is available, the excess clustering is once more diminished, approaching the null result obtained for haloes alone.

The clear result obtained for haloes and massive galaxies indicates that merger bias is unlikely

to be a viable solution to the apparent puzzle of the high clustering of high redshift quasars. On the other hand, we have also found that recently merged massive haloes with $M_{\text{halo}} \sim 10^{13} h^{-1} M_{\odot}$ could be both numerous enough and clustered enough to match the observed quasar number density and large-scale bias, if we assume a quasar visibility time $t_q \sim 1 \times 10^8$ yr and if we assume negligible scatter in the relation between halo mass and quasar luminosity.

In conclusion, if major mergers are responsible for triggering quasar activity, the lack of significant merger bias requires models to be characterized by high duty-cycles and negligible scatter in the relation between quasar luminosity and halo mass.

Chapter 5

Semi-analytic vs. hydrodynamical simulations

In this chapter we show some preliminary results of a direct comparison between the black hole population simulated with our semi-analytic model for galaxy formation and with hydrodynamical cosmological simulations.

The cosmological simulations are run with the same initial conditions used to generate the merger trees that constitute the backbone of the semi-analytic model. With this approach, we can not only compare the predictions for the time evolution of the global properties of black holes and quasars simulated with the two different numerical methods, but we can also select individual objects in the cosmological boxes and follow their history to isolate the differences in the black hole growth as treated with semi-analytical and fully-numerical simulations.

In §5.1 we introduce the topic of the chapter. In §5.2 we present the details of the simulations and a discussion of the two methods to treat the evolution of the baryons, with a particular emphasis on the treatment of the black hole growth. The first results on this comparison are presented in §5.3 and discussed in §5.4.

5.1 Introduction

In the last decade, models that use analytic prescriptions to follow the evolution of galaxies (and their supermassive black holes) within dark matter merger trees, have been proven successful in describing the main statistical properties of galaxies as a function of redshift (e.g., Kauffmann et al. 1993; Somerville & Primack 1999; Benson et al. 2003; Croton et al. 2006; De Lucia & Blaizot 2007; Monaco et al. 2007). Merger trees used for this kind of analysis can be derived analytically from Press & Schechter (PS) theory (Press & Schechter 1974), or can be measured from the outputs of collisionless dark matter cosmological simulations. In general, this second approach is preferred, since PS theory seems to underestimate the number of high-mass haloes (Springel et al. 2005c), and cosmological simulations provide also the spatial distribution of dark matter haloes, necessary, for example, for clustering analysis.

A more self-consistent way to study the evolution of the baryonic component of the Universe is through simulations that also include hydrodynamics. In the last few years, the code that has been most widely used for this purpose is GADGET, a publicly-available code which combines a N-body approach to follow the collisionless fluids with smoothed particle hydrodynamics (SPH;

e.g., Monaghan 1992) to follow the collisional gas (Springel et al. 2001b). In 2005, a treatment for the growth of black holes and quasar feedback has been incorporated into the code (Springel et al. 2005b). Simulations of isolated galaxy mergers with such a treatment have been successful in reproducing the $M_{\text{BH}} - \sigma_*$ relation (Di Matteo et al. 2005), and the properties of quasar light curves (Hopkins et al. 2005). The same model for BH growth has also been used by Li et al. (2007) in calculations that combine large-scale cosmological N-body simulations with hydrodynamic simulations of galaxy mergers to produce a bright quasar at $z = 6$ (e.g., Fan et al. 2001a). Recently, cosmological hydrodynamical simulations have become accessible, and the cosmological evolution of black holes and quasars has also been analyzed (Di Matteo et al. 2008; Degraf et al. 2010).

With state-of-the-art computational facilities, galaxy formation and evolution can thus be followed self-consistently with hydrodynamical simulations, but the dynamic range accessible with this approach is still relatively limited: to study the statistical properties of rare objects such as massive clusters or quasars, boxes with hundreds of comoving Mpc on a side need to be simulated, but, in such large-scale simulations, the resolution at small-scales can not reach sub-kpc scales.

With semi-analytic models, on the other hand, galaxy formation can be modeled in large-volumes without high computational cost, and a large dynamic range can be covered. For example, the galaxy population generated on top of the Millennium simulation includes both a large sample of bright clusters as well as galaxies down to low luminosities ($\sim 0.1 L^*$). For a statistical analysis of bright quasars, which have a very low space density, it is indeed important to simulate large boxes. The drawback of semi-analytical models is that they rely on many assumptions that risk to oversimplify the physics involved. Also, their outcome relies on many input parameters that can be degenerate with each other, thus diminishing the predictive power of some aspects of this modeling technique.

In summary, both semi-analytic models and hydrodynamical simulations offer advantages and drawbacks, and in the work presented below we compare the two methods directly, focusing on their predictions for the cosmological evolution of supermassive black holes.

5.2 The simulations

In this section we first describe the setting-up of the simulations, and then the baryonic physics entering in the hydro code and in the semi-analytic model, paying special attention to the treatment of black hole accretion and evolution.

5.2.1 The initial conditions

In the previous chapters we have, in several occasions, described the main properties of the Millennium Simulation, and N-body cosmological simulation with $2160^3 \approx 10^{10}$ dark matter particles in a periodic box of $500 h^{-1}\text{Mpc}$ on a side. The merger trees extracted from the simulation constitute the basic structure on which galaxies are evolved using analytic prescriptions for the baryonic physics. The Millennium run has a “sister” simulation called milli-Millennium, which is also a dark matter cosmological simulation, with the same mass resolution and cosmology, but smaller box ($62.5 h^{-1}\text{Mpc}$ on a side). When run on the merger trees of the milli-Millennium, the galaxy formation model still produces a quite large sample of galaxies (and their supermassive black holes).

As discussed in the previous section, hydrodynamical simulations are now computationally

	Milli-Millennium	hydro <i>Basic</i>	hydro <i>High_8</i>
N_p (dark matter)	270^3	270^3	540^3
Box size [h^{-1} Mpc]	62.5	62.5	62.5
m_{DM} [$h^{-1} M_\odot$]	8.60×10^8	7.06×10^8	8.82×10^7
m_{gas} [$h^{-1} M_\odot$]	—	1.55×10^8	1.94×10^7
softening [h^{-1} kpc]	5.0	5.0	2.5

Table 5.1: *Main numerical parameters of the simulations*

feasible for cosmological boxes with few tens of comoving Mpc on a side. For a direct comparison with the semi-analytic model, we therefore simulated the box of the milli-Millennium, using the same initial conditions (cosmological parameters and random phases): particles have the same initial distribution as in the initial conditions of the milli-Millennium but, before the simulation starts, they are split into a dark matter and a gas component, with the mass associated to each component depending on the cosmological baryon fraction assumed; the particle pairs are then displaced keeping the center of mass fixed at the initial distribution. We run a first simulation (called *Basic*), which has the same resolution as the milli-Millennium, and a second one with eight times better resolution (called *High_8*). The latter run was set-up by re-running the initial condition code, with identical amplitudes and phases for the large-scale modes, but with new small-scale modes added to reach the Nyquist frequency of the new simulation. This approach guarantees that the same haloes are formed, but the resolution at small scales is increased. The simulations were run using GADGET3, an updated version of GADGET2 (Springel 2005).

In table 5.1 the main numerical parameters adopted in our simulations are shown. The particle number for the two hydrodynamical simulations refers to the particle number before the splitting. Effectively, for the hydro simulations the total number of particles is twice as large.

Throughout this chapter, we will often refer to “haloes” and “subhaloes”, both when discussing the hydrodynamical simulations and the semi-analytic models. For both types of simulations, haloes are identified using a friend-of-friends (FOF) group-finder, whereas subhaloes are identified using an extended version of the SUBFIND algorithm (Springel et al. 2001a).

5.2.2 The baryonic physics in GADGET

As mentioned in the introduction of this chapter, the code GADGET uses an N-body approach to treat the collisionless fluids (dark matter, stars and black holes), whereas SPH is used to follow the evolution of the gas. With the current computational facilities, it is still prohibitive to simulate the entire dynamic range necessary to follow the large-scale evolution of galaxies as well as the physics connected to molecular clouds, star formation and black hole accretion. Instead, for the physics connected to small-scale processes, sub-grid treatments are adopted: in this approach, the small-scale physical conditions of the gas are estimated based on the gas properties at scales resolved by the simulation. In the code used for our simulations, cooling, star formation and supernova feedback are treated using the sub-resolution multiphase model developed by Springel & Hernquist (2003a), where the inter-stellar medium is described by a two-phase medium, consisting of cold clouds embedded in the ambient hot gas. As soon as clouds cool to form stars, a fraction of the newly formed stars is assumed to be short-lived and to die instantaneously as supernovae. The fraction of

short-lived stars depends on the initial mass function, which is usually assumed to be Salpeter-like (Salpeter 1955). Supernova feedback and the evaporation of cold clouds increase the density of the surrounding hot gas, triggering subsequent star formation in a self-regulated fashion. We refer to Springel & Hernquist (2003a) and Springel & Hernquist (2003b) for details of the model and its success in reproducing the most important properties of star formation as a function of cosmic time. Radiative cooling and heating by photoionization are implemented in a way similar to Katz et al. (1996). For further details on the gravitational force calculation and time integration of the code, we refer to Springel (2005).

In what follows, we describe only the numerical details of the treatment of supermassive black holes. This modeling for the growth and feedback from BHs has been introduced by Springel et al. (2005b); Di Matteo et al. (2005). Black holes are represented by collisionless “sink” particles. An on-the-fly FOF finder is regularly called to select all haloes above a given mass threshold (in our simulations this threshold is $4 \times 10^{10} h^{-1} M_{\odot}$); if a halo above this threshold does not already contain a black hole, the densest gas particle within the halo is converted into a sink particle with a given seed mass. In the runs presented here, the seed mass is assumed to be $10^5 h^{-1} M_{\odot}$. As discussed in the introduction of the thesis and in §3.2, the origin of supermassive black holes is still a matter of debate. However, the choice of the initial seed mass does not influence the results presented here, provided it is not too small. The value we adopt is consistent with the choice of Di Matteo et al. (2008), and approximately puts the black hole onto the local observed scaling relation between black hole mass and galaxy mass. After the most dense gas particle has been converted into a black hole seed, the new BH particle interacts with the environment only gravitationally. The mass of the black hole can then grow through accretion of the surrounding gas, or through mergers with other black holes, as described below.

Black hole accretion and feedback

The rate of accretion of gas onto the black hole is estimated using a Bondi-Hoyle-Lyttleton parametrization (Bondi & Hoyle 1944; Bondi 1952, see also §A.2). According to this parametrization, for steady, spherically symmetric accretion, the rate depends on the properties of the surrounding gas as:

$$\dot{M}_{\text{BH}} = \frac{4 \pi \alpha G^2 M_{\text{BH}}^2 \rho}{(c_s^2 + v^2)^{3/2}}, \quad (5.1)$$

where ρ and c_s are, respectively, the density and sound speed of the gas and v is the velocity of the black hole relative to the gas. α is a dimensionless parameter which, in the correct formulation of the Bondi accretion rate should be of order of unity; however, as our subresolution model for the interstellar gas computes average values of the density and sound speed of the hot and cold phases, a larger value of α (of the order of one hundred) is necessary to correct for this ISM averaging procedure. In our simulations, the accretion is always assumed to be radiatively efficient, and black holes are not allowed to accrete at a rate higher than the Eddington rate (which is the accretion rate that would produce the Eddington Luminosity, as described in Appendix A). The radiative efficiency ϵ is assumed to be constant at the value of 0.1 (we refer the reader again to Appendix A for a discussion on the values of the radiative efficiency). At any given time, the radiative luminosity is then given by $L = \epsilon \dot{M} c^2$, with the upper limit given by the Eddington Luminosity. Feedback from the accreting black hole is modeled assuming that a fraction ϵ_f of the emitted luminosity can couple thermally to the surrounding gas, so that the energy per unit time that the accreting black hole is

transferring (isotropically) to the surrounding medium is given by:

$$\dot{E}_{\text{feed}} = \epsilon_f L. \quad (5.2)$$

ϵ_f is a free parameter of the simulation, and is it here assumed to be 0.05, following the results of Di Matteo et al. (2005) and Springel et al. (2005b), who showed that such a value for the coupling efficiency reproduces the normalization of the $M_{\text{BH}} - \sigma_*$ relation at $z = 0$. Simulations of isolated galaxy mergers run with this model have shown that black holes accrete gas efficiently, often reaching the Eddington limit, while the host galaxy is experiencing a strong starburst. Eventually, the feedback from the central object becomes powerful enough to heat and blow away the surrounding gas, leaving the black hole without further “fuel”. In this picture, the black hole is thus regulating its own growth through feedback, reaching a final mass that is in agreement with the $M_{\text{BH}} - \sigma_*$ relation (Di Matteo et al. 2005; Robertson et al. 2006; Hopkins et al. 2006b).

Another feedback mode has been modeled by (Sijacki et al. 2007) to account for the mechanical feedback from an AGN accreting at low rates. This feedback takes the form of bubbles driven by the AGN into the environment and is particularly important in the centers of galaxy clusters in suppressing cooling flows. However, since in this phase the black hole is not increasing its mass significantly, this mode of accretion is not particularly relevant for the current analysis.

Black hole mergers

As discussed in §1.5.3, the timescales on which a black hole binary is able to shrink to orbital scales small enough for gravitational radiation to be efficient and to thereby quickly bring the black holes to coalescence, is still not clear. In an case, it very much depends on the local conditions at galaxy centers. Since we are unable to resolve the scales of interest for a black hole binary in our simulations, it is assumed that black holes merge if they come within the spatial resolution of the simulation and their relative speed is below the sound speed of the surrounding gas. This last criterion avoids the merger of two black hole in a “flyby” event, for example during the first encounter in a galaxy merger.

5.2.3 The baryonic physics in the semi-analytic model

In §2.2 we have described the analytic prescriptions used, together with dark matter merger trees, to study the evolution of the galaxy population with a semi-analytic approach. We refer to that Section and to Croton et al. (2006); De Lucia & Blaizot (2007) for details on this.

We here review only the details of the black hole treatment that are necessary for the comparison with the hydrodynamical simulations.

In the semi-analytic model, merger trees are “walked” back in time until the first resolved haloes appear. Every newly formed halo is populated with a galaxy, which is initially just made of gas, according to the baryon fraction that depends on the assumed cosmology. This gas can then start cooling and forming stars as described in §2.2. Together with the gas, we populate haloes with a black hole seed. The results of the previous chapters have been obtained for models with an assumed seed mass of $10^3 M_{\odot}$ but, as discussed in §3.2, all results are essentially independent on the value adopted for the seed. Here, to be consistent with the hydro runs, we assume a seed mass of $10^5 M_{\odot}$.

Black hole accretion and feedback

The main assumption of the current black hole model in our semi-analytic approach is that galaxy mergers are the physical processes able to channel gas towards galaxy centers and trigger efficient black hole accretion (see also §1.5.2). During merger events, we assume that the BHs hosted by the merging galaxies instantaneously coalesce and form a single BH whose mass is the sum of the progenitor BHs, and that this resulting BH starts accreting a fraction of the available cold gas. As described in §3.2.3, the fraction of gas that the central black hole accretes is given by:

$$\Delta M_{\text{BH,Q}} = \frac{f'_{\text{BH}} m_{\text{cold}}}{1 + (280 \text{ km s}^{-1} / V_{\text{vir}})^2} (1 + z_{\text{merg}}), \quad (5.3)$$

where m_{cold} is the total mass of cold gas in the final galaxy, z_{merg} is the redshift of the merger and $f'_{\text{merg}} = f_{\text{merg}} (m_{\text{sat}}/m_{\text{central}})$, where $f_{\text{merg}} \approx 0.02$ is a normalization parameter chosen to match the observed locally $M_{\text{BH}} - M_{\text{Bulge}}$ relation, and $m_{\text{sat}}/m_{\text{central}}$ is the mass ratio of the merging galaxies. To estimate the bolometric luminosity associated with the accreting black hole, we have to estimate the time it takes the black hole to accrete the available gas. We follow here the Model II described in §3.2.3. This model assumes that a fraction of the gas is accreted at the Eddington rate, until the black hole reaches a peak of luminosity L_{peak} , after which the accretion rate decreases and the corresponding AGN is in a “quiescent” luminosity phase (Hopkins et al. 2005).

At any given time, the bolometric luminosity emitted by an accreting BH is given by

$$L_{\text{bol}}(t) = f_{\text{Edd}} \frac{M_{\text{BH}}(t)}{t_{\text{Edd}}} c^2, \quad (5.4)$$

where f_{Edd} is the fraction of Eddington luminosity emitted, and $t_{\text{Edd}} = \sigma_{\text{T}} c / (4\pi m_p G) \sim 0.45 \text{ Gyr}$ (see also eq. 3.5). If, at any given time, the radiative efficiency and the Eddington ratio are known, the accretion rate is given by:

$$d \ln M_{\text{BH}}(t) = \frac{dt}{t_{\text{ef}}(t)}, \quad (5.5)$$

where $t_{\text{ef}}(t) = \frac{\epsilon}{1-\epsilon} \frac{t_{\text{Edd}}}{f_{\text{Edd}}(t)}$ is the e-folding time ($t_{\text{ef}} \equiv t_{\text{Salpeter}}$, if $f_{\text{Edd}} = 1$). In our approach, we assume that a fraction $\mathcal{F} = 0.7$ of the gas is accreted at the Eddington rate ($f_{\text{Edd}} = 1$), and in the quiescent phase the luminosity is characterized by a decreasing f_{Edd} , derived by following Hopkins et al. (2005), who suggest that the average time that an AGN spends in a logarithmic luminosity interval can be approximated by:

$$\frac{dt}{d \ln L_{\text{bol}}} = |\alpha| t_9 \left(\frac{L_{\text{bol}}(t)}{10^9 L_{\odot}} \right)^{\alpha}, \quad (5.6)$$

where $t_9 \equiv t_Q(L' > 10^9 L_{\odot})$ and $t_Q(L' > L)$ is the total AGN lifetime above a given luminosity L . Hopkins et al. (2005) found from merger simulations that $t_9 \sim 10^9 \text{ yr}$ over the range $10^9 L_{\odot} < L_{\text{bol}} < L_{\text{peak}}$; here, we assume always $t_9 = 10^9 \text{ yr}$. In the range $10^{10} L_{\odot} \lesssim L_{\text{peak}} \lesssim 10^{14} L_{\odot}$, Hopkins et al. (2005) also found that α is a function of only the AGN luminosity at the peak of its activity, L_{peak} , given by $\alpha = -0.95 + 0.32 \log(L_{\text{peak}}/10^{12} L_{\odot})$, with $\alpha = -0.2$ as an upper limit.

In the treatment for black hole growth in the semi-analytic model, we do not include an explicit prescription for feedback from black holes in a quasar phase. Indirectly, the growth of the hole is regulated by the amount of gas that it is allowed to swallow, as given by Equation (5.3).

As in the hydrodynamical simulations, in the semi-analytic model we also account for the

feedback produced by an AGN accreting hot gas at low-rates. During those phases, the BH does not increase its mass significantly, and the radiative output is a small fraction of the bolometric luminosity (see §3.2.2). Therefore, the results shown in this chapter are independent on the details of this mode.

Black hole mergers

As for the hydro runs, in the semi-analytic model we also assume that two black holes in a binary system can merge on a short time scale. While in the hydrodynamical simulations the moment of the merger can be estimated using physical conditions of the surroundings, in the semi-analytic model we assume that two black holes merge as soon as the parent galaxies have merged.

5.3 Results for the black hole population

In this section we compare the predictions of the hydro runs and the semi-analytical model on the major global descriptors of the black hole and quasar populations in the local Universe and as a function of redshift.

5.3.1 The most massive haloes

In Figure 5.1 and 5.2 we show 2-d maps of the nine most massive haloes from the *High_8* hydrodynamical simulation and the semi-analytic model, respectively. In the first case, a random subsample of the particles in each halo is shown, whereas for the semi-analytic case, we show the space distribution of the galaxies, which approximately follows the distribution of the substructures in each halo. We are clearly able to match haloes from the hydro runs and the semi-analytic model, which allows a direct comparison of individual structures. Despite the good match, small differences in some properties of the haloes are expected, since in the hydro runs the dark matter particles are split into a dark matter and a gas component after the initial conditions are generated, as we explained in §5.2.1. The smaller mass in the dark matter particles, and the presence of the gas are at the origin of small differences in the halo properties such as the virial masses quoted in each panel of the figures (the virial mass is defined as the mass within the radius that encloses a mean overdensity of 200 times the critical value).

In the same figures, we also show with colored circles the positions of the black holes present in the groups. The purple triangles indicate the position of the most massive black hole in each group. Overall, there is good agreement in the location of the most massive hole as predicted by the hydro run and the semi-analytic model, except for a couple of cases where they do not coincide (e.g., the halo in the central panel of each figure). We note, however, that the mass difference between the most massive black holes in each group can be quite small, and fluctuations in the mass ranking are expected. Globally, the number of massive black holes in each halo is qualitatively similar in the hydro run and in the semi-analytic model. We discuss this further in the next subsection.

5.3.2 The black hole mass function and mass density

In Figure 5.3 we compare the redshift-zero black hole mass functions predicted by the hydro runs and the semi-analytic model. In the top panels the black hole function predicted by the *Basic* and the *High_8* runs are shown (solid blue lines). The predictions depend on the simulation resolution.

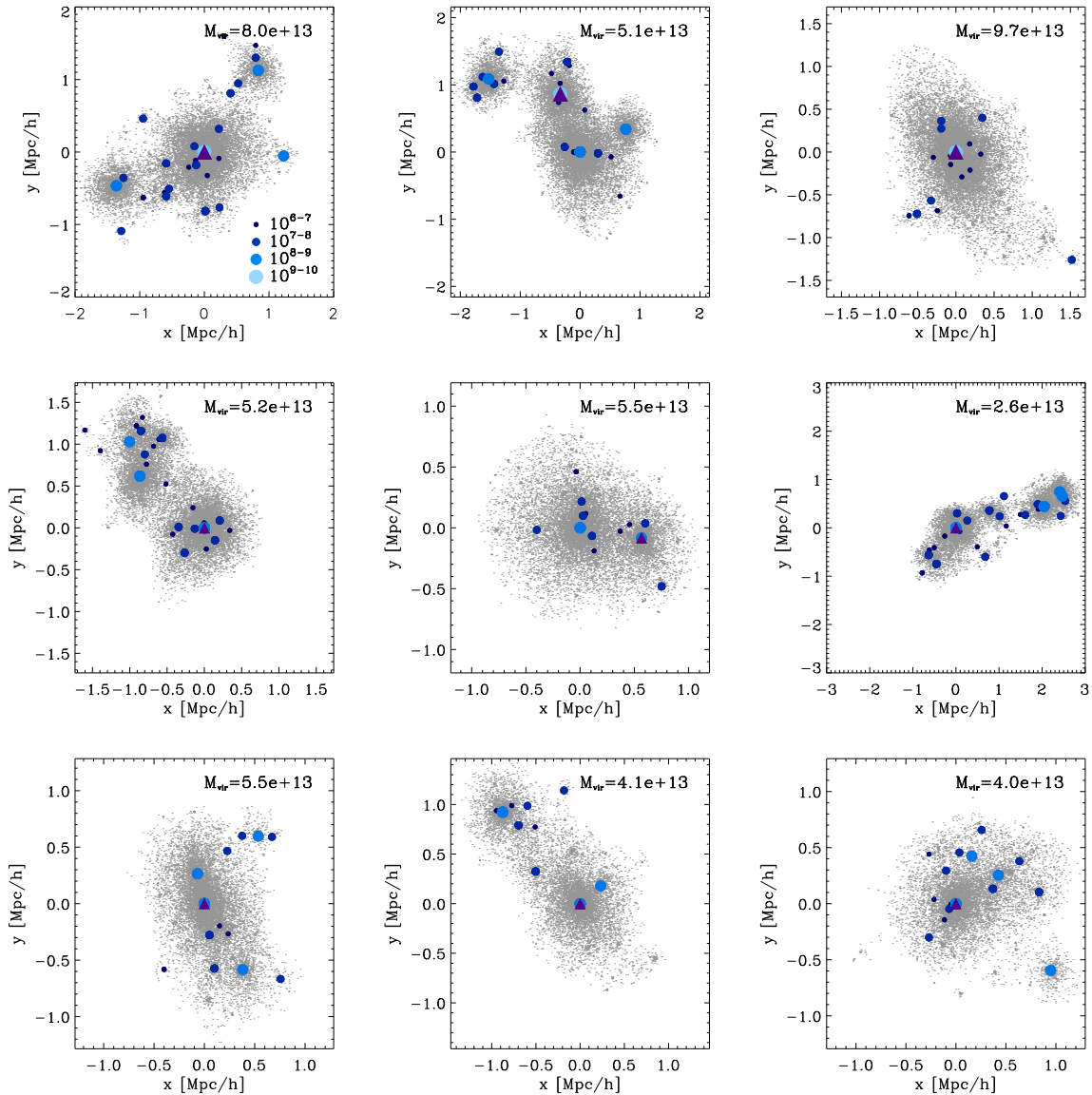


Figure 5.1: $x - y$ maps of the most massive haloes at $z = 0$ from the “High_8” run. The haloes are selected with the FOF group-finder and are ranked according to their total number of particles. On each panel, the virial mass corresponding to each halo is indicated, in [$h^{-1} M_{\odot}$]. The grey points are a random sample ($\sim 1\%$) of the particles in the haloes, and the blue circles indicate the positions of the black holes, with size and color of the circles that on the black hole mass as indicated in the first panel, in [M_{\odot}]. The purple triangles indicate the position of the most massive black hole in each group.

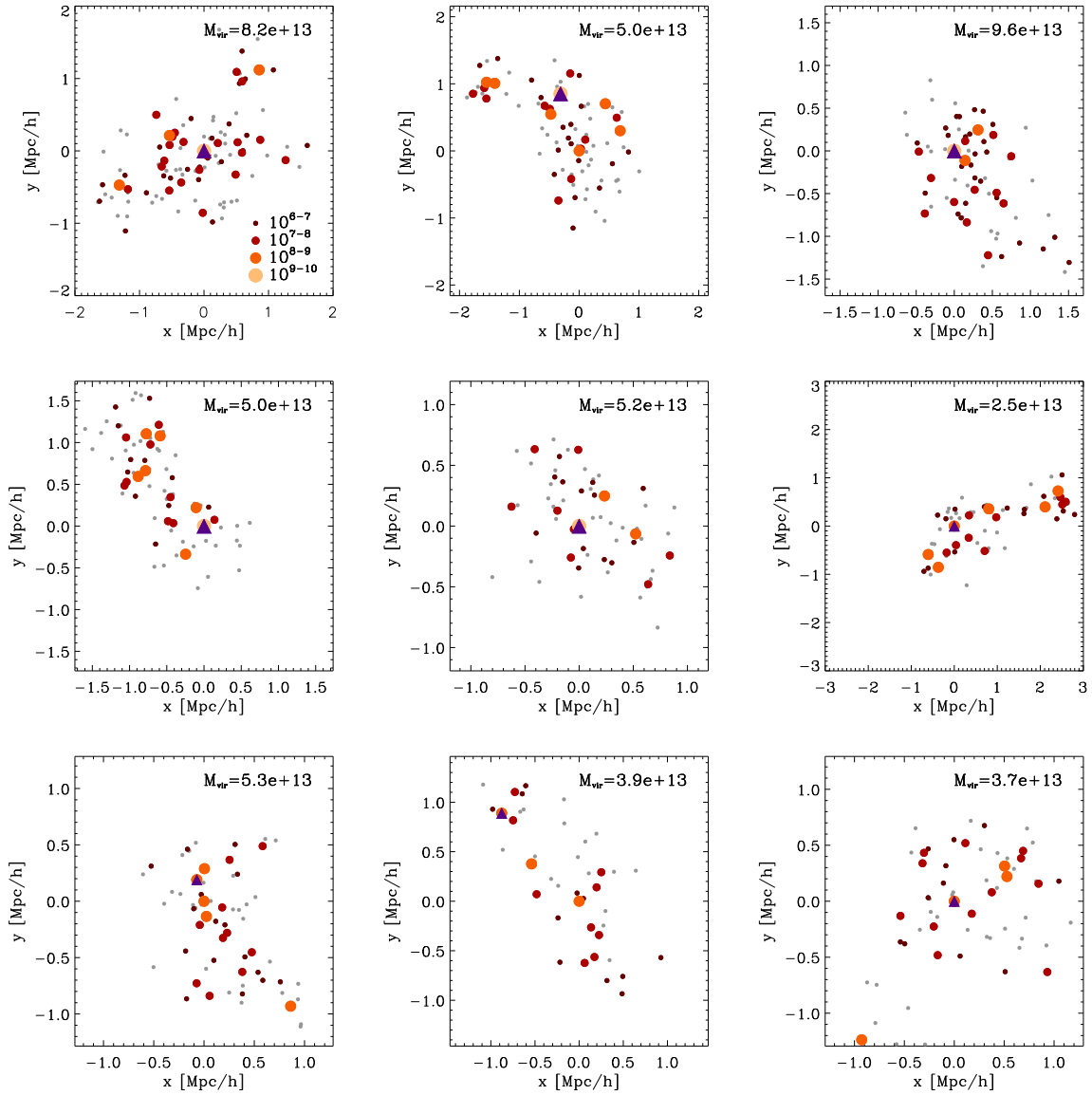


Figure 5.2: Same as the previous Figure, but for the groups and black holes from the semi-analytic model run on top of the milli-Millennium. The grey points indicate the position of the galaxies, and the red circles the positions of the black holes. Each of this halo has his correspondent in the previous Figure.

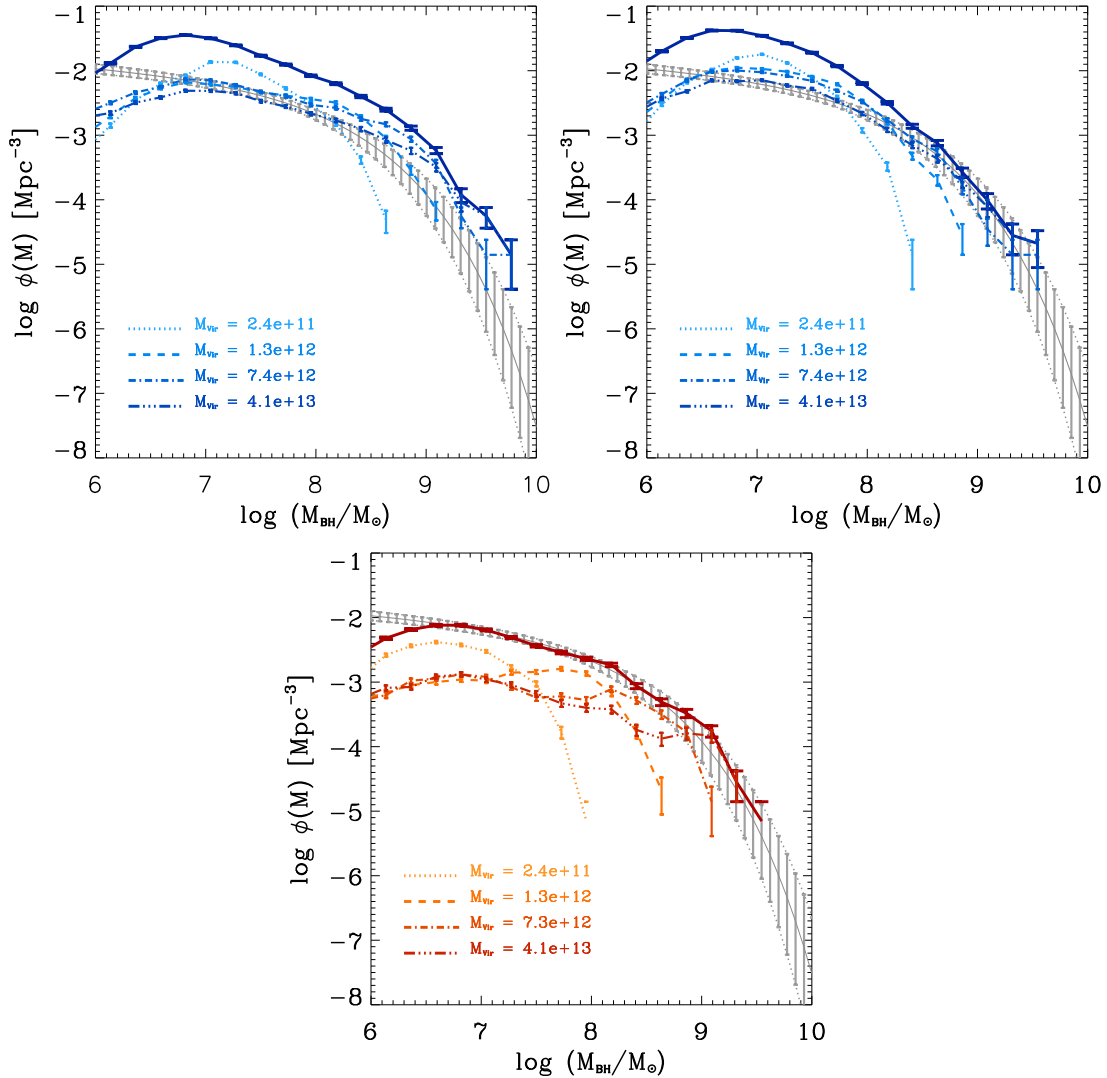


Figure 5.3: Black hole mass function at $z = 0$ as predicted by the “Basic” and the “High_8” hydrodynamical simulations (top-left and top-right panel, respectively), and by the semi-analytic model (lower panel). In each panel, the grey band indicate observational constraints from Shankar et al. (2004). The solid lines show the total predicted black hole mass functions, whereas the other thinner lines in each panel indicate the mass function of black holes residing in haloes with median mass as indicated on the panels.

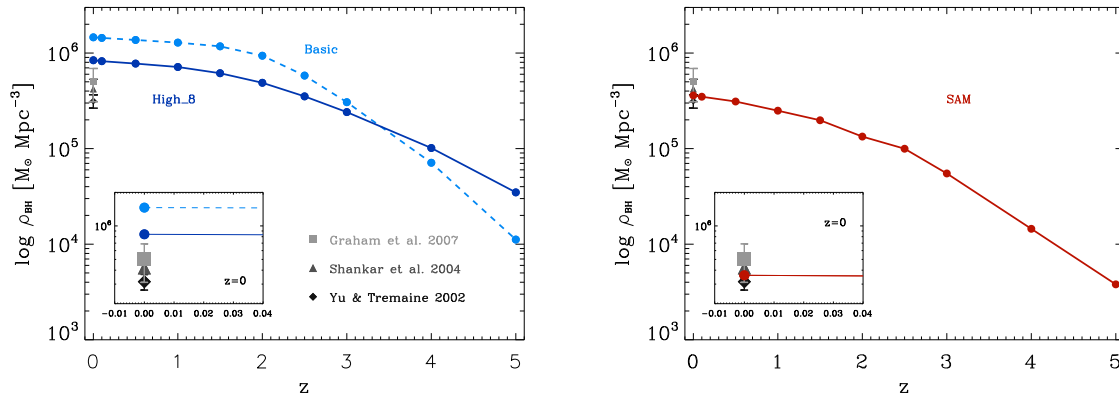


Figure 5.4: Predicted redshift evolution of the black hole mass density as predicted by the *Basic* and *High_8* hydrodynamical simulations (left panel) and the semi-analytic model (right panel). At $z = 0$, the predicted values are compared with the observational estimates of various authors, as indicated.

The *Basic* simulation over-predicts the number of black holes at all masses. The run with higher resolution over-predicts the number of small and intermediate mass black holes, but is in agreement with observational estimates (grey band) at the high-mass end. We also looked at the contributions to the total mass function from black holes in dark matter haloes of various mass. The haloes are divided into four bins, logarithmically-spaced, from a mass of $\sim 10^{11}h^{-1} M_{\odot}$ to the highest halo mass in each run ($\sim 10^{14}h^{-1} M_{\odot}$). The median mass of each bin is indicated in the figure. Overall, in the *Basic* run the number of more massive black holes is higher for all dark matter haloes. This is probably due to an excessive number of BH mergers due to the poor resolution. The problem seems to be solved in the higher resolution run, even though only future runs with yet higher resolution will be able to reliably establish whether this is already converged. The bottom panel of the figure shows the same quantities as predicted by the semi-analytic model. The good fit with the observational data is the result of the recipe adopted for black hole accretion, as already discussed in Chapters 2 and 3. The contribution to the total mass function strongly depends on the hot halo of the black hole. The correlation between black hole mass and halo mass is, in fact, despite some scatter, relatively tight, as shown in Figure 3.15 of Chapter 3. The *High_8* run and the semi-analytic predictions are in broad agreement at the high-mass end.

The redshift evolution of the black hole mass density as predicted by the different numerical methods is shown in Figure 5.4. The left panel shows the evolution predicted by the two hydro runs. The evolution is clearly resolution-dependent. In the *Basic* run, the mass-density evolves very rapidly down to $z \sim 2$ (dashed line), after which it settles to a value which is almost an order of magnitude higher than the observational estimates ($\sim 3\text{--}4 \times 10^5 [\text{M}_{\odot}/\text{Mpc}^3]$, e.g., Graham & Driver (2007)). The evolution of the mass density in the higher resolution run (solid dark-blue line) is quite different: higher fraction of the black hole total mass is already formed at $z \sim 5$, and the subsequent evolution is much milder. The $z = 0$ value reached in the *High_8* run is much closer to the observational estimates.

Interestingly, in the semi-analytic model, the prediction for the redshift evolution of the black hole mass density is quite different. While the parameters entering the BH growth have been tuned to match the local value, the redshift evolution is a pure prediction of the model, and the assumption

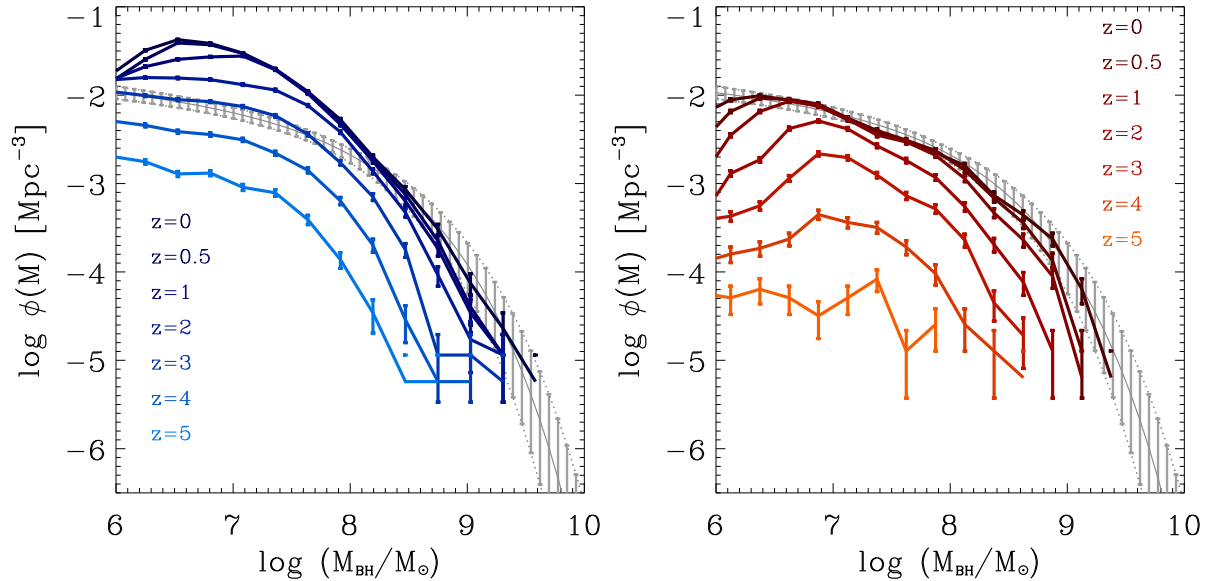


Figure 5.5: Predicted redshift evolution of the black hole mass function as predicted by the *High_8* hydrodynamical simulation (left panel) and the semi-analytic model (right panel).

that black hole accretion is triggered during galaxy mergers.

Finally, the redshift evolution of the black hole mass function is shown in Figure 5.5, for the *High_8* run (left panel) and the semi-analytic model (right panel). As evident also by the evolution of the black hole mass density, the evolution of the mass function is more dramatic for the semi-analytic model.

5.3.3 The quasar luminosity function

In Figure 5.6 the bolometric luminosity function of active black holes as predicted from the model is shown at various redshifts and compared with the observational-data compilation of Hopkins et al. (2007b). In the top panel, the predictions from the hydro runs are shown, with the light blue dashed line indicating the prediction from the *Basic* run, and the solid blue line giving the *High_8*. Overall, the predictions from the two runs are not significantly different from each other, but they both strongly overestimate the number of faint objects at high redshift. In the local Universe, the predictions are in quite good agreement with observed data. These results are broadly consistent with the findings of Degraf et al. (2010), who analyzed the luminosity function predicted by the simulations presented in Di Matteo et al. (2008), concentrating mainly on the faint end, given the small boxes they used (their best-resolved run is in a $33.75 [h^{-1} \text{ Mpc}]$ box). These authors found a good agreement with observations at $z \sim 0.5$, and at $z < 2$ for the brightest accessible luminosities. At high redshifts, their simulations also overestimate the number of faint objects, although this might be underestimated by current observations.

The large discrepancies between the predicted and the observed faint luminosity functions are in part due to resolution effects (see also the discussion in Degraf et al. 2010), but stronger constraints on the shape and evolution of the quasar luminosity function will be provided by future high-redshift surveys observing both obscured and optically-visible AGN (such as eROSITA, PAN-STARRS, VST

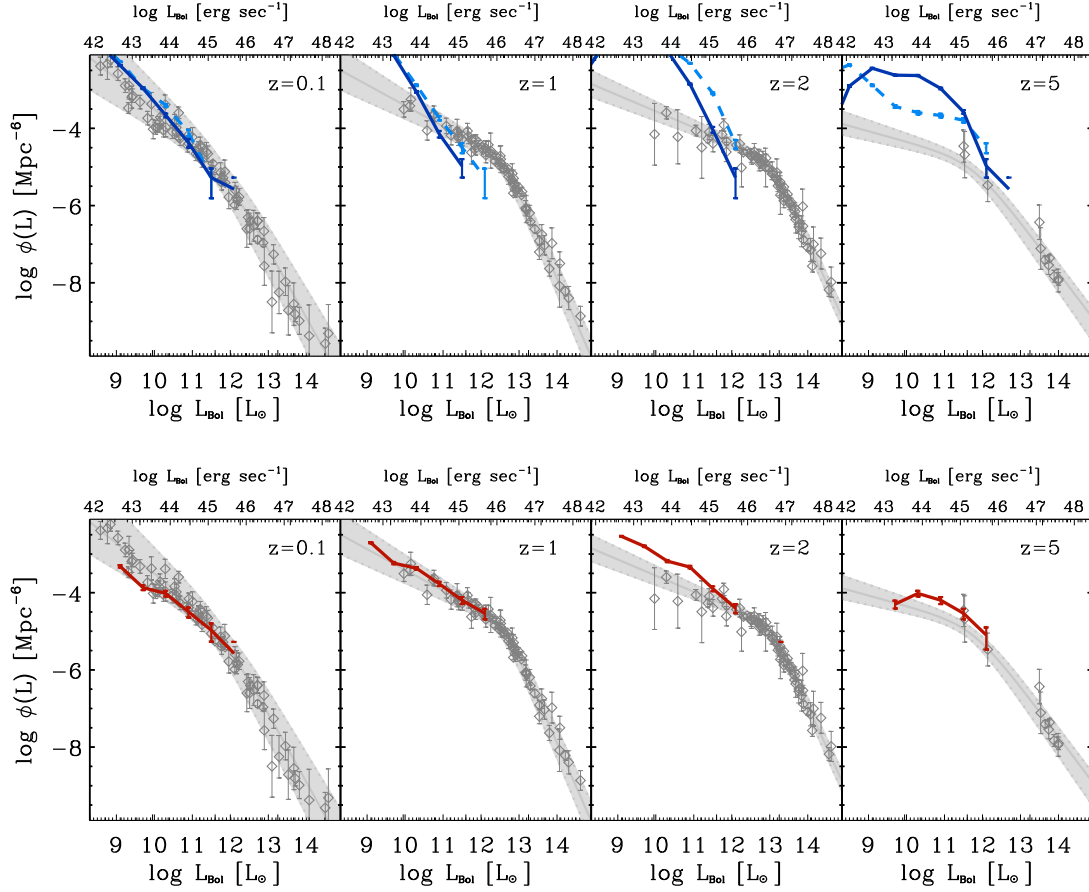


Figure 5.6: Predicted quasar bolometric luminosity function at various redshifts as predicted by the Basic and High-8 hydrodynamical simulations (top panels, dashed line and solid blue line respectively) and the semi-analytic model (lower panel). The luminosity functions are compared with the compilation of observed data by Hopkins et al. (2007b) (grey points with best fit given by the grey band).

and VISTA). These future data will be particularly important to test models of black hole accretion in hydrodynamical simulations.

In the lower panel of Figure 5.6, the quasar luminosity function from the semi-analytic model is shown. The agreement with observations is overall quite good when a model which accounts for an Eddington-limited phase followed by a quiescent one is assumed. As discussed in more detail in Chapters 2 and 3, the main problem of a model that assumes efficient black hole accretion only during galaxy mergers is the production of enough very-bright objects at high redshift. In this figure this challenge is not really addressed, since the number-density of very bright objects is too low to have a useful sample of them in the milli-Millennium, but it can be studied with the predictions from the Millennium in Figures 2.7 and 3.3).

5.3.4 The $M_{\text{BH}} - \sigma_*$ relation

The scaling relations between black hole masses and the properties of the host galaxies, are very well established in the local Universe (see §1.4.1), and are one of the most important constraints

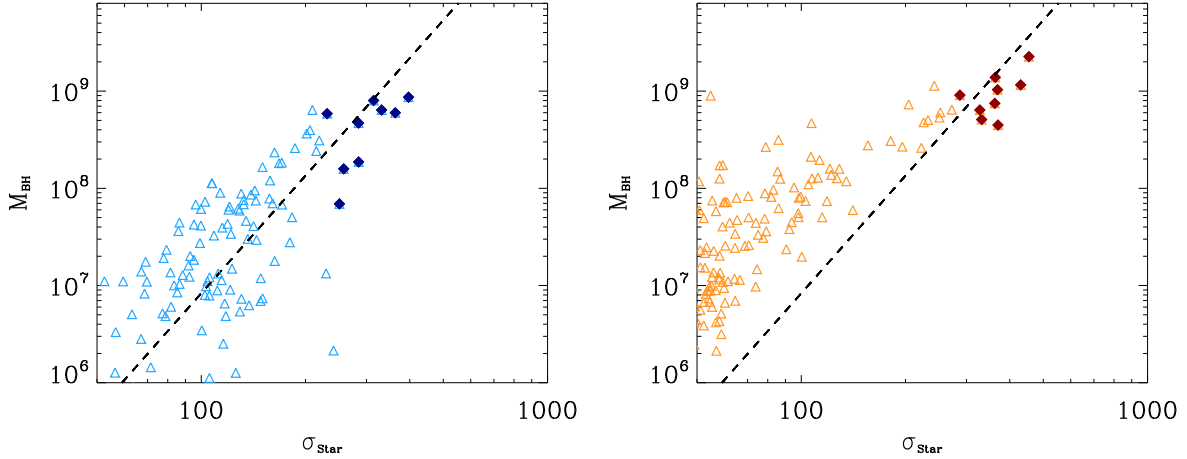


Figure 5.7: $M_{\text{BH}} - \sigma_*$ relation for the black holes populating the groups shown in Figures 5.1 and 5.2 as predicted by the *High_8* hydrodynamical simulation (left panel) and the semi-analytic model (right panel). The filled symbols refer to the location in the relation of the main halo of each group. The black dashed line indicates the best-fit of Tremaine et al. (2002).

for models that want to describe the cosmological evolution of supermassive black holes. In Figure 5.7, we show the predicted scaling between the masses of the black holes populating the groups shown in Figures 5.1 and 5.2, and the velocity dispersion of the galaxies they reside in. For the hydrodynamical simulation, we show the result of the *High_8* run, where the star particles within the half-mass-radius of each galaxy are used to calculate the velocity dispersion. For the semi-analytic model, we do not have information on the stellar velocity dispersion, but we estimate it by assuming that the circular velocity v_c of each halo is equal to the virial velocity of the halo, and then the velocity dispersion is derived using the relation from Baes et al. (2003):

$$\log v_c = (0.96 \pm 0.11) \log \sigma + (0.32 \pm 0.25), \quad (5.7)$$

where the velocity dispersion and the circular velocity are given in km s^{-1} . In the figure, the solid symbols indicate the relation for the main haloes of each group. The dashed-line indicates the best-fit relation of Tremaine et al. (2002). The hydrodynamical simulation clearly gives a good prediction for the relation, as also shown by Di Matteo et al. (2008) and Sijacki et al. (2007). For the semi-analytic model, the match is really good for the most massive black holes populating the central galaxies. The match with the observed relation is less satisfactory for the less-massive black holes. We note, however, that the value for σ_* for the semi-analytic model is derived with several assumptions: we assumed $v_c = v_{\text{vir}}$, but this relation might not always hold; in particular, for less massive haloes, the circular velocity might be larger than the virial velocity, thus pushing the velocity dispersion to higher values (see Seljak 2002, and the discussion in §2.3.1).

5.4 Summary of the chapter

In this chapter, we presented preliminary results of a direct comparison between the black hole and quasar populations as simulated with the hydro-code GADGET and our semi-analytic model for

galaxy formation. The objective of this work is to fully understand the advantages and limitations of the two approaches in modeling the black hole evolution. Generally, the semi-analytic approach suffers from an over-simplification of the gas physics necessary to model galaxy formation. In hydrodynamical simulations the collisional component of the Universe is followed more self-consistently, but there is still need to invoke sub-grid physics to describe phenomena such as star-formation, that can not be properly resolved. On the other hand, compared to hydrodynamical simulations, semi-analytic models are able to simulate a larger dynamic range with significantly smaller computational cost, thus being very attractive for the analysis of global statistical properties of targeted populations.

The simulations run here with the two methods have in common the same initial conditions, so that any difference in the galaxy and black hole populations and their cosmological evolution is due to the specific prescriptions used in the two models for the evolution of the baryons and the growth of black holes.

We found that some of the predictions of the hydrodynamical simulations are resolution dependent, which is expected, considering the large softening length necessary to simulate relatively-large cosmological boxes. Still, the agreement between the predictions of the hydrodynamical simulations for the high-mass end of the black hole mass function, the quasar luminosity function and the $M_{\text{BH}} - \sigma_*$ in the local Universe are quite remarkable.

Interestingly, the predicted redshift evolution of the black hole population is quite different in the two approaches: in the hydrodynamical simulations a significant fraction of the mass function is already formed by $z = 5$, and the subsequent evolution is milder than in the semi-analytic model. Powerful quasars have been observed at $z = 6$, and these observations set important constraints on the number of very massive black holes that have already to be in place when the Universe was still so young.

Having used the same initial conditions for the hydrodynamical simulations and the dark matter simulation that constitute the back bone of the semi-analytic model, we will be able to compare directly the evolution of individual objects, thus isolating the physical processes that lead to differences in the global evolution of the black hole population and deriving important information on how each numerical method can be improved.

Chapter 6

Summary and outlook

Black holes are among the most interesting and fascinating objects in current astrophysical research. They are not only laboratories for studying fundamental physics theories, such as Einstein's General Relativity, but are also the powerful engines of extremely energetic observable phenomena. In fact, gas that falls onto black holes gets in part swallowed and in part accelerated away to far distances where it shines very brightly. The so-called quasars (or, more generally, Active Galactic Nuclei, AGN) are galaxies with a massive black hole at their center whose surrounding gas is falling onto it and being ejected so efficiently and rapidly that the light emitted in the accretion process can reach 10^{14} solar luminosities. The extra-galactic nature of these objects was recognized in the middle of last century, and, since then, a lot of effort has been invested in understanding the detailed physics connected to these extreme phenomena.

At the end of last century, a wider interest of the astrophysical community in accreting supermassive black holes (black holes up to few billion times the mass of the Sun) was triggered by the discovery that these massive objects are present at the center of nearly all nearby galaxies and that their masses are tightly connected with many physical properties of their host galaxies, such as mass and luminosity. These observations clearly suggested that massive black holes and their parent galaxies evolve "hand-in-hand": black hole growth might depend on the environment and, vice versa, the environment itself can be strongly shaped by the energy that a massive hole releases over its lifetime. Moreover, in the last decade very bright quasars powered by black holes with masses of the order of $10^9 M_{\odot}$ were discovered at redshifts up to $z \sim 6$. At the same time, X-ray observations showed that the space density of AGN peaks at $z \sim 2 - 3$, and that Active Nuclei with high X-ray luminosities are more common at higher redshift with respect to their low-luminosity counterparts. These observations suggest that supermassive black holes grow "anti-hierarchically": the more massive black holes were already in place at high redshift, and since then the accretion activity has shifted to smaller scales.

Understanding how this evolution of black hole growth relates to cosmic structure formation, how black hole accretion depends on the environment, and how black holes interact with their host galaxies, have become central questions in cosmology. Indeed, the importance of black hole evolution in our understanding of galaxy formation is now widely recognized, to the extent that many major future instruments (from radio to X-rays) will be partly devoted to the observation of distant AGN, promising to unveil details of the first population of accreting black holes and their environment, and to offer unprecedented data that can be compared with theoretical predictions.

On the theoretical side, a lot of progress has been achieved in the last several years, thanks to constantly improving models for the small-scale physics of accreting black holes, as well as models

that follow simultaneously the cosmological evolution of dark matter structures and their embedded galaxies and black holes. Indeed, to explain the wealth of observational data available and to make predictions for future observations, theorists need to exploit all available techniques to develop and improve models for the birth and evolution of massive black holes, from the time when the first stars were formed to the Universe we see today. While much progress has been achieved, many details of the physics associated with black hole growth and its interaction with the host galaxy are still unknown. From the very origin of these massive objects to the details of how the energy released during active phases couples with and influences the interstellar medium, many aspects of black hole behavior and their interaction with the host galaxies need to be explored further. A long-standing question is what triggers black hole accretion. The energetics associated with bright quasars can be explained with supermassive black holes accreting tens of solar masses per year. The Schwarzschild radius of a black hole, and even its gravitational radius of influence, are many orders of magnitude smaller than typical galactic scales: for efficient accretion to take place, there must be physical processes able to channel the gas present in the interstellar medium from galaxy scales down to the very nuclear regions. Galaxy mergers are among the processes that could trigger instabilities in a galaxy and induce a flow of gas towards the center. Indeed, simulations of galaxy mergers have shown that during those processes gas is funnelled to the nucleus of the merger remnants. The same processes are also able to trigger starbursts and the formation of spheroids, as seen in simulations and also confirmed observationally by the morphologically-disturbed appearance of starburst galaxies.

The objective of this thesis has been to explore the role of mergers in triggering efficient black hole accretion using different numerical methods and statistical tools, complementing and extending previous work on this subject.

In Chapter 2 we presented an extension of the semi-analytic model for galaxy formation developed at the MPA. This model combines the output of a large dark-matter simulation, the Millennium Simulation, with analytical prescriptions to describe the baryonic physics. One assumption of the model is that black hole accretion is triggered during galaxy mergers and the extension presented in this chapter was developed to describe the emission of accreting black holes. In comparing the predictions of our simulations with recent observations of the global descriptors of the black hole and quasar populations, we tested at the same time the assumption of the merger-driven nature of active nuclei and various theoretical models for the lightcurve associated to individual accretion events. The good match between the predicted and the observed properties of the black hole population, such as the mass function and scaling relations, lends support to the assumption that efficient black hole accretion is merger-driven. Moreover, comparing our predictions with the observed redshift evolution of the quasar luminosity function, we found that a substantial fraction of the available gas has to be accreted at rates close to the Eddington limit, but a “quiescent” accretion phase is necessary to describe the faint-end of the luminosity function.

In Chapter 3 the same models were tested using clustering analysis. Clustering is a very important statistical tool to study the spatial distribution of objects and to infer the type of environment in which they reside. Clustering analysis can also provide information on quasar lifetime, since, if quasars are strongly clustered, they must be hosted by rare objects, and therefore their time of activity must be long to account for the total abundance observed. We found that, in agreement with observations, the two-point correlation function of our simulated AGN can be approximated by a single power-law in the range $0.5 \lesssim r \lesssim 20 h^{-1} \text{Mpc}$. The bias between AGN and the dark matter is a strong function of redshift, but, at a given epoch, it is approximately

constant in the range $1.0 \lesssim r \lesssim 20 h^{-1}\text{Mpc}$. The redshift evolution of the bias is consistent with the redshift evolution of dark matter haloes in the mass range $10^{12} - 10^{13} h^{-1} M_{\odot}$, suggesting that quasars are always hosted by haloes in this mass range. Since bright quasars are always black holes accreting close to the Eddington limit, we found that the results for the clustering of bright AGN are independent of the specific light curve model assumed. Our results for the clustering of bright optical quasars are in very good agreement with recent observations at all redshifts. Since the merger episodes that trigger quasar activity are, in our modeling procedure, connected to the mergers of the dark matter haloes, clustering statistics depend strongly on the positions of halo mergers, which are directly predicted in the Millennium Simulation. Our clustering analysis therefore does not depend significantly on the parameters used to describe baryonic physics, and therefore should be regarded as a genuine model prediction. The good match between our predictions and the observed quasar clustering lends further support to the assumption of the merger-driven nature of quasars.

Chapter 4 was devoted to the analysis of the significance of the *merger bias*. Such an effect, if present, could lead to an incorrect interpretation of the clustering properties of observed quasars. Dark matter haloes (and galaxies) are, in fact, biased tracers of the underlying dark matter distribution, with a bias that depends primarily on halo mass. However, if recently merged objects do not cluster in the same way as other objects with the same mass, then the observed quasar clustering cannot be used to infer the type of environment quasars reside in (assuming that quasar activity is connected to halo mergers). The strength of any such merger bias was studied using the halo population simulated with the Millennium. We found that recently-merged haloes do not show significant excess clustering when compared to other haloes of similar mass. A similar result was found analyzing the merger bias for recently merged galaxies and quasars as modeled with the semi-analytical approach.

Finally, in Chapter 5, we showed some preliminary comparisons of the evolution of the black hole and the quasar populations simulated with our semi-analytic model for galaxy formation, and with hydrodynamic simulations that directly follow the baryonic physics. Such direct comparison between different numerical methods is extremely important for a full understanding of the limitations and advantages of each. Despite some resolution-dependencies, we found that hydrodynamical simulations can describe well the population of the most massive black holes in the local universe. The redshift evolution of the black hole mass function and luminosity function from the hydrodynamical and the semi-analytic simulations are quite different, however and, in the near future, we will explore in detail the origin of these differences by following the history of individual objects when simulated with the two methods.

Our analysis supports the assumption that galaxy mergers are the primary triggering mechanism for efficient black hole accretion. However, other processes (such as galaxy disk instabilities and recycling of gas from stellar evolution) could contribute to the growth of massive holes, and thus activate luminous phases in galaxies having entirely different properties than the ones expected for merger remnants (e.g., Seyfert galaxies). It is thus necessary to include these processes in cosmological models to understand their relative importance, and their evolution with cosmic time. Analysis of the evolution of scaling relations and of the properties of galaxies hosting AGN triggered by different physical processes could provide important indicators of the relative importance of different triggering mechanisms, and make predictions for future observations. Spatial clustering (also at small scales) can be further exploited to study AGN environments and can also be compared directly with the clustering of different classes of galaxies.

The upcoming new generation of observational facilities makes this a very exciting time to

work on theoretical models for the co-evolution of black holes and galaxies. Future X-rays, optical and near-IR surveys (such as eROSITA, PAN-STARRS, VST and VISTA) will be able to detect quasars with a wide range in luminosity, providing information on the faint-end of the quasar luminosity function, important as diagnostic for hydrodynamical simulations. Also, the observation of many more quasars at high redshifts will better constrain the redshift evolution of the population. Information at different wavelengths will be important to test models of growth, light curves and obscuration.

ALMA (mm and sub-mm) and JWST (Infrared) will open new windows to observe high redshift galaxies. The main properties of these objects (such as star formation rates, dust and gas content) can be compared with predictions from galaxy formation models. The simultaneous estimates of black hole masses through optical and near-IR emission lines and host galaxy masses with ALMA, will provide observational estimates for the evolution of the scaling relations between black holes and their host galaxies, such as the $M_{\text{BH}} - \sigma_*$. Moreover, IXO (X-rays) will be able to directly observe AGN fueling and feedback processes. Such observations and direct comparisons with theoretical predictions will be essential to understand the origin of massive black holes, the mechanisms that trigger black hole accretion and the role of stars and accreting black holes in the reionization of the Universe.

The combination of constantly more sophisticated numerical models and these future observations will certainly lead to important breakthroughs in the next few years in our understanding the formation and evolution of black holes, as well as their interaction with the environment.

Appendix A

Black hole accretion

In this appendix we introduce basic concepts of accretion physics, useful for the present thesis. We refer to Frank et al. (2002) for a detailed review on this subject.

A.1 Eddington Luminosity

The *Eddington limit* defines the equilibrium point between the outward radiation force and the inward gravitational force in an accreting object. The Eddington limit is derived assuming that the accretion is steady and spherically symmetric, and that the accreting material is ionized hydrogen. In this framework, the gravitational force that pulls electron and proton pairs towards the central object is given by:

$$F_{\text{in}} = \frac{G M_{\text{BH}} (m_p + m_e)}{r^2} \sim \frac{G M m_p}{r^2}, \quad (\text{A.1})$$

where m_p and m_e are the proton and electron mass, respectively, and $m_p \gg m_e$.

In the opposite direction, radiation exerts an outward force on the free electrons given by:

$$F_{\text{out}} = \frac{S \sigma_T}{c} = \frac{L \sigma_T}{4\pi r^2 c} \quad (\text{A.2})$$

where S is the radiant energy flux, σ_T is the Thomson cross-section and $L = 4\pi r^2$ the luminosity of the source. Despite having a much smaller cross-section, protons will be dragged outwards together with the electrons due to Coulomb electrostatic forces.

The net force on the electron-proton pairs is then:

$$F_{\text{tot}} = \frac{G M m_p}{r^2} - \frac{L \sigma_T}{4\pi r^2 c}. \quad (\text{A.3})$$

The luminosity at which radiative pressure and gravitational attraction are balanced is then:

$$L_{\text{Edd}} = \frac{4\pi G M_{\text{BH}} m_p c}{\sigma_T} \sim 1.3 \times 10^{46} \left(\frac{M_{\text{BH}}}{10^8 M_{\odot}} \right) \text{ erg/s}. \quad (\text{A.4})$$

At higher luminosities, the radiation pressure would sweep out the infalling material, thus halting further accretion.

A.1.1 The radiative efficiency

If R is the radius of an accreting object of mass M , the energy produced by the accretion of a mass m is given by the potential energy:

$$\Delta E_{\text{acc}} = \frac{G M m}{R}. \quad (\text{A.5})$$

Differentiating over time, the corresponding luminosity is given by:

$$L_{\text{acc}} = \frac{G \dot{M} m}{R}. \quad (\text{A.6})$$

Since a black hole does not have a solid surface, part of the mass will fall into the event horizon, and therefore not all the gravitational potential energy is converted into radiation. The *radiative efficiency* ϵ is a parameter that indicates which fraction of the accreted rest mass energy is converted into radiation:

$$L_{\text{acc}} = \epsilon \frac{G \dot{M} m}{R} = \epsilon \dot{M} c^2, \quad (\text{A.7})$$

where R has been substituted by the radius of the black hole, the event horizon, which is given by the Schwarzschild radius $R_S = 2GM_{\text{BH}}/c^2$.

The closest point to the black hole from which energy can be extracted is the *innermost stable circular orbit* (ISCO). The maximum radiative efficiency is related to R_{ISCO} as:

$$\epsilon \sim \frac{G M m / 2 R_{\text{ISCO}}}{m c^2}. \quad (\text{A.8})$$

For a non-rotating black hole, the last stable orbit is given by:

$$R_{\text{ISCO}} = \frac{6 G M}{c^2}. \quad (\text{A.9})$$

Relativistic calculations lead to a maximum value $\epsilon \sim 0.06$ for a non-rotating black hole. If the black hole is rotating, the value of the last stable orbit decreases, and the maximum possible radiative efficiency is higher. For a maximally-rotating black hole, $\epsilon \sim 0.4$. Statistical arguments connected to the redshift evolution of the quasar luminosity function indicate an average radiative efficiency across cosmic time of $\epsilon \sim 0.1$ (e.g., Soltan 1982).

A.1.2 The *e-folding* time

If \dot{M} is the mass-flow rate, the black hole grows at the rate $\dot{M}_{\text{BH}} = (1 - \epsilon) \dot{M}$. Combining equation A.4 with A.7:

$$\frac{\dot{M}_{\text{BH}}}{M_{\text{BH}}} = \frac{4\pi G m_p}{c \sigma_T} \frac{1 - \epsilon}{\epsilon}. \quad (\text{A.10})$$

The right-hand-side of the above equation is the inverse of the so-called *Salpeter* time, $t_s = \epsilon/(1 - \epsilon) 4.5 \times 10^8 \text{yr}$, which is the time it would take a black hole emitting at the Eddington Luminosity to radiate away all of its rest mass. But, integrating equation A.10, one gets:

$$M_{\text{BH}} = M_{\text{BH},0} e^{t/t_s}, \quad (\text{A.11})$$

so t_s is also equivalent to the *e-folding* time, that is the time it would take a black hole to grow exponentially by a factor of e .

If the black hole is emitting at a fraction f_{Edd} of the Eddington Luminosity, the *e-folding* time is given by $t_{ef} = t_s/f_{\text{Edd}}$.

A.2 Black Hole accretion models

A.2.1 Thin disk

Quasars and high-luminosity AGN are powered by supermassive black holes accreting mass at high rates (up to tens of solar masses per year), and which can efficiently radiate away energy. Sitting on the accretion disk, material falls inwards by losing angular momentum through viscous processes. If energy can be radiated away efficiently, the gas cools efficiently, the sound speed c_s is much less than the keplerian velocity $v_K = (GM/R)^{1/2}$ and the accretion disk is thin (the vertical height H is much less than the radius of the disk R) (Shakura & Sunyaev 1973).

These are the conditions in which black holes radiate at high Eddington fractions, and power bright AGN.

A.2.2 Thick disk

If the gas is unable to efficiently radiate away the energy extracted from loss of angular momentum, this energy remains in the gas. In this scenario, the pressure of the gas is high, and so is the sound speed, which can become comparable to the Keplerian velocity ($c_s \sim v_K$) making the disk is thick, with $H \sim R$. Introduced by Narayan & Yi (1994), such *Advection-dominated accretion flows* (ADAFs), are able to describe properties of low-luminosity AGN, whose accretion rates and radiative efficiencies are much lower than in the thin-disk case.

A.2.3 Bondi accretion

Bondi accretion describes the case of an object with spherically-symmetric accretion flow.

In 1939, Hoyle & Lyttleton derived the accretion rate for the case of a star moving at a steady speed through an infinite gas cloud (Hoyle & Lyttleton 1939):

$$\dot{M} = \frac{4 \pi G^2 M^2 \rho_\infty}{v_\infty^3}, \quad (\text{A.12})$$

where M is the mass of the accreting object, ρ_∞ and v_∞ are the density and velocity of the gas at infinity. The Hoyle & Lyttleton formulation defines a characteristic value for the impact parameter ($2GM/v_\infty^2$), below which material is accreted with the above mass flux.

Bondi (1952) studied the case of a point mass with spherically-symmetric accretion. In this case, the characteristic radius is given by $r_B = GM/c_s^2$: inside this radius, the gas is supersonic and in free-fall.

A generalized formula for the accretion rate is then given by:

$$\dot{M} = \frac{4 \pi G^2 M^2 \rho_\infty}{c_\infty^3 + v_\infty^3}, \quad (\text{A.13})$$

which gives the solution above if $c_s \ll v_\infty$. We refer to Edgar (2004) and Frank et al. (2002) for full descriptions of the Bondi-Hoyle-Lyttleton accretion.

Appendix B

Clustering statistics

B.1 Introduction to clustering statistics

According to the *theory of biased galaxy formation*, galaxies do not follow the distribution of the underlying dark matter (Kaiser 1984; Bardeen et al. 1986). Galaxies, in fact, form in the high peaks of the dark matter density field, and, at large scales, the mass fluctuations can be derived from galaxy clustering only if the *bias* parameter is known, defined as:

$$b_{G,DM}(r) \equiv \sqrt{\frac{\xi_G(r)}{\xi_{DM}(r)}}, \quad (\text{B.1})$$

where $\xi_G(r)$ and $\xi_H(r)$ are the two point correlation function of the galaxy population and the dark matter, respectively. The *two-point spatial autocorrelation function* $\xi(r)$ for a given class of objects is defined as the excess probability for finding a pair at a distance r , each in the volume elements dV_1 and dV_2 (e.g., Peacock 1999):

$$dP = n^2 [1 + \xi(r)] dV_1 dV_2, \quad (\text{B.2})$$

where n is the average number density of the set of objects under consideration.

In the scale range between few tens of kpc and few tens of Mpc, for most classes of objects $\xi(r)$ can be described by a single power-law:

$$\xi(r) = \left(\frac{r}{r_0}\right)^{-\gamma}, \quad (\text{B.3})$$

where r_0 is the *correlation length* which is, by definition, the scale at which the two-point correlation function is equal to unity: $\xi(r_0) \equiv 1$.

In Figure B.1 the two-point galaxy correlation function from the Millennium Simulation is compared with observational data. In the same figure, also the correlation function of the dark matter is shown. Clearly, while the galaxy correlation function is a good power-law over a wide range of scales (up to $\sim 20 h^{-1}$ Mpc), the dark matter has a characteristic “bump” below $1 h^{-1}$ Mpc, inside the so-called 1-halo term¹ Springel et al. (2005c).

¹The two-point correlation function can be divided in two components: at small scales, it indicates the correlation of matter within individual dark matter haloes, whereas at large scales it gives information on the correlation power between separate

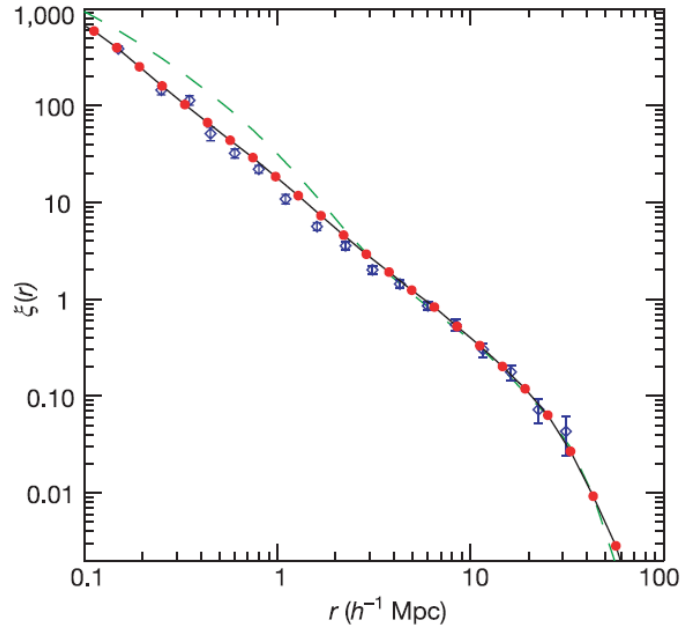


Figure B.1: Galaxy two-point correlation function from the Millennium Simulation (red filled circles), compared with the one of galaxies observed with the 2dFGRS survey (blue diamonds). The green dashed line shows the correlation function of the underlying dark matter. Figure from Springel et al. (2005c).

A statistically-accurate calculation of the two-point correlation function requires large samples. If the number density of the objects into consideration is small, an estimate of the clustering power of a population can also be derived using the cross-correlation function, which calculates the number of pairs from two sets of objects. If $\xi_{G,R}(r)$ is the cross-correlation function between galaxies and a reference population (larger in size), the bias between the galaxies and the dark matter is then:

$$b_{G,DM}(r) \equiv \frac{1}{b_{R,DM}(r)} \frac{\xi_{G,R}(r)}{\xi_{DM}(r)}, \quad (\text{B.4})$$

where $b_{R,DM}(r)$ is the bias (relative to the dark matter) of the population used as reference in the cross-correlation analysis.

B.2 Galaxy and halo clustering

As mentioned above, galaxies are biased tracers of the dark matter distribution. Observations have shown that the bias is a function of galaxy properties, such as color and luminosity. For example, analyzing galaxies observed with the Sloan Digital Sky Survey (York et al. 2000) and the 2 Degree Field Galaxy Redshift Survey (Colless et al. 2001), various groups found that more luminous galaxies are more strongly clustered than less luminous ones, and red galaxies are more strongly clustered than blue ones (e.g., Norberg et al. 2001; Zehavi et al. 2005; Li et al. 2006a).

haloes. The division between these two regimes is at $1 h^{-1}$ Mpc.

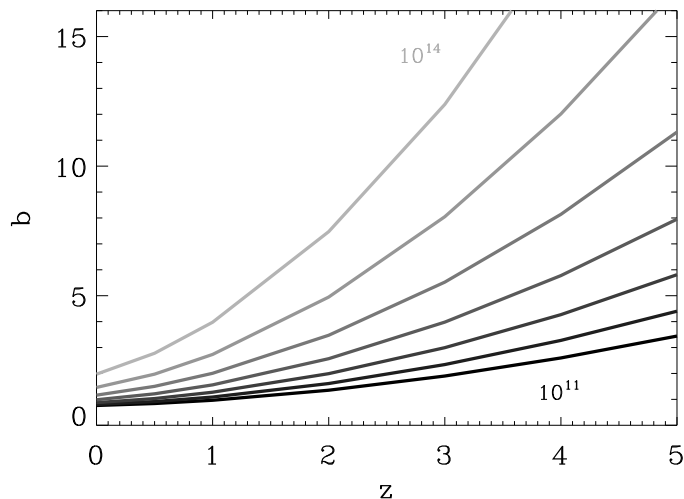


Figure B.2: The redshift evolution of the dark matter halo bias in the analytical formulation of Sheth et al. (2001), for the cosmology of the Millennium Simulation, and for various halo masses, from $10^{11}h^{-1} M_{\odot}$ to $10^{14}h^{-1} M_{\odot}$, with mass differences of 0.5 dex.

Similarly, the clustering of dark matter haloes depends on the halo physical properties. Halo bias can be estimated analytically or through dark matter simulations (e.g., Mo & White 1996; Sheth et al. 2001; Jing 1998), and it depends primarily on mass, as is shown in Figure B.2, where the bias for dark matter haloes of various masses is shown as a function of redshift, calculated using the formulation of Sheth et al. (2001) and the cosmological parameters of the Millennium Simulation. Clearly, the bias is a strong function of mass and redshift. A comparison between the clustering power observed for target classes of objects and the theoretical predictions for the halo bias gives information on the type of environment in which the selected objects live. While the value of halo bias mainly depends on mass, in recent years less trivial dependences have been found. Gao et al. (2005) discovered an “assembly bias”, where later forming haloes with mass $M < M_*$ ² are less clustered than typical haloes of the same mass. Wechsler et al. (2006) showed that less concentrated haloes more massive than the non-linear mass scale are instead more biased than average.

² M_* is the mass for which $\sigma(M_*) = 1.69/D(z)$, where $D(z)$ is the growth factor.

Acknowledgements

To Simon and Volker goes my first and sincere, thank you.

Simon, I want to express here all my admiration for your knowledge, memory and intuition. You are not always an easy-to-please supervisor, but your criticisms have always been constructive challenges, of which I am really grateful! I deeply hope I will have in the future other chances to learn more from you.

Volker, your skills, efficiency and ability at multi-tasking will never stop impressing me! Thank you for your support and supervision, and for saying always the right thing, being it about astrophysics or about life.

To all MPA, from the students to the four directors. In particular, thanks to everyone who puts the lively and friendly scientific atmosphere of the institute above all.

To the *amochette*: Caroline, Margarita, Mona, Payel and Shy. You have been my family here.

To Andrea, for the many discussions on black holes, the constant encouragement, and for sharing the logarithmic view of an AGN!

To the many people that, at different times, have shared friendship and physics: Gabriella, Eric, Andre, Antonella, Benedetta, Klaus, Dimitri, Ben, Mattia, Marco, Stefano, Stuart, Roderik, Francesco, Mike, Eyal, Carlos and Raul.

Thanks to the GalileoMobile, to the people that made it possible and to the many kids and teachers that welcomed us in their schools. This project renewed my enthusiasm for life and for science.

To Anna & Brunetto
and, last and least, a little thanks to myself...

Curriculum vitae

Personal data

Silvia Bonoli
Max Planck Institute for Astrophysics
Karl Schwarzschild Str. 1
85748 Garching
Germany

bonoli@mpa-garching.mpg.de
phone: +49 (0)89 300002240
fax: +49 (0)89 300002235

Education and Research Experience

2006-2010 PhD - Max Planck Institute for Astrophysics, Garching

PhD Thesis: *The role of galaxy mergers in the evolution of supermassive black holes*

Supervisors: Prof. Volker Springel and Prof. Simon D.M. White

2004-2006 MSc - Department of Astronomy & Astrophysics, University of Toronto

Research project: *Halo stochasticity in global clustering analysis*

Supervisor: Prof. Ue-Li Pen

Research project: *Binary black holes in merging elliptical galaxies*

Supervisor: Prof. John Dubinski

1998-2003 Laurea in Astronomy - University of Bologna

Thesis: *The fundamental plane of elliptical galaxies: effects of rotation*

Supervisor: Prof. Luca Ciotti

Final grade: 110 out of 110 with distinction

Research Interests

Theoretical cosmology and galaxy formation. Joint evolution of black holes and galaxies. Clustering of dark matter haloes, galaxies and quasars. Galactic dynamics. Evolution of black hole binaries. Seed black holes.

Publication list

Refereed Publications

On merger bias and the clustering of quasars

Bonoli S., Shankar F., White S.D.M., Springel V., Wyithe J.S.B.
MNRAS, in press

Modeling the cosmological co-evolution of supermassive black holes and galaxies II.: the clustering of quasars and their dark environment.

Bonoli S., Marulli F., Springel V., White S.D.M., Branchini E., Moscardini L.
2009, MNRAS, 396, 423

The spatial distribution of X-ray selected AGN in the Chandra deep fields: a theoretical perspective.

Marulli F., Bonoli S., Branchini E., Gilli R., Moscardini L., Springel V.
2009, MNRAS, 396, 1404

Halo stochasticity in global clustering analysis.

Bonoli S., Pen U.L.
2009, MNRAS, 396, 1610

Modeling the cosmological co-evolution of supermassive black holes and galaxies I.: BH scaling relations and the AGN luminosity function.

Marulli F., Bonoli S., Branchini E., Moscardini L., Springel V.
2008, MNRAS, 385, 1846

The contribution of rotational velocity to the FP of elliptical galaxies.

Riciputi A., Lanzoni B., Bonoli S., Ciotti L.
2005, A&A, 443, 133

Bibliography

- Adelberger, K. L. & Steidel, C. C. 2005, *ApJ*, 630, 50
- Akritas, M. G. & Bershad, M. A. 1996, *ApJ*, 470, 706
- Alvarez, M. A., Wise, J. H., & Abel, T. 2008, in *American Institute of Physics Conference Series*, Vol. 990, First Stars III, ed. B. W. O'Shea & A. Heger, 432–434
- Angulo, R. E., Baugh, C. M., & Lacey, C. G. 2008, *MNRAS*, 387, 921
- Angulo, R. E., Lacey, C. G., Baugh, C. M., & Frenk, C. S. 2009, *MNRAS*, 399, 983
- Babbedge, T. S. R. et al. 2006, *MNRAS*, 370, 1159
- Baes, M., Buyle, P., Hau, G. K. T., & Dejonghe, H. 2003, *MNRAS*, 341, L44
- Bajtlik, S., Duncan, R. C., & Ostriker, J. P. 1988, *ApJ*, 327, 570
- Bardeen, J. M., Bond, J. R., Kaiser, N., & Szalay, A. S. 1986, *ApJ*, 304, 15
- Barger, A. J., Cowie, L. L., Capak, P., et al. 2003a, *ApJL*, 584, L61
- Barger, A. J. et al. 2003b, *AJ*, 126, 632
- Barkana, R. & Loeb, A. 2001, *Phys. Rep.*, 349, 125
- Barnes, J. E. 1988, *ApJ*, 331, 699
- Barnes, J. E. & Hernquist, L. 1996, *ApJ*, 471, 115
- Barnes, J. E. & Hernquist, L. E. 1991, *ApJL*, 370, L65
- Beckmann, V., Soldi, S., Shrader, C. R., Gehrels, N., & Prodit, N. 2006, *ApJ*, 652, 126
- Begelman, M. C. 2010, *MNRAS*, 402, 673
- Begelman, M. C., Volonteri, M., & Rees, M. J. 2006, *MNRAS*, 370, 289
- Bennert, N., Canalizo, G., Jungwiert, B., et al. 2008, *ApJ*, 677, 846
- Benson, A. J., Bower, R. G., Frenk, C. S., et al. 2003, *ApJ*, 599, 38
- Best, P. N., Kauffmann, G., Heckman, T. M., et al. 2005, *MNRAS*, 362, 25
- Binney, J. & Tabor, G. 1995, *MNRAS*, 276, 663
- Binney, J. & Tremaine, S. 1987, *Galactic dynamics* (Princeton, NJ, Princeton University Press, 1987, 747 p.)

- Bird, J., Martini, P., & Kaiser, C. 2008, *ApJ*, 676, 147
- Blandford, R. D. & McKee, C. F. 1982, *ApJ*, 255, 419
- Bond, J. R., Arnett, W. D., & Carr, B. J. 1984, *ApJ*, 280, 825
- Bondi, H. 1952, *MNRAS*, 112, 195
- Bondi, H. & Hoyle, F. 1944, *MNRAS*, 104, 273
- Bongiorno, A. et al. 2007, preprint, astro-ph/0704.1660, 704
- Bonoli, S., Marulli, F., Springel, V., et al. 2009, *MNRAS*, 396, 423
- Bromm, V. & Loeb, A. 2003, *ApJ*, 596, 34
- Brown, M. J. I. et al. 2006, *ApJ*, 638, 88
- Brown, W. R., Geller, M. J., & Kenyon, S. J. 2009, *ApJ*, 690, 1639
- Brüggen, M. & Kaiser, C. R. 2002, *Nature*, 418, 301
- Bullock, J. S., Kolatt, T. S., Sigad, Y., et al. 2001, *MNRAS*, 321, 559
- Carswell, R. F., Whelan, J. A. J., Smith, M. G., Boksenberg, A., & Tytler, D. 1982, *MNRAS*, 198, 91
- Cattaneo, A. & Bernardi, M. 2003, *MNRAS*, 344, 45
- Cattaneo, A., Blaizot, J., Devriendt, J., & Guiderdoni, B. 2005, *MNRAS*, 364, 407
- Cavaliere, A. & Vittorini, V. 2002, *ApJ*, 570, 114
- Churazov, E., Sunyaev, R., Forman, W., & Böhringer, H. 2002, *MNRAS*, 332, 729
- Ciotti, L. & Ostriker, J. P. 2007, *ApJ*, 665, 1038
- Cirasuolo, M., Shankar, F., Granato, G. L., De Zotti, G., & Danese, L. 2005, *ApJ*, 629, 816
- Coil, A. L., Hennawi, J. F., Newman, J. A., Cooper, M. C., & Davis, M. 2007, *ApJ*, 654, 115
- Colberg, J. M. & di Matteo, T. 2008, *MNRAS*, 387, 1163
- Cole, S. & Kaiser, N. 1989, *MNRAS*, 237, 1127
- Colless, M. et al. 2001, *MNRAS*, 328, 1039
- Comastri, A. 2004, in *Astrophysics and Space Science Library*, Vol. 308, *Astrophysics and Space Science Library*, ed. A. J. Barger, 245–+
- Conroy, C. & Wechsler, R. H. 2009, *ApJ*, 696, 620
- Cowie, L. L., Barger, A. J., Bautz, M. W., Brandt, W. N., & Garmire, G. P. 2003, *ApJL*, 584, L57
- Cowie, L. L. & Binney, J. 1977, *ApJ*, 215, 723
- Cox, T. J. 2004, Ph.D. Thesis, University of California, Santa Cruz
- Cox, T. J., Primack, J., Jonsson, P., & Somerville, R. S. 2004, *ApJL*, 607, L87

- Cristiani, S. et al. 2004, *ApJL*, 600, L119
- Croom, S. M., Boyle, B. J., Shanks, T., et al. 2005, *MNRAS*, 356, 415
- Croom, S. M., Richards, G. T., Shanks, T., et al. 2009, *MNRAS*, 399, 1755
- Croom, S. M., Smith, R. J., Boyle, B. J., et al. 2004, *MNRAS*, 349, 1397
- Croton, D. J. 2006, *MNRAS*, 369, 1808
- Croton, D. J. et al. 2006, *MNRAS*, 365, 11
- da Ângela, J., Shanks, T., Croom, S. M., et al. 2008, *MNRAS*, 383, 565
- De Lucia, G. & Blaizot, J. 2007, *MNRAS*, 375, 2
- De Lucia, G., Kauffmann, G., & White, S. D. M. 2004, *MNRAS*, 349, 1101
- De Lucia, G., Springel, V., White, S. D. M., Croton, D., & Kauffmann, G. 2006, *MNRAS*, 366, 499
- de Vaucouleurs, G. 1948, *Annales d'Astrophysique*, 11, 247
- Degraf, C., Di Matteo, T., & Springel, V. 2010, *MNRAS*, 402, 1927
- Di Matteo, T., Colberg, J., Springel, V., Hernquist, L., & Sijacki, D. 2008, *ApJ*, 676, 33
- Di Matteo, T., Springel, V., & Hernquist, L. 2005, *Nature*, 433, 604
- Dotti, M., Volonteri, M., Perego, A., et al. 2010, *MNRAS*, 402, 682
- Edgar, R. 2004, *New Astronomy Review*, 48, 843
- Efstathiou, G. 1992, *MNRAS*, 256, 43P
- Efstathiou, G. & Rees, M. J. 1988, *MNRAS*, 230, 5P
- Eisenhauer, F., Genzel, R., Alexander, T., et al. 2005, *ApJ*, 628, 246
- Elvis, M. et al. 1994, *ApJS*, 95, 1
- Enoki, M., Nagashima, M., & Gouda, N. 2003, *PASJ*, 55, 133
- Escala, A. 2007, *ApJ*, 671, 1264
- Escala, A., Larson, R. B., Coppi, P. S., & Mardones, D. 2004, *ApJ*, 607, 765
- Fabian, A. C. & Nulsen, P. E. J. 1977, *MNRAS*, 180, 479
- Fan, X., Narayanan, V. K., Lupton, R. H., et al. 2001a, *AJ*, 122, 2833
- Fan, X. et al. 2001b, *AJ*, 121, 54
- Ferrarese, L. 2002, *ApJ*, 578, 90
- Ferrarese, L. & Ford, H. 2005, *Space Science Reviews*, 116, 523
- Ferrarese, L. & Merritt, D. 2000, *ApJL*, 539, L9
- Fine, S., Croom, S. M., Miller, L., et al. 2006, *MNRAS*, 373, 613

- Fontanot, F., Cristiani, S., Monaco, P., et al. 2007, *A&A*, 461, 39
- Fontanot, F., Monaco, P., Cristiani, S., & Tozzi, P. 2006, *MNRAS*, 373, 1173
- Frank, J., King, A., & Raine, D. J. 2002, *Accretion Power in Astrophysics: Third Edition*, ed. Frank, J., King, A., & Raine, D. J.
- Furlanetto, S. R. & Kamionkowski, M. 2006, *MNRAS*, 366, 529
- Gao, L., Springel, V., & White, S. D. M. 2005, *MNRAS*, 363, L66
- Gao, L. & White, S. D. M. 2007, *MNRAS*, 377, L5
- Gebhardt, K., Bender, R., Bower, G., et al. 2000, *ApJL*, 539, L13
- Genel, S., Genzel, R., Bouché, N., Naab, T., & Sternberg, A. 2009, *ApJ*, 701, 2002
- Genzel, R. & Karas, V. 2007, in *IAU Symposium, Vol. 238, IAU Symposium*, ed. V. Karas & G. Matt, 173–180
- Georgakakis, A., Coil, A. L., Laird, E. S., et al. 2009, *MNRAS*, 397, 623
- Ghez, A. M., Salim, S., Hornstein, S. D., et al. 2005, *ApJ*, 620, 744
- Gillessen, S., Eisenhauer, F., Bartko, H., et al. 2010, *ArXiv e-prints*
- Gilli, R., Comastri, A., & Hasinger, G. 2007, *A&A*, 463, 79
- Gilli, R., Daddi, E., Zamorani, G., et al. 2005, *A&A*, 430, 811
- Gilli, R., Zamorani, G., Miyaji, T., et al. 2009, *A&A*, 494, 33
- Gnedin, N. Y. 2000, *ApJ*, 542, 535
- Gottlöber, S., Kerscher, M., Kravtsov, A. V., et al. 2002, *A&A*, 387, 778
- Graham, A. W. & Driver, S. P. 2007, *MNRAS*, 380, L15
- Graham, A. W., Erwin, P., Caon, N., & Trujillo, I. 2001, *ApJL*, 563, L11
- Granato, G. L., De Zotti, G., Silva, L., Bressan, A., & Danese, L. 2004, *ApJ*, 60
- Grazian, A., Cristiani, S., D’Odorico, V., Omizzolo, A., & Pizzella, A. 2000, *AJ*, 119, 2540
- Grazian, A., Negrello, M., Moscardini, L., et al. 2004, *AJ*, 127, 592
- Haehnelt, M. G., Natarajan, P., & Rees, M. J. 1998, *MNRAS*, 300, 817
- Haehnelt, M. G. & Rees, M. J. 1993, *MNRAS*, 263, 168
- Haiman, Z. & Hui, L. 2001, *ApJ*, 547, 27
- Haiman, Z. & Loeb, A. 1998, *ApJ*, 503, 505
- Haiman, Z. & Menou, K. 2000, *ApJ*, 531, 42
- Hao, L. et al. 2005, *AJ*, 129, 1795
- Häring, N. & Rix, H.-W. 2004, *ApJL*, 604, L89

- Hasinger, G., Miyaji, T., & Schmidt, M. 2005, *A&A*, 441, 417
- Hatziminaoglou, E., Mathez, G., Solanes, J.-M., Manrique, A., & Salvador-Solé, E. 2003, *MNRAS*, 343, 692
- Heckman, T. M., Kauffmann, G., Brinchmann, J., et al. 2004, *ApJ*, 613, 109
- Heger, A. & Woosley, S. E. 2002, *ApJ*, 567, 532
- Hennawi, J. F. et al. 2006, *AJ*, 131, 1
- Hennawi, J. F. et al. 2009, *ArXiv e-prints*
- Hernquist, L. 1992, *ApJ*, 400, 460
- Hills, J. G. 1988, *Nature*, 331, 687
- Hoefl, M., Yepes, G., Gottlöber, S., & Springel, V. 2006, *MNRAS*, 371, 401
- Hopkins, P. F. & Hernquist, L. 2008, *arXiv:0809.3789*
- Hopkins, P. F., Hernquist, L., Cox, T. J., & Keres, D. 2007b, *ArXiv e-prints*, 706
- Hopkins, P. F., Hernquist, L., Cox, T. J., et al. 2006a, *ApJ*, 639, 700
- Hopkins, P. F., Hernquist, L., Cox, T. J., Robertson, B., & Krause, E. 2007a, preprint, *astro-ph/0701351*
- Hopkins, P. F., Hernquist, L., Martini, P., et al. 2005, *ApJL*, 625, L71
- Hopkins, P. F., Lidz, A., Hernquist, L., et al. 2007a, *ApJ*, 662, 110
- Hopkins, P. F., Richards, G. T., & Hernquist, L. 2007b, *ApJ*, 654, 731
- Hopkins, P. F., Robertson, B., Krause, E., Hernquist, L., & Cox, T. J. 2006b, *ApJ*, 652, 107
- Hoyle, F. & Lyttleton, R. A. 1939, in *Proceedings of the Cambridge Philosophical Society*, Vol. 35, *Proceedings of the Cambridge Philosophical Society*, 405–+
- Hunt, M. P., Steidel, C. C., Adelberger, K. L., & Shapley, A. E. 2004, *ApJ*, 605, 625
- Hutchings, J. B., Scholz, P., & Bianchi, L. 2009, *AJ*, 137, 3533
- Jahnke, K., Kuhlbrodt, B., & Wisotzki, L. 2004, *MNRAS*, 352, 399
- Jing, Y. P. 1998, *ApJL*, 503, L9+
- Jogee, S. 2006, in *Lecture Notes in Physics*, Berlin Springer Verlag, Vol. 693, *Physics of Active Galactic Nuclei at all Scales*, ed. D. Alloin, 143–+
- Johansson, P. H., Burkert, A., & Naab, T. 2009, *ApJL*, 707, L184
- Kaiser, N. 1984, *ApJL*, 284, L9
- Kaspi, S., Smith, P. S., Netzer, H., et al. 2000, *ApJ*, 533, 631
- Katz, N., Weinberg, D. H., & Hernquist, L. 1996, *ApJS*, 105, 19
- Kauffmann, G. 1996, *MNRAS*, 281, 475
- Kauffmann, G. & Haehnelt, M. 2000, *MNRAS*, 311, 576

- Kauffmann, G. & Haehnelt, M. G. 2002, *MNRAS*, 332, 529
- Kauffmann, G., Heckman, T. M., Tremonti, C., et al. 2003, *MNRAS*, 346, 1055
- Kauffmann, G., White, S. D. M., & Guiderdoni, B. 1993, *MNRAS*, 264, 201
- Kennefick, J. D., Djorgovski, S. G., & de Carvalho, R. R. 1995, *AJ*, 110, 2553
- Kennicutt, Jr., R. C. 1998, *ApJ*, 498, 541
- Kirkman, D. & Tytler, D. 2008, *MNRAS*, 391, 1457
- Kitzbichler, M. G. & White, S. D. M. 2007, *MNRAS*, 376, 2
- Koehler, T., Groote, D., Reimers, D., & Wisotzki, L. 1997, *A&A*, 325, 502
- Kolatt, T. S., Bullock, J. S., Somerville, R. S., et al. 1999, *ApJL*, 523, L109
- Kollmeier, J. A., Onken, C. A., Kochanek, C. S., et al. 2006, *ApJ*, 648, 128
- Komossa, S. 2006, *Memorie della Societa Astronomica Italiana*, 77, 733
- Kormendy, J. 2004, in *Coevolution of Black Holes and Galaxies*, ed. L. C. Ho, 1–+
- Kormendy, J. & Richstone, D. 1995, *ARA&A*, 33, 581
- Koushiappas, S. M., Bullock, J. S., & Dekel, A. 2004, *MNRAS*, 354, 292
- Koushiappas, S. M. & Zentner, A. R. 2006, *ApJ*, 639, 7
- Kravtsov, A. V., Gnedin, O. Y., & Klypin, A. A. 2004, *ApJ*, 609, 482
- La Franca, F. et al. 2005, *ApJ*, 635, 864
- Lamastra, A., Perola, G. C., & Matt, G. 2006, *A&A*, 449, 551
- Lemson, G. & Kauffmann, G. 1999, *MNRAS*, 302, 111
- Lemson, G. & Virgo Consortium, t. 2006, preprint, astro-ph/060801
- Li, C., Kauffmann, G., Heckman, T. M., White, S. D. M., & Jing, Y. P. 2008, *MNRAS*, 385, 1915
- Li, C., Kauffmann, G., Jing, Y. P., et al. 2006a, *MNRAS*, 368, 21
- Li, C., Kauffmann, G., Wang, L., et al. 2006b, *MNRAS*, 373, 457
- Li, Y., Hernquist, L., Robertson, B., et al. 2007, *ApJ*, 665, 187
- Lidz, A., Hopkins, P. F., Cox, T. J., Hernquist, L., & Robertson, B. 2006, *ApJ*, 641, 41
- Loeb, A. & Rasio, F. A. 1994, *ApJ*, 432, 52
- Lynden-Bell, D. 1969, *Nature*, 223, 690
- Madau, P. & Rees, M. J. 2001, *ApJL*, 551, L27
- Magorrian, J., Tremaine, S., Richstone, D., et al. 1998, *AJ*, 115, 2285
- Maior, U., Dolag, K., Ciardi, B., & Tornatore, L. 2007, *MNRAS*, 379, 963

- Makino, J. & Funato, Y. 2004, *ApJ*, 602, 93
- Malbon, R. K., Baugh, C. M., Frenk, C. S., & Lacey, C. G. 2007, *MNRAS*, 382, 1394
- Marconi, A. & Hunt, L. K. 2003, *ApJL*, 589, L21
- Marconi, A., Risaliti, G., Gilli, R., et al. 2004, *MNRAS*, 351, 169
- Martini, P. 2004, in *Coevolution of Black Holes and Galaxies*, ed. L. C. Ho, 169
- Martini, P. & Weinberg, D. H. 2001a, *ApJ*, 547, 12
- Martini, P. & Weinberg, D. H. 2001b, *ApJ*, 547, 12
- Marulli, F., Bonoli, S., Branchini, E., et al. 2009, ArXiv e-prints
- Marulli, F., Bonoli, S., Branchini, E., Moscardini, L., & Springel, V. 2008, *MNRAS*, 385, 1846
- Marulli, F., Branchini, E., Moscardini, L., & Volonteri, M. 2007, *MNRAS*, 375, 649
- Marulli, F., Crociani, D., Volonteri, M., Branchini, E., & Moscardini, L. 2006, *MNRAS*, 368, 1269
- Matute, I., La Franca, F., Pozzi, F., et al. 2006, *A&A*, 451, 443
- Mayer, L., Kazantzidis, S., & Escala, A. 2008, ArXiv e-prints
- McNamara, B. R. & Nulsen, P. E. J. 2007, *ARA&A*, 45, 117
- Merloni, A. 2004, *MNRAS*, 353, 1035
- Merloni, A., Bongiorno, A., Bolzonella, M., et al. 2010, *ApJ*, 708, 137
- Merloni, A., Rudnick, G., & Di Matteo, T. 2004, *MNRAS*, 354, L37
- Merritt, D. 2004, in *Coevolution of Black Holes and Galaxies*, ed. L. C. Ho, 263–+
- Mihos, J. C. & Hernquist, L. 1994, *ApJL*, 431, L9
- Mihos, J. C. & Hernquist, L. 1996, *ApJ*, 464, 641
- Milosavljević, M. & Merritt, D. 2003, *ApJ*, 596, 860
- Miyaji, T., Hasinger, G., & Schmidt, M. 2000, *A&A*, 353, 25
- Miyaji, T., Hasinger, G., & Schmidt, M. 2001, *A&A*, 369, 49
- Mo, H. J., Mao, S., & White, S. D. M. 1998, *MNRAS*, 295, 319
- Mo, H. J. & White, S. D. M. 1996, *MNRAS*, 282, 347
- Monaco, P., Fontanot, F., & Taffoni, G. 2007, *MNRAS*, 375, 1189
- Monaghan, J. J. 1992, *ARA&A*, 30, 543
- Moster, B. P., Somerville, R. S., Maulbetsch, C., et al. 2010, *ApJ*, 710, 903
- Myers, A. D., Brunner, R. J., Nichol, R. C., et al. 2007a, *ApJ*, 658, 85
- Myers, A. D., Brunner, R. J., Richards, G. T., et al. 2007b, *ApJ*, 658, 99

- Myers, A. D., Richards, G. T., Brunner, R. J., et al. 2008, *ApJ*, 678, 635
- Naab, T. & Burkert, A. 1999, in *Astronomical Society of the Pacific Conference Series*, Vol. 182, *Galaxy Dynamics - A Rutgers Symposium*, ed. D. R. Merritt, M. Valluri, & J. A. Sellwood, 477–+
- Nagar, N. M., Falcke, H., & Wilson, A. S. 2005, *A&A*, 435, 521
- Nandra, K., Laird, E. S., & Steidel, C. C. 2005, *MNRAS*, 360, L39
- Narayan, R. & Yi, I. 1994, *ApJL*, 428, L13
- Negroponte, J. & White, S. D. M. 1983, *MNRAS*, 205, 1009
- Netzer, H. & Trakhtenbrot, B. 2007, *ApJ*, 654, 754
- Norberg, P., Baugh, C. M., Gaztañaga, E., & Croton, D. J. 2009, *MNRAS*, 396, 19
- Norberg, P., Baugh, C. M., Hawkins, E., et al. 2001, *MNRAS*, 328, 64
- Omma, H., Binney, J., Bryan, G., & Slyz, A. 2004, *MNRAS*, 348, 1105
- Padmanabhan, N., White, M., Norberg, P., & Porciani, C. 2008, arXiv:0802.2105
- Padmanabhan, N., White, M., Norberg, P., & Porciani, C. 2009, *MNRAS*, 397, 1862
- Peacock, J. A. 1999, *Cosmological Physics* (Cosmological Physics, by John A. Peacock, pp. 704. ISBN 052141072X. Cambridge, UK: Cambridge University Press, January 1999.)
- Peng, C. Y., Impey, C. D., Rix, H., et al. 2006, *ApJ*, 649, 616
- Percival, W. & Miller, L. 1999, *MNRAS*, 309, 823
- Percival, W. J., Scott, D., Peacock, J. A., & Dunlop, J. S. 2003, *MNRAS*, 338, L31
- Perryman, M. A. C., de Boer, K. S., Gilmore, G., et al. 2001, *A&A*, 369, 339
- Peterson, B. M., Ferrarese, L., Gilbert, K. M., et al. 2004, *ApJ*, 613, 682
- Porciani, C., Magliocchetti, M., & Norberg, P. 2004, *MNRAS*, 355, 1010
- Press, W. H. & Schechter, P. 1974, *ApJ*, 187, 425
- Richards, G. T. et al. 2005, *MNRAS*, 360, 839
- Richards, G. T. et al. 2006, *AJ*, 131, 2766
- Ricotti, M., Ostriker, J. P., & Gnedin, N. Y. 2005, *MNRAS*, 357, 207
- Ripamonti, E., Mapelli, M., & Zaroubi, S. 2008, *MNRAS*, 387, 158
- Robertson, B., Hernquist, L., Cox, T. J., et al. 2006, *ApJ*, 641, 90
- Ross, N. P., Shen, Y., Strauss, M., et al. 2008, in *American Institute of Physics Conference Series*, Vol. 1082, *American Institute of Physics Conference Series*, 186–190
- Ross, N. P., Shen, Y., Strauss, M. A., et al. 2009, *ApJ*, 697, 1634
- Salpeter, E. E. 1955, *ApJ*, 121, 161

- Salpeter, E. E. 1964, *ApJ*, 140, 796
- Sánchez, A. G., Baugh, C. M., Percival, W. J., et al. 2006, *MNRAS*, 366, 189
- Sánchez, S. F., Jahnke, K., Wisotzki, L., et al. 2004, *ApJ*, 614, 586
- Sanders, D. B., Soifer, B. T., Elias, J. H., et al. 1988, *ApJ*, 325, 74
- Sazonov, S. Y. & Revnivtsev, M. G. 2004, *A&A*, 423, 469
- Scannapieco, E. & Thacker, R. J. 2003, *ApJL*, 590, L69
- Schmidt, M., Schneider, D. P., & Gunn, J. E. 1995, *AJ*, 110, 68
- Seljak, U. 2002, *MNRAS*, 334, 797
- Serber, W., Bahcall, N., Ménard, B., & Richards, G. 2006, *ApJ*, 643, 68
- Sersic, J. L. 1968, *Atlas de galaxias australes*, ed. Sersic, J. L.
- Sesana, A., Haardt, F., Madau, P., & Volonteri, M. 2005, *ApJ*, 623, 23
- Seyfert, C. K. 1943, *ApJ*, 97, 28
- Shakura, N. I. & Sunyaev, R. A. 1973, *A&A*, 24, 337
- Shankar, F., Bernardi, M., & Haiman, Z. 2009a, *ApJ*, 694, 867
- Shankar, F., Crocce, M., Miralda-Escudé, J., Fosalba, P., & Weinberg, D. H. 2008, *ArXiv:0810.4919*
- Shankar, F., Lapi, A., Salucci, P., De Zotti, G., & Danese, L. 2006, *ApJ*, 643, 14
- Shankar, F. & Mathur, S. 2007, *ApJ*, 660, 1051
- Shankar, F., Salucci, P., Granato, G. L., De Zotti, G., & Danese, L. 2004, *MNRAS*, 354, 1020
- Shankar, F., Weinberg, D. H., & Miralda-Escudé, J. 2009b, *ApJ*, 690, 20
- Shen, Y., Greene, J. E., Strauss, M. A., Richards, G. T., & Schneider, D. P. 2008, *ApJ*, 680, 169
- Shen, Y., Strauss, M. A., Oguri, M., et al. 2007, *AJ*, 133, 2222
- Shen, Y. et al. 2009a, *ArXiv e-prints*
- Shen, Y. et al. 2009b, *ApJ*, 697, 1656
- Sheth, R. K., Mo, H. J., & Tormen, G. 2001, *MNRAS*, 323, 1
- Sheth, R. K. & Tormen, G. 1999, *MNRAS*, 308, 119
- Shinozaki, K., Miyaji, T., Ishisaki, Y., Ueda, Y., & Ogasaka, Y. 2006, *AJ*, 131, 2843
- Siana, B. et al. 2006, preprint, *astro-ph/0604373*
- Sijacki, D. & Springel, V. 2006, *MNRAS*, 366, 397
- Sijacki, D., Springel, V., Di Matteo, T., & Hernquist, L. 2007, *MNRAS*, 380, 877
- Silk, J. & Rees, M. J. 1998, *A&A*, 331, L1

- Silverman, J. D., Mainieri, V., Lehmer, B. D., et al. 2008, *ApJ*, 675, 1025
- Silverman, J. D. et al. 2005a, *ApJ*, 618, 123
- Silverman, J. D. et al. 2005b, *ApJ*, 624, 630
- Small, T. A. & Blandford, R. D. 1992, *MNRAS*, 259, 725
- Soltan, A. 1982, *MNRAS*, 200, 115
- Somerville, R. S. & Primack, J. R. 1999, *MNRAS*, 310, 1087
- Somerville, R. S., Primack, J. R., & Faber, S. M. 2001, *MNRAS*, 320, 504
- Spergel, D. N. et al. 2003, *ApJS*, 148, 175
- Spergel, D. N. et al. 2007, *ApJS*, 170, 377
- Springel, V. 2005, *MNRAS*, 364, 1105
- Springel, V., Di Matteo, T., & Hernquist, L. 2005a, *ApJL*, 620, L79
- Springel, V., Di Matteo, T., & Hernquist, L. 2005b, *MNRAS*, 361, 776
- Springel, V. & Hernquist, L. 2003a, *MNRAS*, 339, 289
- Springel, V. & Hernquist, L. 2003b, *MNRAS*, 339, 312
- Springel, V., White, S. D. M., Tormen, G., & Kauffmann, G. 2001a, *MNRAS*, 328, 726
- Springel, V., Yoshida, N., & White, S. D. M. 2001b, *New Astronomy*, 6, 79
- Springel, V. et al. 2005c, *Nature*, 435, 629
- Steffen, A. T., Barger, A. J., Cowie, L. L., Mushotzky, R. F., & Yang, Y. 2003, *ApJL*, 596, L23
- Strand, N. E., Brunner, R. J., & Myers, A. D. 2008, *ApJ*, 688, 180
- Sutherland, R. S. & Dopita, M. A. 1993, *ApJS*, 88, 253
- Tamura, N., Ohta, K., & Ueda, Y. 2006, *MNRAS*, 365, 134
- Thacker, R. J., Scannapieco, E., & Couchman, H. M. P. 2006, *ApJ*, 653, 86
- Thacker, R. J., Scannapieco, E., Couchman, H. M. P., & Richardson, M. 2009, *ApJ*, 693, 552
- Tremaine, S., Gebhardt, K., Bender, R., et al. 2002, *ApJ*, 574, 740
- Treu, T., Malkan, M. A., & Blandford, R. D. 2004, *ApJL*, 615, L97
- Treu, T., Woo, J., Malkan, M. A., & Blandford, R. D. 2007, *ApJ*, 667, 117
- Tundo, E., Bernardi, M., Hyde, J. B., Sheth, R. K., & Pizzella, A. 2007, *ApJ*, 663, 53
- Ueda, Y., Akiyama, M., Ohta, K., & Miyaji, T. 2003, *ApJ*, 598, 886
- Urry, C. M. & Padovani, P. 1995, *Publ. Astr. Soc. Pac.*, 107, 803
- Vale, A. & Ostriker, J. P. 2004, *MNRAS*, 353, 189

- Vestergaard, M. 2002, *ApJ*, 571, 733
- Viola, M., Monaco, P., Borgani, S., Murante, G., & Tornatore, L. 2007, ArXiv e-prints, 710
- Volonteri, M., Haardt, F., & Madau, P. 2003, *ApJ*, 582, 559
- Volonteri, M., Sikora, M., & Lasota, J.-P. 2007, preprint, astro-ph/0706.3900, 706
- Wang, J., De Lucia, G., Kitzbichler, M. G., & White, S. D. M. 2007, preprint, astro-ph/0706.2551, 706
- Wang, L. & Kauffmann, G. 2008, *MNRAS*, 391, 785
- Wechsler, R. H., Zentner, A. R., Bullock, J. S., Kravtsov, A. V., & Allgood, B. 2006, *ApJ*, 652, 71
- Weinmann, S. M., van den Bosch, F. C., Yang, X., et al. 2006, *MNRAS*, 372, 1161
- Wetzel, A. R., Cohn, J. D., & White, M. 2009, *MNRAS*, 394, 2182
- Wetzel, A. R., Cohn, J. D., White, M., Holz, D. E., & Warren, M. S. 2007, *ApJ*, 656, 139
- White, M., Martini, P., & Cohn, J. D. 2008a, *MNRAS*, 390, 1179
- White, M., Martini, P., & Cohn, J. D. 2008b, *MNRAS*, 390, 1179
- White, S. D. M. & Frenk, C. S. 1991, *ApJ*, 379, 52
- White, S. D. M. & Rees, M. J. 1978, *MNRAS*, 183, 341
- Wolf, C., Wisotzki, L., Borch, A., et al. 2003, *A&A*, 408, 499
- Wyithe, J. S. B. 2006, *MNRAS*, 365, 1082
- Wyithe, J. S. B. & Loeb, A. 2002, *ApJ*, 581, 886
- Wyithe, J. S. B. & Loeb, A. 2003, *ApJ*, 595, 614
- Wyithe, J. S. B. & Loeb, A. 2005, *ApJ*, 634, 910
- Wyithe, J. S. B. & Loeb, A. 2009, *MNRAS*, 395, 1607
- Yang, Y., Mushotzky, R. F., Barger, A. J., & Cowie, L. L. 2006, *ApJ*, 645, 68
- York, D. G., Adelman, J., Anderson, Jr., J. E., et al. 2000, *AJ*, 120, 1579
- Younger, J. D., Fazio, G. G., Wilner, D. J., et al. 2008, *ApJ*, 688, 59
- Yu, Q. & Lu, Y. 2004, *ApJ*, 602, 603
- Yu, Q. & Tremaine, S. 2002, *MNRAS*, 335, 965
- Yu, Q. & Tremaine, S. 2003, *ApJ*, 599, 1129
- Zehavi, I., Zheng, Z., Weinberg, D. H., et al. 2005, *ApJ*, 630, 1
- Zel'Dovich, Y. B. 1964, *Soviet Physics Doklady*, 9, 195